



**NTNU – Trondheim**  
Norwegian University of  
Science and Technology

# Geological and Mineralogical Characterization of the Upper Part of the Gamasfjell Quartzite at the Vaggecearu Mountain

**Jonas Arthur Pevik**

Geology

Submission date: May 2015

Supervisor: Kurt Aasly, IGB

Co-supervisor: Steinar Ellefmo, IGB  
Sean Berger, Elkem Tana

Norwegian University of Science and Technology  
Department of Geology and Mineral Resources Engineering



## Abstract:

In Northern Norway on the Varanger Peninsula, the Gamasfjell quartzite extends as a belt over a large area, from Porsganger in the west to Skallelv in the east. The Gamasfjell Formation is Precambrian in age, and represents an important industrial mineral resource, where the upper part is mined by Elkem Tana for ferrosilicon and silicon, in Autertana, Finnmark. For Elkem Tana, the quality of the quartzite is defined primarily by its chemical purity ( $\text{SiO}_2$  concentration), where  $\text{Al}_2\text{O}_3$ ,  $\text{Fe}_2\text{O}_3$  and  $\text{TiO}_2$  represent the main contaminating oxides.

The upper part of the Gamasfjell Formation on the Vaggecearru Mountain, approximately 2 km NE of the mine, has been mapped and sampled for mineralogical examination. Samples were studied in microscope and analyzed by ICP-EOS, XRD and EMP. The data have been used to produce a 3D model of the deposit.

The upper part of the Gamasfjell formation was divided into three distinct sub units, based on visual appearance. In descending order, these units have been termed Unit A, Unit B and Unit C. Unit A (~38m thick) is light gray, massive and extensively cemented. Unit B (~18m thick) alternates between pink and red and contains more hematite. Unit C alternates between several shades and tints of red, small-scale sedimentary structures are characteristic. Hematite and the phyllosilicates, sericite and pyrophyllite are relatively abundant. Each of the visually defined units could also be recognized chemically. In Unit A there is a minimal amount of contaminating oxides and it therefore represents good quality quartzite, Unit B has a high  $\text{Fe}_2\text{O}_3$  content and represents intermediate quality. Unit C contains high amounts of all three contaminating oxides and represents the footwall of the deposit.

Structurally, the Gamasfjell Formation is folded by a gentle, upright, horizontal fold. Three main joint sets affect the strata, as well as a set of pervasive master joints. Weathering has caused alteration in zones surrounding the joints, particularly in Unit B.

Both the mineralogical and textural maturity of the quartzite decreases with stratigraphic depth. Clay minerals are autogenic in origin, and were likely produced by dissolution, alteration and replacement of detrital feldspar, during diagenesis. The uppermost part of the formation is interpreted to have been reworked or recycled to a larger degree, destroying feldspar before burial. Hematite was probably formed shortly after deposition (apparent by grain coatings) and during burial diagenesis, by the dissolution of iron bearing minerals. Rutile may be both detrital and diagenetic in origin (as the polymorph anatase). A strong correlation between  $\text{TiO}_2$  and  $\text{Al}_2\text{O}_3$  may point towards the latter.

Based on the 3D model, a resource estimation of the SE flank was made, showing promising results, with large amounts of good quality quartzite.

## Sammendrag

På Varangerhalvøya i Nord Norge breier Gamasfjell kvartsitten seg som et belte over et stort område, fra Porsganger i Vest til Skallelv I Øst. Gamasfjell Kvartsitten er av prekambrisk alder. Den representerer en viktig minerals forekomst, hvor Elkem Tana benytter den til utvinning av industrimineralene, ferrosilisium og silisium, Austertana, Finnmark. For Elkem er kvaliteten på kvartsitten bestemt ut i fra hvor ren den er i silisium. Det er hovedsakelig,  $\text{Al}_2\text{O}_3$ ,  $\text{Fe}_2\text{O}_3$  og  $\text{TiO}_2$  som representerer forurensende oksider.

Den øverste delen av Gamasfjellkvartsitten er ved Vaggecearru Fjellet, som ligger omtrent 2km NE for gruva, har blitt kartlagt og prøvetatt for mineralogiske undersøkelser. Prøvene har blitt studert i mikroskop og analysert ved ICP-IO, XRD og EMP. Dataene har blitt brukt til å produsere en 3D modell av forekomsten.

Den øverste delen av Gamasfjellkvartsitten ble delt inn i tre enheter, basert på visuelle karakteristikk. I synkende rekkefølge er disse definert som; Enhet A, enhet B og enhet C. Enhet A (~38m tykk) er lys grå, massive og godt cementert. Enhet B (~18m tykk) veksler mellom rosa og rød, og inneholder mer hematitt. Enhet C, veksler mellom flere variasjoner av rød, småskala sedimentære strukturer er typiske. Hematitt og leiremineralene serisitt og pyrophyllitt opptrer ofte. Disse tre enhetene viser også en gjenkjennbar kjemisk signatur. Enhet A inneholder minimale mengder forurensende oksider og representerer god kvalitet. Enhet B inneholder mer  $\text{Fe}_2\text{O}_3$  og representerer middels kvalitet. Enhet C inneholder forholdsvis mye  $\text{Al}_2\text{O}_3$ ,  $\text{Fe}_2\text{O}_3$  og  $\text{TiO}_2$ , noe som gjør at enhet C representerer avgrensingen til forekomsten.

Strukturelt er Gamasfjell formasjonen foldet av en svak, stående, horisontal fold. Formasjonen har blitt påvirket av tre sprekkesett, i tillegg til ett fjerde sprekkesett som er dypt-penetrerende. Forvitring langs sprekkesettene har forårsaket omvandling i soner rundt sprekkesettene, særlig i enhet B.

Både den mineralogiske og den teksturale modningsgraden til kvartsitten, synker i samsvar med den stratigrafiske dybden. Leiremineralene har en diagenetisk opphav. De ble sannsynligvis dannet fra oppløsning, omvandling og utbytting av feltspat. Den øverste delen av formasjonen er tolket til å ha blitt re-avsatt eller resirkulert i større grad, slik at de fleste feltspatkorn var blitt ødelagt ved siste avsetningen. Hematitt ble sannsynligvis dannet rett etter avsetning (hematitt omrissene originale korn grenser), og under begravelse, ved at jernholdige mineraler gikk i oppløsning. Rutile kan være avsatt, men kan også ha blitt dannet under begravelse, da som et polymorf av rutile (antase). En sterk korelasjon mellom  $\text{Al}_2\text{O}_3$  og  $\text{TiO}_2$  kan peke mot det siste.

Basert på 3D modellen har et ressursestimert av den sørvestlige flanken blitt generert. Den viser lovende resultater, med store mengder god kvalitet.

## Acknowledgements

This master thesis has been carried out at the Department of Geology and Mineral Resources Engineering at the Norwegian University of Science and Technology (NTNU), Trondheim. This thesis is written in collaboration with Elkem AS, who have funded much of the project.

Firstly, I would like to thank my supervisors Kurt Aasly, who suggested this thesis to me, and Steinar Ellefmo, for all their help and encouragement during this project. I would like to show my gratitude to Sean Berger at Elkem, who spent many days out in the field with me, assisting with important observations and helping with the hard work of extracting samples and carrying them back. I would also like to thank Trond Veisal, the exploration manager at Elkem, for sending me articles and sharing his knowledge in the field.

I want to thank the employees at Elkem Tana, for their help with sample perpetrations and their hospitality. Lastly, I want to thank my classmates at NTNU for all the good times!

## Contents

1	Introduction.....	1
1.1	Background of thesis .....	1
1.2	Objectives and scope .....	1
1.3	Outline of thesis.....	3
1.4	Location .....	4
1.5	History and previous work .....	5
2	Background .....	6
2.1	Geological setting .....	6
2.2	Tanafjord-Varangerfjord region .....	7
2.3	The Gamafjell Formation.....	8
2.3.1	Distribution and thickness.....	8
2.3.2	Description .....	8
2.3.3	Stratigraphic relations .....	8
2.4	Local geology .....	9
2.5	Quartzites: Uses and specifications .....	10
2.5.1	Applications .....	10
2.5.2	Assessment criteria for quartzites .....	11
2.5.3	Elkem Tana: Products and classification .....	12
3	Theory .....	15
3.1	Quartz .....	15
3.2	Quartzites and sandstones.....	15
3.2.1	Sandstone classification .....	15
3.2.2	Nomenclature .....	16
3.2.3	Quartz arenites.....	16

3.2.4	Chemical composition sandstones .....	18
3.2.5	Diagenesis .....	19
3.3	Structural geology (folds).....	20
4	Methods and material.....	21
4.1	Fieldwork.....	21
4.2	Equipment.....	22
4.3	Geological Mapping .....	23
4.4	Surface sampling .....	24
4.5	Crushing and milling .....	27
4.6	Microscopy .....	27
4.7	Electron Micro probe (EMP).....	27
4.8	X-Ray Diffraction (XRD).....	28
4.9	Inductively coupled plasma optical emission spectrometry (ICP-OES) .....	28
4.10	Heat Index (HI) and Thermal strength sampling (TSI). .....	28
4.11	DDH positioning and core logging.....	28
4.12	Structural measurements.....	29
4.12.1	Bedding .....	29
4.12.2	Fractures .....	29
4.13	Modeling.....	30
5	Results.....	31
5.1	Map description and lithology .....	31
5.2	Sedimentary structures .....	35
5.3	Microscopy .....	37
5.3.1	Texture: .....	37
5.3.2	Mineralogy .....	37

5.4	Geochemistry .....	44
5.4.1	Bulk geochemical characteristics: .....	44
5.4.2	Chemical relations .....	46
5.5	Color .....	47
5.6	Heat index and thermal strength index: .....	48
5.7	Stratigraphy: .....	49
5.7.1	Lithological logs: .....	49
5.7.2	Geochemical log: .....	50
5.8	Structural Geology .....	53
5.8.1	Fold classification .....	53
5.8.2	Fractures .....	56
5.8.3	Faults .....	58
5.9	Weathering .....	60
5.10	Petrography .....	62
5.10.1	Unit A: Light gray quartzite .....	62
5.10.2	Unit B: Pink and red quartzite .....	65
5.10.3	Unit C: Pink/red/violet quartzite .....	68
5.11	3D model .....	71
5.11.1	Assumptions and constraints .....	71
5.11.2	Presentation of model .....	73
5.11.3	Resource estimation .....	76
6	Discussion .....	77
6.1	Geochemistry and appearance .....	77
6.2	Diagenesis .....	80
6.3	Structural geology: .....	81



6.4	Assumptions, constraints and inaccuracies in model .....	83
6.5	Future drilling campaign suggestion .....	84
7	Conclusion .....	86
8	Futher Work .....	88
9	References:.....	89
Appendix A	Sample Locations .....	91
Appendix B	Material and methods .....	92
Appendix C	Microprobe results.....	96
Appendix D	XRD Results:.....	103
Appendix E	Bulk chemistry of all samples .....	106
Appendix F	Photo of core.....	109
Appendix G	Structural measurements.....	111
Appendix H	Leapfrog data.....	117

Figure 1.1:	Map showing the location of the study area (framed) and location of quarry (circle). lower map scale: 1:71 767.....	4
Figure 2.1:	Stratigraphic coloumb of the Tanafjord-Varangerfjord groups, from Fjellanger (2007). Note that outdated terms are used for age. ....	7
Figure 2.2:	View of the Vaggecearru Mountain and the outcropping formations in the area.....	10
Figure 2.3:	Examples of usages and products that contain ferrosilicon and silicon metal. From (Schei et al., 1997).....	11
Figure 2.4:	Photo taken at the mine site, structurally at the fold hinge. The boundary between light gray and red quartzite is clearly visible. ....	14
Figure 3.1:	Dotts classification of silicate sandstones from (Dott, 1964). ....	15
Figure 3.2:	a) Fold classes based on the relationship between axial surface dip and plunge of hinge line. Based on Fleuty, 1964. From Fossen, 2010. b) Fold classification based on dip isogons. From (Ramsay and Huber, 1987).....	21
Figure 4.1:	Aerial image of the Vaggecearru Mountain with the location of the profiles. ....	25

Figure 4.2: Profile 1 (left) and profile 2 (right). Samples collected at outcrops close to profiles..	26
Figure 5.1: Geological map created in ArcGis, Showing the formations, sub units and boundaries in the study area. Bedding measurements and the axial plane trace is also shown.....	32
Figure 5.2: Cross section of the fold. Extending from Lilleleirpollen (A) to Vaggedalen (B). .....	33
Figure 5.3: Field observation of different sedimentary structures. a) Massive bedding in Unit A. b) Unidirectional crossbedding in Unit C. c) Bimodal crossbedding in Unit C. d) Lense of clay sandwiched between quartzite, in Unit C. e) Small cavities, surrounded b .....	36
Figure 5.4 Quartz grains at varies depths: a) Tripple junctions between grain (Sample. Pr2+13,5 at 16,5m depth). b) Polycrystalline grains (Sample Pr2-15 at 53m depth. c) Layers of medium grained and fine-very fined grained quartz (Sample Pr2-30 at 69,5m depth). d) Bimodal distribution (poorly sorted) of very coarse grains and fine grains, notice also polycrystalline grains (Pr1-45 at 76m depth). (Scale bar: 1 mm).....	38
Figure 5.5: Muscovite inclusion in a quartz grain. (Sample PR1-45) at 76m depth. (scale bar: 1 mm) .....	39
Figure 5.6: a) Angular zircon grain showing high order interference color (Pr2-30, at 69,5m depth). b) Rounded tourmaline grain (Blue)between quartz grains. Note the fracture that follows grain boundaries (Pr2-22, at 61,5m depth). c) Needle shaped rutile inclusion (Prw+13,5, at 16,5 m depth). Scale bar: 1 mm. Note that images are distorted in relation to each other, due to cropping and stretching. ....	40
Figure 5.7: Grain sized/shaped pores filled with sericite. Sample (PR2+13.5) at approximately 16.5m depth. (scale bar: 1 mm).....	41
Figure 5.8: Etched quartz bordering pyrophyllit. Note the dust like rims covering detrital quartz grains. From sample (PR2-25) at 64m depth (scale bar: 1 mm). ....	42
Figure 5.9: Plane light microimage of sample (PR2-30) at approximately 69.5 m depth. Alternating layers of medium and fine-grained quartz, notice how hematite is concentrated in the fine-grained fraction. Scale bar: 1mm. ....	43
Figure 5.10: XRD analysis of sample PR2-30, showing 0.64% hematite. Note that all clay minerals are categorized as muscovite by XRD.....	44
Figure 5.11 Al <sub>2</sub> O <sub>3</sub> distribution withing each sub unit. Sub surface and surface sample are differentiated, as seen, subsurface and surface samples do not differ much in Al <sub>2</sub> O <sub>3</sub> . ....	45

Figure 5.12: Fe <sub>2</sub> O <sub>3</sub> distribution within each sub unit. Sub surface and surface sample are differentiated, as seen, subsurface samples are typically more rich in Fe <sub>2</sub> O <sub>3</sub> .	45
Figure 5.13: Scatter diagrams showing the relation between Al <sub>2</sub> O <sub>3</sub> and other common oxides (TiO <sub>2</sub> , K <sub>2</sub> O, Na <sub>2</sub> O, Fe <sub>2</sub> O <sub>3</sub> ).	46
Figure 5.14: The color of the samples collected within each sub unit.	47
Figure 5.15: Lithological logs of Profile 1, Profile 2 and DDH-VR-14-01. Sedimentary structure observed in outcrop were not observed in the DDH core. Boundaries defined in the field, correspond well with the boundaries in the DDH core.	50
Figure 5.16: Geochemistry of profile 1, profile 2 and DDH-VR-14-01 plotted against depth, showing the same general trend between the geochemistry of the two profiles and the DDH.	51
Figure 5.17: DDH log. The lithological and geochemical logs are combined. The Green and red vertical lines show the boundaries of good and bad quality respectively. The yellow vertical line is based on Elkems quality classification. The horizontal red and violet lines show the chemical boundaries used in the 3D model and resource estimation.	52
Figure 5.18: Sketch of strike lines, from the structural measurements, overlying a simplified geological map. The axial surface trace is drawn in.	54
Figure 5.19: a) Measurements of bedding around the fold, including the Gamafjell Formation, Vagge Formation. and the Hanglecearru Formation. Poles to the bedding plot along a great circle. The pole to this great circle represents the fold axis (trend/plunge). b) 1% area contours of poles.	55
Figure 5.20: a) The main joint sets on the SE fold limb. b) Poles to the joints plot on the average bedding plane, indicating that they are perpendicular to the bedding. c) Shows the area where joints were mapped, master joints are clearly visible as light stripes.	57
Figure 5.21: Color change in proximity of quartz veins, indicating leaching of hematite.	58
Figure 5.22: Location of two sinistral faults. Breccia observed at fault 1.	59
Figure 5.23: a) Weathering along open joint in Unit B, fracture planes have a sugary texture extending outwards. b) Image from the top of the Vaggecearru Mountain, where unconsolidated sand covers the bedrock. c) Closed joints in Unit C.	61
Figure 5.24: A typical sample of Unit A, taken from a depth of approximately 32m below the Vagge Formation (Sample: Pr2+5).	63

Figure 5.25: Typical sample of Unit B, Collected at a depth of approximately 46m below the Vagge Formation (Sample: Pr2-7,5). .....	65
Figure 5.26: Typical sample of Unit B, Collected at a depth of approximately 70m below the Vagge Formation ((Sample: Pr2-30). .....	68
Figure 5.27: Cross section of the fold (053/90). Made by taking a vertical slice through the 3D model in leapfrog. The DDH is included, showing quality. As can be seen, the good quality extends downward into Unit B. ....	72
Figure 5.28: Cross section of the fold (053/90), same as figure 5.25, but Unit A has been made thicker in order to include the good quality in the pink/red quartzite. ....	73
Figure 5.29: Eastern view of the Vaggecearru Mountain. Aerial images are draped over the topography. Master joints are drawn inn, crossing the Mountain. ....	74
Figure 5.30: Same view as above, but with transparent topography. The different formations and units become visible. ....	74
Figure 5.31: Same view as in the figures two above. Here the aerial images are removed, making the formations and units clearly visible. ....	75
Figure 5.32: NE view. Cross section (053/90). The geometry of the fold is revealed. ....	75
Figure 5.33: Boundary of resource estimation, limited by profile 1 and profile 2 and the DDH VR-14-01 .....	76
Table 1.1: Boundary of resource estimation .....	3
Table 2.1: Products and quality after Elkems categorization. ....	12
Table 2.2: Quality classification used in this thesis. ....	13
Table 4.1: Summary of exploration activity. ....	22
Table 4.2: Number of samples analyzed by each method. ....	22
Table 4.3 Collar and Survey of DDH - VR-14-01 .....	29
Table 5.1: Chemical composition (%) of the clay minerals in the Gamafjell Formation, based on microprobe analysis of samples PR1-27,5, PR2+13.5, PR2-22 and PR2-30. ....	43
Table 5.2: Results of TSI test. Six prepared samples, two are duplicates. All samples have a good HI and TSI. ....	48
Table 5.3: Fold classification. ....	56

Table 5.4: Azimuth and dip of main joint sets and strata within the mapped area on SE fold limb .....	56
Table 5.5: Average major element composition of Unit A. ....	64
Table 5.6: Average major element composition of Unit B. ....	67
Table 5.7: Average major element composition of Unit C. ....	70
Table 5.8: Boundary of resource estimation .....	76
Table 5.9: Results of resource estimation (rounded to nearest 100 000) .....	76
Table 6.1: Collar.....	84
Table 6.2: Survey .....	85
Table 7.1: Characteristics of each unit and their associated quality and maturity. ....	86
Table 7.2: Volume and tonnage from resource estimation (rounded to nearest 100 000).....	87

# 1 Introduction

## 1.1 Background of thesis

The Leirpollen quartzite mine in Tana, Finnmark is the largest quartzite mine in Norway and has been in production since 1974. From 1983 until today, Elkem Tana has operated the mine. Elkem Tana is a substantial industrial mineral producer, with a yearly production of 1,2 million tons. Elkem has separated the quartzite into three main products, which are defined by their chemical properties. The products are sold directly with minimal processing.

The deposit mined in Leirpollen is part of a belt that extends over a large part of Finnmark, from Skallelv in the east to Porsanger in the west. The Gamasfjell Formation is approximately 300 m thick, but the bulk of the resource has been confined to the upper 40m of the Formation. The hanging wall of the Gamasfjell Formation/deposit is represented by gray slate of the overlying Vagge Formation. The footwall of the deposit is not well defined, but is apparent by a gradual increase in mainly aluminum.

The quartzite is exposed to the surface, making exploration uncomplicated and allows for low cost open pit mining. The continuity of good quality quartzite is recognized in proximity of the mine, giving an estimated 20-year lifetime. In order to expand the reserves, Elkem Tana has looked for potential future deposits and have identified the Vaggecearru Mountain as a promising target. Mapping the area will form the basis for this thesis.

## 1.2 Objectives and scope

The upper part of the Gamasfjell Formation in the area around the Vaggecearru Mountain will be mapped and sampled in the field. Quality variations based on colour and mineralogy will be described. Observations of lenses of clay and silt will be noted. Fractures will be mapped. Data collected in the field will be used to create a 3D model of the resource. Based on this model, a resource estimate for the different qualities (low iron, standard) will be made, including a proposal for a future drilling campaign.

**Goals:**

- Assess the contact between the Gamasfjell Formation and the above lying Vagge Formation.
- Define the boundary between the economic and uneconomic part of the quartzite.
- Define the boundary between low iron (grey) and standard quartzite (red).
- Perform structural measurements of the main strata faults and fractures.
- Create a 3D model of the resource, which includes the main faults and weakness zones. Construct maps and profiles including a proposal for future drill-hole positions.

The main goal of this work is to make a preliminary evaluation of the quality and quantity of the quartzite in the target area for use as ferrosilicon and silicon. Much of the literature on the economic potential of sandstones is focused towards the petroleum industry. For this thesis, the focus will be on the properties that are important in respect to the potential the sandstone has as an industrial mineral for silicon and ferrosilicon use. Features such as sedimentary structures, diagenic alterations etc. will be described when observed and evaluated for the eventual influence they may have on the quality of the resource. Interpretation of the depositional environment, source area, diagenic history etc. will however be limited.

Mineralogical descriptions will focus on the appearance of contaminating minerals (minerals other than quartz). Contaminations within the quartz crystal such as lattice bound trace elements or fluid inclusions will not be considered, as the quality is not effected (for ferrosilicon use). All sample descriptions will be qualitative.

The structural investigation will include measurements of the orientation of the local strata, faults and fractures within a predetermined area. The strata orientation data will be used to generate the framework for the 3D model. How the faults and fractures may influence the quality of the deposit will also be considered, but the impact they may have on mining operations, et. engineering problems is beyond the scope. The structural history is also beyond the scope of this thesis. Diamond drill hole (DDH) data will be used to complement the surface data. The core log will present visual observations together with details of the chemical analysis of the samples. Again, no consideration surrounding engineering problems will be made. Simple statistical

methods will be used to evaluate and present data, more advanced geostatistics will not be required. The targeted deposit lays on the NE limb of an anticlinal fold, the investigation will therefore be focused on this area. However, in order to get a better understanding of the geology and the main structures, measurements and sample collection will also partly be performed on the fold hinge and at the SW limb. A 3D model of the fold will be generated and the volume and tonnage of the resource will be estimated for the target area, within the boundary presented in Table 1.1. The model will be exported in a format that can be used for more specific calculations.

*Table 1.1: Boundary of resource estimation*

X (East):	Min: 560407.87	Max: 561334.66
Y (North):	Min: 7821985.52	Max: 7823099.74
Z (Elev):	Min: 275.0	Max: 600.0

### 1.3 Outline of thesis

Chapter 1: Outlines the background, objectives and limitations of the thesis. Also includes the geographic location previous work and history.

Chapter 2: Gives the necessary background knowledge required in order to get familiar with the geology and quartzite as an industrial mineral.

Chapter 3: Presents theory on the formation of quartzites, the chemical composition of sandstones and a brief description of diagenesis and folding.

Chapter 4: Presents the material and methods used in this thesis.

Chapter 5: This chapter presents all the results of the field work. It is structured to first present a general description of the geology, including a detailed description of the mineralogy. The characteristics of the visually defined units are presented in more detail afterwards, but mineral descriptions will be brief to avoid repetition. Finally, a 3D model and resource estimation is presented, with boundaries defined chemically.

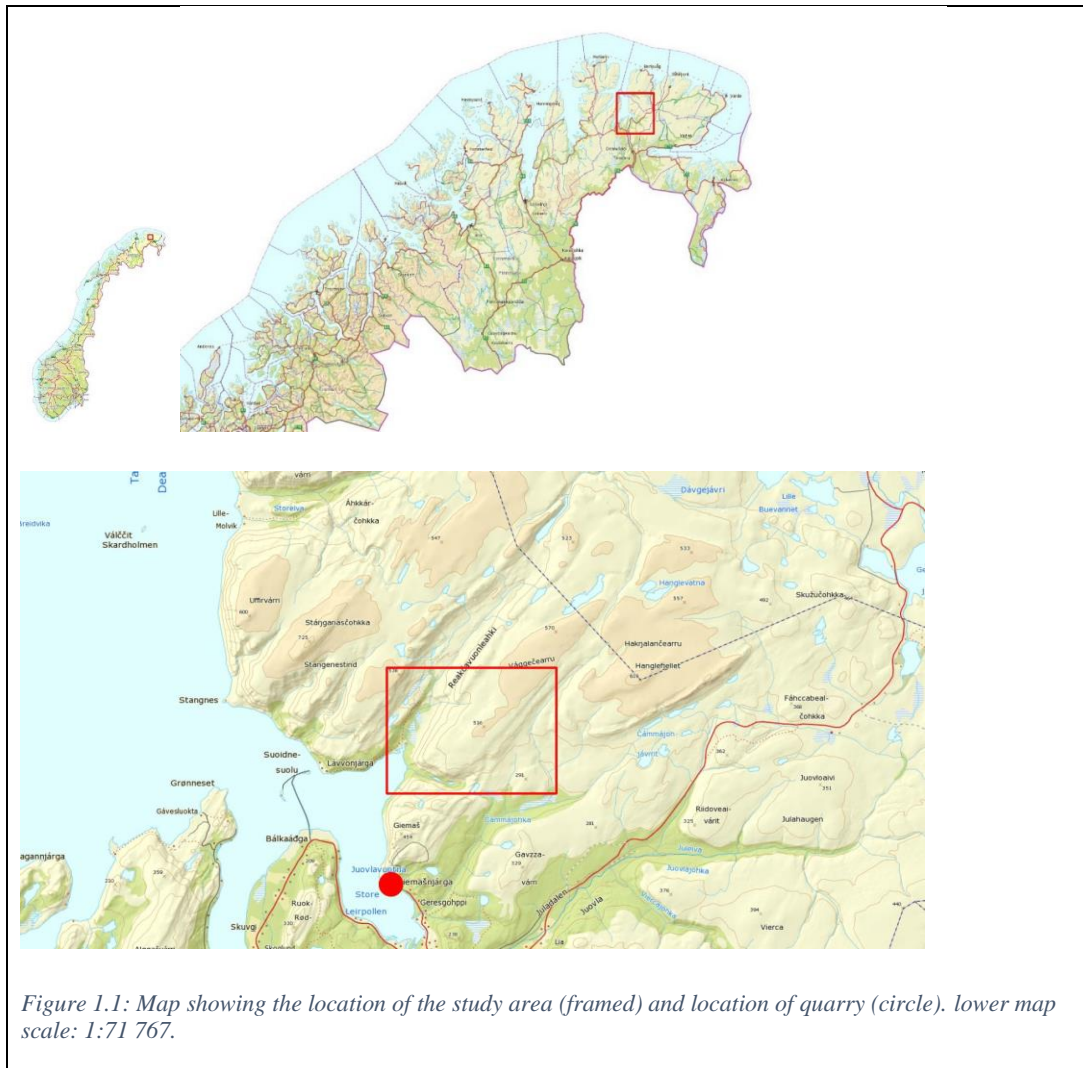
Chapter 6: Discussion of the results, additionally a proposal for a future drilling campaign is made.

Chapter 7: Presents the conclusion of this study.



## 1.4 Location

The Leirpollen quartzite quarry (55 59 20, 7819031 N35) is located in Tana County, Finnmark. It lies in the inner parts of the Tanafjord, on the western part of the Varanger Peninsula. Field work was conducted approximately 2 km to the northeast of the quarry, at the Vaggeciarru Mountain (Figure 1.1) The deposit is exposed to the surface on the SE limb of an anticlinal fold at an altitude of 275m above sea level. Field work was conducted over a broader area, examining both limbs of the local fold. The nearest road and port is located at the mine site. A small body of water is located directly below the deposit and second larger lake (Melkevannet) is located approximately 1 km to the SW. The quartzite is bare for vegetation, except for lichen and moss.



## 1.5 History and previous work

A/S Sydvaranger was the first company to take interest in the quartzites in Finnmark, and in 1956 J.H.W Bugge was the first to explore the quartzite in Austertana for the purpose of industrial minerals. The first sampling was performed in 1963. Extensive work performed in 1971 by Siedlecka and Siedlecki gave detailed knowledge of the quartzites in east Finnmark. The stratigraphic division and terminology used today is attributed to them. A/S Sydvaranger started detailed exploration of specific quartzite deposits in 1971. From 1971-1973, sampling, description and evaluation of the four localities was performed. These were Smafjorden, Tananes, Vaggedalen and Leirpollen (Gamasneset). The conclusion was that good quality quartzite could be found at several localities, and Gamasneset was seen as most promising. Sydvaranger started mining the upper part of the Gamasfjell Formation at Gamasneset in 1973. They found out that the good quality was constrained to the white and upper red quartzite of the Gamasfjell Formation.

In 1975 NGU initiated the North Norway project, with the goal of examining the quartzites of Finnmark and Northern Troms. As a part of this project, Ryghaug and Barjey did extensive field work and sampling at several localities in the summer of 1976 and 1977. They visited sites spanning from Skalelv in the east to Burfjord (Troms) in the west. Analysis, maps and notes from their work is presented in a report on industrial minerals that was published by Wanvik in 1985.

In 1983 Elkem ASA took over the mining and are today the present operator.

In 1990 NGU started a second large mapping project of the quartz resources of Finnmark, where the Gamasfjell Formation was the main focus. The project was named “Finnmarksprogrammet”. In the summer months of 1990 and 1991 extensive fieldwork and sampling was conducted to compliment the work done in the 70s (Størseth and Wanvik, 1992).

In 1996 and 1998, Elkem became interested in exposers at Tananeset. Detailed mapping, sampling and drilling was performed at Tananeset.

In the summer months of 2013 and 2014, drilling was performed to evaluate the continuity of the deposit along strike. DDH logging was performed by the student as part of a summer job.

## 2 Background

### 2.1 Geological setting

The Varanger Peninsula is located at 28 – 31° E and 70-71° N. It is enclosed by the Barents Sea to the north, Varangerfjorden to the south and Tanafjorden to the west. The bedrock is made up of sedimentary strata from the late Precambrian to earliest Cambrian (Siedlecka, 1975).

The Peninsula consists of two geological regions, separated by the NW- SE trending Trollfjord – Komagelv fault zone (TKFZ). Northeast of the fault zone, lies the Barents Sea region, while the Tanafjord – Varangerfjord Region is located southeast of the fault (Siedlecka, 1990). These two regions consist of sedimentary successions that are approximately the same age, but formed under different tectonic conditions at separate locations. It was only after the complete sedimentation of both basins, that dextral slip along the TKFS brought them together (Siedlecka, 1990)

The Tanafjorden – Varangerfjorden sequence accumulated in an autochthonous basin on the northern margin of the Fennoscandian shield and rests upon the metamorphic Karelin substratum. It is approximately 3800 m thick and consists of fluvial, coastal, and shallow marine sediments (Siedlecka, 1990)

The Barents Sea succession consists of about 9 km of deep water, deltaic and shallow marine sediments (Roberts and Siedlecka, 2012). The sediments accumulated in an allochthonous basin, located at an unknown location. It has been suggested, based on paleomagnetic data, that at least 200 km of dextral slip translation along the TKFZ moved the basin to its present location (Roberts and Siedlecka, 2012).

The northwesterly part of the peninsula (below the TKFZ) is part of the Caledonian Nappe complex. Here we find the Tanafjorden group in the Gaisse nappe, a lower allochthon belonging to the Caledonian tectonostratigraphy (Roberts and Siedlecka, 2012).

The strata of the Varanger peninsula has been affected by two main deformation events, where Late Vendian to Early Cambrian Baikalian deformation has led to mainly NW-SE trending folds, found in the eastern parts of Varanger. Late Silurian to Early Devonian Scandian deformation and metamorphism caused folds and thrusts with a NE-SW trend in the western parts of the peninsula, in the Caledonian parautochthon and allochthon (Roberts, 1996).

## 2.2 Tanafjord-Varangerfjord region

The sedimentary sequence extends over the southwestern part of the Varanger peninsula. The entire sequence is almost 4000 meters thick and is subdivided into three groups (Ramberg et al.,

Age	Lithostratigraphic units	
CAMBRIAN-ORDOV.	DIGERMULEN GR. 1510-1550 m	Formation
		Other formations
VENDIAN	VESTERTANA GR. 1300-1650 m	Breivika 600 m
		Stappogiedde 500-550 m
		Mortensnes 10-60 m
		Nyborg 200-400 m
		Smalfjord 2-50 m
TERMINAL RIPHEAN	TANAFJORDEN GR. 1450-1660 m	Grasdalen 280 m
		Hanglecearru 200 m
		Vagge 80 m
		Gamasfjell 300 m
		Dakkovarre 270-350 m
		Stangnes
		Grønnes
		Ekkerøya
		Other formations
RIPHEAN	VADSØ GR. 590-960 m	Other formations
Older Precambrian rocks		

Figure 2.1: Stratigraphic coloumb of the Tanafjord-Varangerfjord groups, from Fjellanger (2007). Note that outdated terms are used for age.

2006). From bottom to top these are the Vadsø group, the Tanafjord group, and the Vestertana group. Each group consists of several Formations. Veidnesbotn is the lowermost Formation of the Vadsø group. It is a sandstone that was deposited as beach sediments on the metamorphic bedrock of the continent Baltika, approximately 800 million years ago (Ramberg et al., 2006). The rest of the Vadsø group consists mostly of fluvial deposits (Siedlecka, 1990). The Tanafjorden and the above lying Vestertana group are mostly shallow marine to marine. Two tillite horizons formed during the Varanger ice age are also present in the Vestertana group (Ramberg et al., 2006). Several erosional surfaces are present in the sequence. The most significant erosional surface is found at the base of the Vestertana group, created by a northward tilting of the layers of the Vadsø and Tanafjorden groups combined with transgression and southward erosion of the sedimentary layers (Siedlecka, 1990). This resulted in the removal of both groups.

Grasdalen, the uppermost Formation of the Tanafjord group is preserved to the northwest close to the TKFZ, all

Formations of both groups have been removed on the

southern parts of the peninsula, where the lowest Formation of the Vestertana group rests directly on top of Veidnesbotn and the basement near Varangerfjorden (Siedlecka, 1990).

## 2.3 The Gamasfjell Formation

### 2.3.1 *Distribution and thickness*

The Gamasfjell Formation extends over a large area of Finnmark, from Skallelv in the east to Porsanger in the west. The Formation is on average about 280-300 m thick (Størseth and Wanwik, 1992), and is identified as a shallow marine sheet complex formed in shallow water, sub tidal and tidal current dominated environments (Johnson, 1978).

### 2.3.2 *Description*

The Gamasfjell is an orthoquartzitic sandbody of Precambrian age. It is thick-benched, homogeneous and varies in color with depth. The upper 10s of meters are white to gray in color, below the color ranges from pink to increasingly red and violet. Crossbedding is characteristic (Johnson, 1978). The color variations are a result hematite flakes, which often are concentrated in bands (Størseth and Wanwik, 1992). Cementation is normally extensive, with pores filled with secondary quartz cement, but in some cases, patches of sericite occur locally (Størseth and Wanwik, 1992). In outcrop, the quartzites are characterized by a weathering surface that is somewhat lighter and more rusty than underlying layers (Størseth and Wanwik, 1992). Lenses of shale and silt are sparse and occur randomly throughout the Formation, a single uniform silty layer is found at about 75m depth below the Vagge Formation (Størseth and Wanwik, 1992).

### 2.3.3 *Stratigraphic relations*

The Gamasfjell rests approximately in the middle of the Tanafjord subgroup, situated between the Vagge Formation and the Dakkovare Formation. In Figure 2.1, the stratigraphic position of the Formation is shown. The underlying Dakkovare Formation is approximately 350m thick and consists of heterogeneous sandstones and shales (Størseth and Wanwik, 1992). At the top of the Gamasfjell Formation, one finds interbeds of arenaceous grey shale which grades into the Vagge shale Formation (Siedlecka, 1990). The Vagge Formation is about 80 m thick and consists of interbeds of arenaceous grey shale and thin beds of grey sandstone (Siedlecka, 1990). A well defined boundary separates the Vagge Formation with the above lying Hanglecærro Formation (Siedlecka, 1990). This Formation consists of medium to thick bedded quartzitic sandstone, the color varies from blue-grey in the lower part to white further up (Siedlecka, 1990).

## 2.4 Local geology

The geology of Eastern Tanafjord is dominated by quartzite and sandstone units that belong to the Tanafjord group. These Formations are very resistant to weathering, and often form insielbergs rising several hundred meters above sea level (Fjellanger et al., 2006).

The Vaggecearru Mountain is part of large undulating plateau that stretches over an area between Trollfjorden, Leirpollen and Geatnjajávri (Fjellanger et al., 2006).

In the study area, one finds outcrops of the Gamasfjell- and Hanglecearru quartzite and the Vagge shale. Figure 2.2, shows the three Formations and the Vaggecearru Mountain in the background. From a structural viewpoint, the Gamasfjell Formation has been folded into a gentle anticline oriented SW-NE. The summit area consists of the Gamasfjell Formation, with fold limbs dipping NW and SE. The present surface cuts the fold, leaving deeper stratigraphy of the Gamasfjell Formation exposed in the summit area. On both the southeastern and northwestern flanks, the upper part of the Gamasfjell Formation is exposed. The Vagge and Hanglecearru Formations also outcrop at the flanks. The limbs of the fold are typically continuous and well exposed.

Autoctonous block fields cover the summit of the mountain as well as large areas of the Varanger peninsula and are generally constrained to quartzite and quartzitic sandstones (Fjellanger et al., 2006). As a result of weathering, sand often covers the spaces between boulders (Fjellanger, 2007).

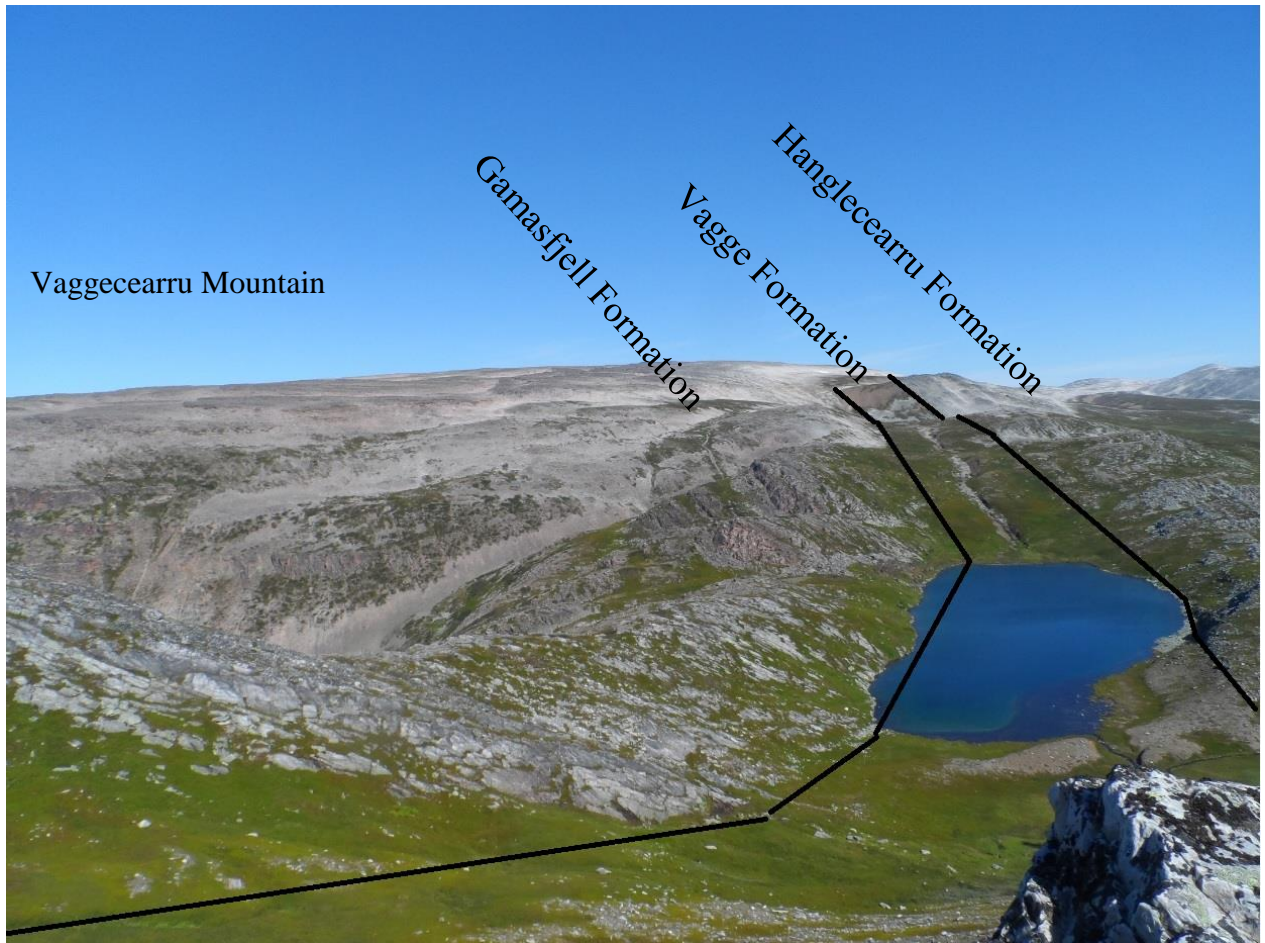


*Figure 2.2: View of the Vaggecearru Mountain and the outcropping formations in the area.*

## 2.5 Quartzites: Uses and specifications

### 2.5.1 Applications

Quartzite is the most common raw material used in the production of ferrosilicon (Tangstad, 2013). The main consumer of ferrosilicon is the steel and cast iron industry (Figure 2.3). In steelmaking it is used for deoxidation (e.g in the production of stainless steel) and alloying where it increases properties such as elasticity, tensile yield and annealing resistance (Schei et al., 1997). In cast iron, ferrosilicon and other elements are used as an inoculant to induce graphite nucleation (Schei et al., 1997). If a quartzite is particularly pure, it can be used to process silicon, but this may require mixing with other quartzites (Aasly, 2008). Silicon metal is used e.g. in the chemical industry, semiconductor industry and for alloying (Aasly, 2008).

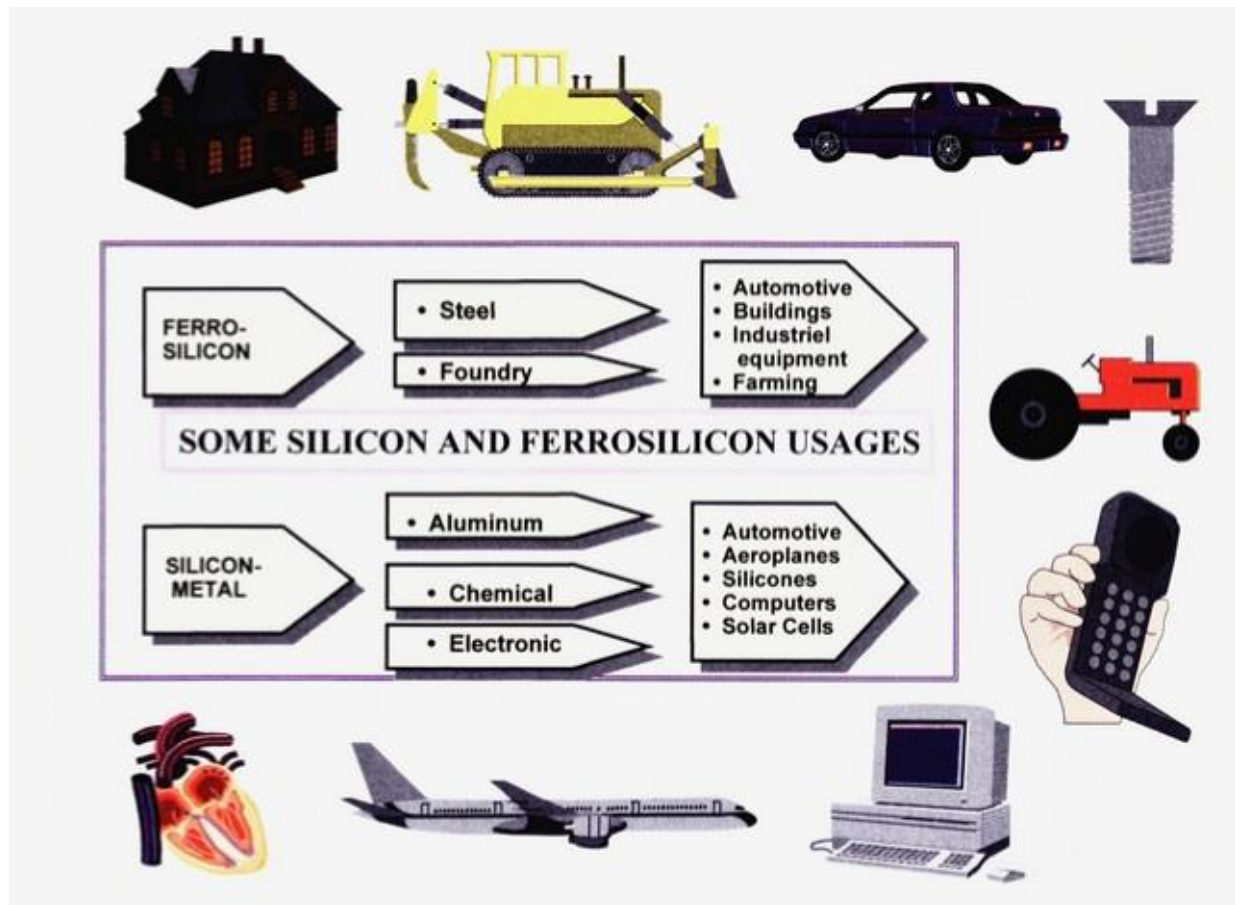


Figure 2.3: Examples of usages and products that contain ferrosilicon and silicon metal. From (Schei et al., 1997)

### 2.5.2 Assessment criteria for quartzites

For ferrosilicon and silicon production, the principal criteria used to assess the quality of a quartzite, is its chemical composition (Al, Fe, Ti, Ca, P and B), lump size, mechanical/thermal strength and softening (Schei et al., 1997). The exact specifications varies for different customers. Generally, chemical composition is considered the most important factor, and a low aluminum content is especially critical (Størseth and Wanwik, 1992). Other contaminating elements include titanium, boron and phosphorous. These elements are often contained in oxides, which due to their refractory nature may not fully melt in the furnace (Kogel et al., 2006)

Besides chemical composition, customers also have criteria for lump size and thermal strength. These properties influence the smelting process in the furnace. It is important that the smelting process is continuous. Too small of a lump size or insufficient thermal strength may lead to



disintegration before smelting (Schei et al., 1997). Generally, lump sizes ranging from 10-150 mm is usual (Schei et al., 1997). Heat treatment and centrifugation followed by sieving is done in order to evaluate the thermal quality. The result is considered good if less than 30% of the material, after heat treatment and centrifugation, passes through a 5mm sieve (Størseth and Wanwik, 1992).

The softening properties is yet another factor that effects processing. A too high softening interval (e.t. the period between quartz starts to melt, up until the melting temperature is met at 1723 °C), may cause the quartzite to soften or melt before it reaches the bottom of the furnace (e.g. Aasly, 2008).

For quartzites used as raw materials in the production of ferrosilicon, color is usually not significant for the quality (Størseth and Wanwik, 1992). This is because the coloring is caused by trace amounts of iron, which is generally not a concern for FeSi – production (Størseth and Wanwik, 1992). In Tana, the color of the quartzite is helpful in determining the approximate stratigraphic depth when mapping.

### 2.5.3 *Elkem Tana: Products and classification*

Elkem Tana delivers four quartzite products, which are categorized on the background of their chemical properties and sizing. The products are listed in Table 2.1. The different qualities are named after their iron- and/or aluminum oxide content. FeSi is short for ferrosilicon and is followed by four numbers. The first 2 numbers specify the amount of aluminum oxide (60 is read as 0,6%), the second two numbers give the amount of iron oxide (45 is read as 0,45%).

Table 2.1: Products and quality after Elkems categorization. .

Quality/oxides		Standard FeSi6045	Low iron FeSi6010	Low iron Si5005	Singel FeSi7045
Fe <sub>2</sub> O <sub>3</sub>	Below	0,45	0,1	0,05	0,45
Al <sub>2</sub> O <sub>3</sub>	Below	0,6	0,6	0,5	0,7
TiO <sub>2</sub>	Below	0,4	0,4	0,4	0,4

A low  $\text{Al}_2\text{O}_3$  content is the most important criteria for ferrosilicon. Elkem operates with a cut-off at 0,60%  $\text{Al}_2\text{O}_3$ . If the percentage is above 0,60 it is considered impure and is not of commercial interest. Values lying between 0,50% and 0,60% are satisfactory and values below 0,50% are considered good quality. Iron oxide may range from 0,05 to 0,45%. The iron oxide content can to a larger degree than aluminum be controlled by mixing different qualities to achieve the desired percentage. There is also a requirements for titanium. If the titanium content exceeds 0,4% it is problematic. Other elements have not been a problem in Tana. In this thesis the qualities are simplified. Table 2.2 presents the qualities used when modeling.

Table 2.2: Quality classification used in this thesis.

Quality/oxides	Good	Intermediate	Bad/Footwall
$\text{Fe}_2\text{O}_3$	<0,05	0,1-0,45	>0,45
$\text{Al}_2\text{O}_3$	<0,5	0,5-0.6	>0,6
$\text{TiO}_2$	<0,4	<0,4	<0,4

The chemical composition is to some degree revealed by the color of the quartzite. The cleanest and best quality is usually confined to light gray quartzite. However, both Standard FeSi6045 and FeSi6010 are usually red and not very easy to distinguish from each other or from the footwall. In some cases the footwall may be noticeable by a larger variation in color and a higher frequency of lenses of clay/silt, but normally it is undistinguishable from the red quartzite above. This is a bit problematic when drilling as there is usually little to no visual indication of when the footwall is passed.

The color differences are best seen in the rock wall of the mine. Figure 2.4, shows a photograph taken at the NE pit (Sommerbruddet). The sharp boundary between gray and red quartzite is clearly seen. The footwall lies at the bottom of the pit.



*Figure 2.4: Photo taken at the mine site, structurally at the fold hinge. The boundary between light gray and red quartzite is clearly visible.*

## 3 Theory

### 3.1 Quartz

Quartz ( $\text{SiO}_2$ ) is the most common and stable mineral of the Earth's crust, making up 12%. (Dyar et al., 2008). It is composed of  $\text{SiO}_4$  tetrahedra in which all four corners are shared with other tetrahedra. There are at least five other main silica polymorphs found in nature, the various silica polymorphs were first described by Fenner (1913) and include cristobalite, tridymite, coesite, stishovite, and moganite (metastable). Fenner (1913) demonstrated with diagrams, that these polymorphs form under different pressure and temperature conditions. The different silica polymorphs have the same chemistry, but the crystal structures are different. (Dyar et al., 2008). Aside from stishovite, each of the polymorphs have completely linked  $\text{SiO}_4$  tetrahedra, though the arrangements vary (Dyar et al., 2008).

### 3.2 Quartzites and sandstones

#### 3.2.1 Sandstone classification

Several different methods have been developed for sandstone classification. The most common classification scheme used for the subdivision of terrigenous sandstones, is that which was developed by Dott (1964). The scheme compares the amount of framework grains to the amount of matrix, and the amount of detrital quartz to feldspar and rock fragments (Figure 3.1). In this way, it considers both mineralogy and texture. For a more detailed description one may also add grain size, sorting, cementation, porosity and color (Pettijohn et al., 1987)

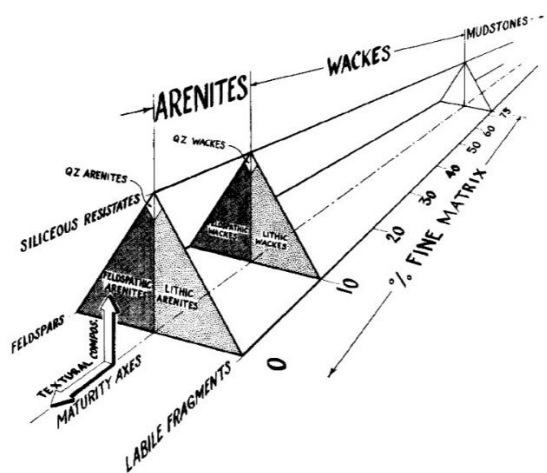


Figure 3.1: Dott's classification of silicate sandstones from (Dott, 1964).

### 3.2.2 *Nomenclature*

A quartzite is considered to be a rock that is so extensively cemented that it breaks across grain boundaries instead of around them (*Pettijohn et al., 1987*). The term orthoquartzite is often used for quartzites with a sedimentary origin, differentiating them from those of metamorphic origin, which are termed metaquartzites. The term quartz arenite has replaced the term orthoquartzite in recent years, but often these two terms are used interchangeably (*Pettijohn et al., 1987*). The Gamasfjell Formation has been described as a quartzitic sandstone (*Siedlecka, 1990*), and quartzite (*Størseth and Wanwik, 1992*). In this report, the term quartzite is used, although it would be more correct to call it a quartzitic sandstone or orthoquartzite. The protolith to the Gamasfjell Formation is sedimentary in origin, a quartz arenite.

### 3.2.3 *Quartz arenites*

#### *Characteristics*

Quartz Arenites are generally defined as sands containing >90 -95% siliceous grains (*Boggs, 2009*). This is the highest compositional maturity of any sand, commonly resulting in a bulk chemistry of over 99% silica. Such a high silica content can make them commercially interesting. Extreme textural maturity is also characteristic of many quartz arenites, but not all. A texturally mature quartz arenite is well sorted and consists of very rounded unstrained monocrystalline quartz. Due to burial diagenesis, grains may appear angular because of cement overgrowth (*Pettijohn et al., 1987*). Textural inversion is observed in some quartz arenites. Some for example contain highly rounded but poorly sorted grains.

Mineral constituents other than quartz may be present in small or trace amounts. Lithic fragments are rare and accessory minerals extremely rare. Durable chert and other detrital fragments are sometimes present (*Pettijohn et al., 1987*). Heavy minerals are usually present, but only in trace amounts, the most common being well-rounded tourmaline, zircon and rutile. Less common heavy minerals are hornblende, sphene, monazite, magnetite, epidote, apatite, leucoxene, hypersthene and magnetite. Most quartz arenites contain little to no matrix. When present it is usually thought to be diagenetic in origin and consists of fine grained quartz, micas, feldspar and clay minerals (*Boggs, 2009*). Overgrowths are common, as well as pressure solution at grain to grain contacts. The cement is usually quartz, but some are also cemented by carbonates or hematite. Characteristic structures are crossbedding and/or ripple marks (*Pettijohn, 1987*). Most quartz arenites are white in color, some are also pink or red due to hematite coatings on grains

(Pettijohn, 1987). The color of sedimentary rocks can be of secondary or primary origins. In most cases, the colors are primary and are a function of the depositional environment. Processes that may influence the color are redox conditions and rate of deposition of organic matter (Paul Myrow, 2003).

### *Origin of quartz arenites*

Generally, stable cratons of low relief in tropical climates produce super mature sands. The source may be a granite or gneiss basement, but recycling is considered as the main source (Pettijohn, Potter, Siever, 1987). Intense tropical weathering and strong abrasive forces working over long amounts of time may however produce first cycle quartz arenites (Soegaard and Eriksson, 1989) On a stable craton, two depositional environments are believed to be capable of reworking material to such a degree as to produce quartz arenites. These are shallow marine environments at passive margins, where deposited immature sand is “cleaned” and rounded by the back and forth moving tides, and eolian environments where wind is the abrasive/sorting agent (Chandler, 1988)

Early studies attributed a dominant role to wind, but later work has shown that many quartz arenites had a history of both wind and tidal weathering (Dott Jr, 2003). Diagenetically formed quartz arenites are also possible (Chandler, 1988). Diagenetic processes may occur both at the surface (eogenesis) by chemical purification of stored sands, and after burial where labile grains may be removed chemically at a large scale (Dott Jr, 2003).

A marine origin is often evident by associated marine shales and marine biota, low relief erosion, extensive crossbedding as well as accessory glauconite and phosphates (Chandler, 1988).

Evidence of eolian weathering comes from the frosting or micro-roughens of sand grains and bimodal distribution in grain size (Chandler, 1988). It is also believed that extreme roundness of coarse quartz grains, only can be achieved by wind abrasion. Diagenesis is recognised by oversized pores, etched skeletal grains and clay and other postdepositional replacement of grains (Dott Jr, 2003). There are several ways to recognize recycling. For instance, overgrowths are post depositional features, abraided overgrowths which are typical in quartz arenites, imply that the grains must have had a sedimentary past (Pettijohn, Potter, Siever, 1987). Multicycling is also evident in many quartz arenites that contain a mixture of accessory minerals from different sources, with no contribution from the underlying basement (Dott Jr, 2003).

Most quartz arenites are polycyclic, with both eolian and tidal features, the final deposition is

however argued to have been in shallow marine environments (Pettijohn, Potter, Siever, 1987). There are few modern sands displaying a high amount of textural maturity (Chandler, 1988). Some modern beaches are of quartz arenitic composition, but lack the rounding of ancient examples and are much less extensive (Dott Jr, 2003). The most extensive quartz arenitic sandstones are dated as late-Precambrian to early Paleozoic (Such as the Gamafjell Formation). (Chandler, 1988).

### 3.2.4 Chemical composition sandstones

The bulk chemical composition of sandstones is useful as a compliment to the mineralogical-textural composition, and is often used in the study of metamorphic varieties of sandstones (Pettijohn et al., 1987). It shows some of the relationships between elemental composition, mineralogy, and rock type (Pettijohn, Potter and Siever, 1987). Below is a presentation of the elements that make up the main minerals and some of the trace minerals found in sandstones.

#### *Sodium and potassium:*

Sodium and potassium usually only represent a few percent of the bulk composition of sandstones. In sandstones that contain little clay, most of the potassium and sodium are bound to muscovite and alkali feldspar. In more clay rich sandstones, sodium and potassium are contained in illite and smectite. For both clay rich and clay poor sandstones, potassium is usually more abundant than sodium, because the mica and illite content is normally higher than the feldspar and smectite content (Pettijohn, Potter and Siever, 1987).

#### *Calcium and magnesium:*

Calcium and Magnesium are bound to carbonates and clays. The most important mineral containing calcium is Ca-plagioclase, calcite cements and to some degree smectite clay. Magnesium is present in dolomite cement and the clay minerals smectite and chlorite. In most sandstones, calcium is more abundant than magnesium as calcite cement is more usual than dolomite cement (S. Boggs Jr., 2009). Minerals containing these two elements are primarily a result of chemical precipitation (Pettijohn, Potter and Siever, 1987).

#### *Aluminum:*

Aluminum is included in feldspars, micas and clay minerals. Sandstones with high amounts matrix therefore contain more Al than mature sandstones (S. Boggs Jr., 2009). On the other hand, more mature sandstones usually have more aluminous clays (Pettijohn, Potter and Siever, 1987).

### *Iron:*

Both ferrous ( $\text{Fe}_{2+}$ ) and ferric iron ( $\text{Fe}_{3+}$ ) is common in many minerals. The most important minerals containing ferrous iron are clay minerals (chlorite), carbonates (siderite, ankerite) and sulfides (pyrite, marcasite). Ferric iron is concentrated in iron oxides, such as hematite and goethite. Heavy minerals such as magnetite also contain ferric iron, but the content of magnetite is usually so low that it does not affect the bulk chemical composition of sandstones (*S. Boggs Jr., 2009*). Iron oxides are the reason for the red color of many types of sandstone, but do not contribute much to the total amount of iron as they are usually dispersed as fine grains (*Pettijohn, Potter and Siever, 1987*).

### *Manganese:*

Usually makes up less than 1%. Mainly substitutes for iron in iron oxides. Minor amounts of manganese oxides may sometimes also be present (*S. Boggs Jr., 2009*).

### *Titanium, Sulfur and Phosphorus:*

Most sandstones contain only small amounts of titanium (<1%) (*S. Boggs Jr., 2009*). Titanium is mostly found in clays and in heavy minerals such as rutile and ilmenite (*Pettijohn, Potter and Siever, 1987*). Sulfur is normally present in chemical precipitates of diagenetic origin. Minerals containing sulfur are gypsum, anhydrite, pyrite and marcasite. Phosphorus is contained mainly in apatite, but it is also often present in trace amounts in other minerals (*Pettijohn, Potter and Siever, 1987*). Most sandstones contain less than 100 ppm phosphorus (*S. Boggs Jr., 2009*).

## **3.2.5 Diagenesis**

The mineralogical maturity of quartzites and quartz arenites, is linked to the amount of matrix they contain. The main contaminating minerals for Elkem, are aluminum bearing clays. Clays in quartz arenites are mostly authigenic (Boggs, 2009). Therefore, diagenesis is presented briefly below, with a focus on mesodiagenesis.

Diagenesis involves all processes that modify sediments after deposition. Diagenesis eventually grades into low level metamorphism at a temperature around 300 degrees and pressures between 1-2 kb (Boggs, 1992). Three diagenetic regimes are recognized, eogenesis (early diagenesis in depositional environment), mesogenesis (burial diagenesis) and teleogenesis (uplift related diagenesis) (R.H. Wordan and S.D. Burley, 2003). After burial processes that create extensive



modifications to the rock and leads to observable chemical and textural changes are compaction, dissolution, cementation, authigenesis, and replacement (Milliken, 2003).

Mesodiagenesis takes place in the subsurface at temperatures between 50 and 300 degrees (Milliken, 2003). Physical, chemical and mineralogical changes occur in the mesogenetic regime, but are not as severe as those that take place during metamorphism (Boggs, 2009). Physical processes include compaction and loss of pore space, chemical and mineralogical changes occur in the presence of fluids that interact with minerals toward equilibrium (Wordan and Burley, 2003).

For quartz arenites physical compaction is typically more dominant at greater depths compared to more immature sandstones. Compaction leads to a reduction of porosity to about 26 % due to grain rearrangement and repacking (Wordan and Burley, 2003). Cementation takes place at temperatures above 50 °C, typically at 1-2km depth and is considered an early diagenetic event (Mcbride, 1989).

### 3.3 Structural geology (folds)

Geometric analysis of folds is important in order to understand how folds form. It is also important for the petroleum and mining industry when studying petroleum traps and folded ores in the subsurface (Fossen, 2010). There are many expressions one can use to describe a fold (Fossen, 2010). The orientation of a fold can be described using Fleuty (1964), classification scheme, which is based on the orientation of axial surface and hinge line (Figure 3.2a). Often the fold type may be recognized from the geological map pattern, but in terrains with high topographic relief this may be difficult (Weijermars, 1997). Folds can also be classified on the basis of dip isogons (Figure 3.2b), which are lines that join points that have equal dip on both sides of a folded layer (Ramsay and Huber, 1987).

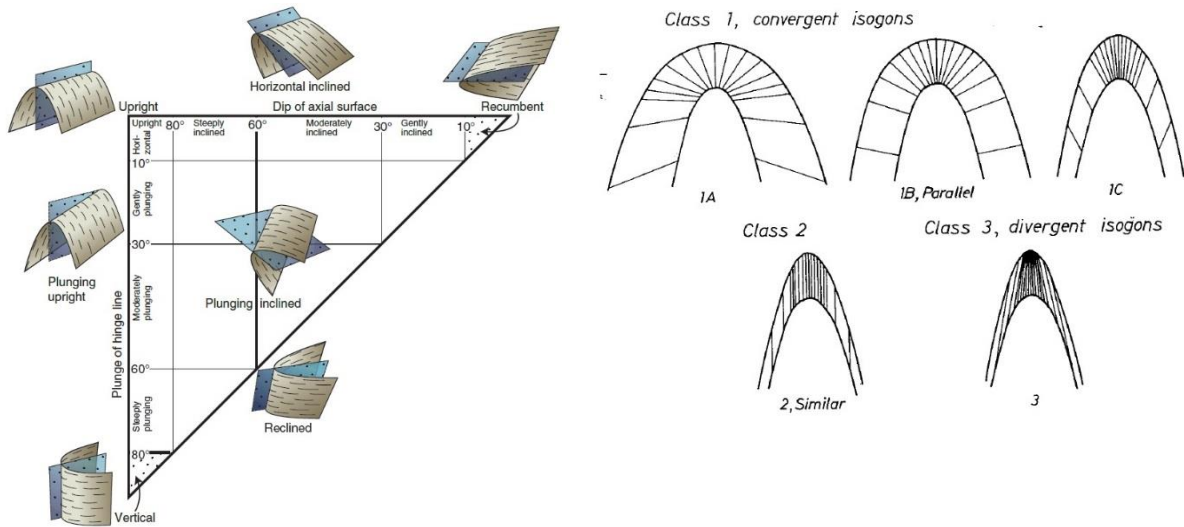


Figure 3.2: a) Fold classes based on the relationship between axial surface dip and plunge of hinge line. Based on Fleuty, 1964. From Fossen, 2010. b) Fold classification based on dip isogons. From (Ramsay and Huber, 1987).

## 4 Methods and material

### 4.1 Fieldwork

Fieldwork was performed in the summer months of 2013 and 2014. Field work during the first summer included recognisance of the area and detailed mapping and sampling of two profiles on the SW fold limb. By the summer of 2014, a working 3D model had been produced from the results of the previous year. Based on this model, a site was picked out for a diamond drill hole. A third profile was also traversed on the NE fold limb during the summer of 2014. Structural measurements of bedding and fracture planes was performed throughout both field periods. A summary of exploration activity is presented in Table 4.1 below. Table 4.2 presents the number of samples analysed by the different methods. For the specific analysis performed on the samples, see Appendix B.

Table 4.1: Summary of exploration activity.

<b>Location</b>	<b>Diamond Drilling</b>	<b>Surface Geochemistry</b>	<b>Total</b>
<b>Vaggecearru Mountain. SE fold limb</b>	1 hole – 69,2 m, 24 samples	2 profiles, 36 rock chip samples	60 samples
<b>Vaggecearru Mountain. NW fold limb</b>		1 profile, 14 rock chip samples	14 samples
<b>Total</b>	1 hole – 69,2 m, 24 samples	3 profiles, 50 samples	74 samples

Table 4.2: Number of samples analyzed by each method.

Method	Material (nr. of samples)
Polarizing light microscopy	24
Inductively coupled plasma optical emission spectrometry ICP-OES	74
Microprobe	4
X-Ray Diffraction (XRD)	3
Thermal Strength Index	4

## 4.2 Equipment

Field equipment included a compass, GPS, hand lens, map, hammer (4Kg) and chisel, safety glasses and notebooks. The compass used was a Silva Ranger. All measurements are corrected by 7 degrees toward geographical north. The GPS is from Garmin, with a horizontal accuracy of 2-3 m.

### 4.3 Geological Mapping

Because the terms used for naming the different qualities are based on chemistry (Table 2.1), it is not useful in the field. When mapping, color and other distinguishing characteristics are used when naming samples and designating stratigraphic sub units.

The mapping strategy consisted of first doing a reconnaissance of the area, looking for light gray quartzite near the contact to the Vagge Formation, as these are known to usually represent good quality quartzite. After some well exposed potentially good locations were found, the investigation consisted of examining visual differences in the rocks, including color variations, mineral content and hardness. The homogeneity of the formation was also investigated, looking particularly for lenses of interbedded shale, silt and clay. Contacts between the Hanglecearru, Vagge and Gamasfjell Formations were mapped on both sides of the fold. When mapping the Gamasfjell Formation, rock types with similar characteristics were grouped together into subunits. Contacts between the subunits were drawn at the most prominent and latterly continuous beds. In the field, a geological map (Siedlecka, 1988) was used as a guide. All field points (samples locations, structural measurements etc.) were saved on GPS and later plotted into ArcGIS. ArcGIS from ESRI together with the extension, sigma mobile from BGS were used to prepare geological maps.

A topographic map (35\_2025, 20m contour lines) from Kartverket was uploaded to ArcGis. Aerial images are from Statens kartverk (2014). Getting a high resolution on the aerial images, required panning over the study area, taking screenshots at maximum zoom. A total of 99 screenshots were taken and merged together, using the software AutoStitch (Brown, 2015). Aerial images and a geological map were georeferenced and uploaded to ArcGIS. The map is projected in WGS 84. UTM zone 35N.

#### 4.4 Surface sampling

Sampling was performed in order to get a representative depiction of the quality of the resource. A total of 50 samples of the Gamasfjell Formation were collected from outcrops on the Vaggecearru Mountain.

Outcrops of the Gamasfjell Formation are easily accessible at the Vaggecearru Mountain and because the mountain is a truncated anticline, samples could be collected from different stratigraphic and structural positions. Three locations were chosen for detailed sampling which would allow comparison between outcrops. At these locations samples were collected along profiles normal to the bedding (there is some divergence from the profiles, due to poor outcropping). The approximate stratigraphic depth (measured by eye) in relation to the Vagge Formation was noted for each sample, later the depth was geometrically estimated. The original names are kept and referred to in this thesis. However, note that the numbers do not represent the stratigraphic depth. The geometrically estimated depth is considered more accurate, and used in data analysis and modeling. The estimated depth of each sample is given in Appendix E, the depth will also sometimes follow the sample name in the thesis.

Profile one and two lie on the southeastern fold limb (36 samples), while profile three (14 samples) is located on the northwestern limb. The locations of the profiles are shown in Figure 4.1. Profile 1 and profile 2 are enhanced in Figure 4.2. The coordinates of each sample is presented in Appendix A. Note that, chemical data from profile 3 is not analyzed, or used in any of the calculations. The visual characteristic logged in the field are however used to draw approximate boundaries on the NW fold limb. Profile 3 will not be discussed further in this thesis.

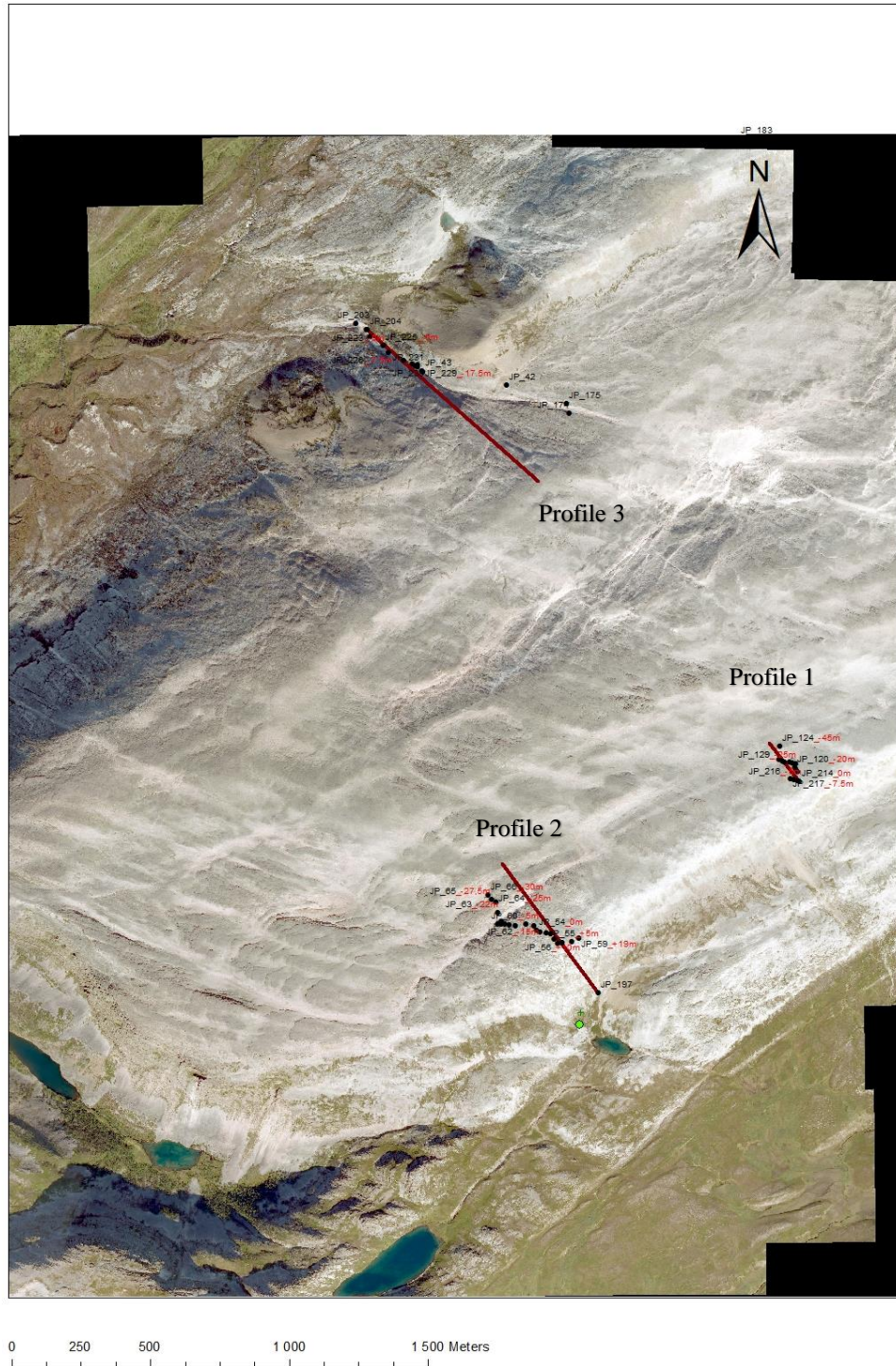


Figure 4.1: Aerial image of the Vaggecearru Mountain with the location of the profiles.

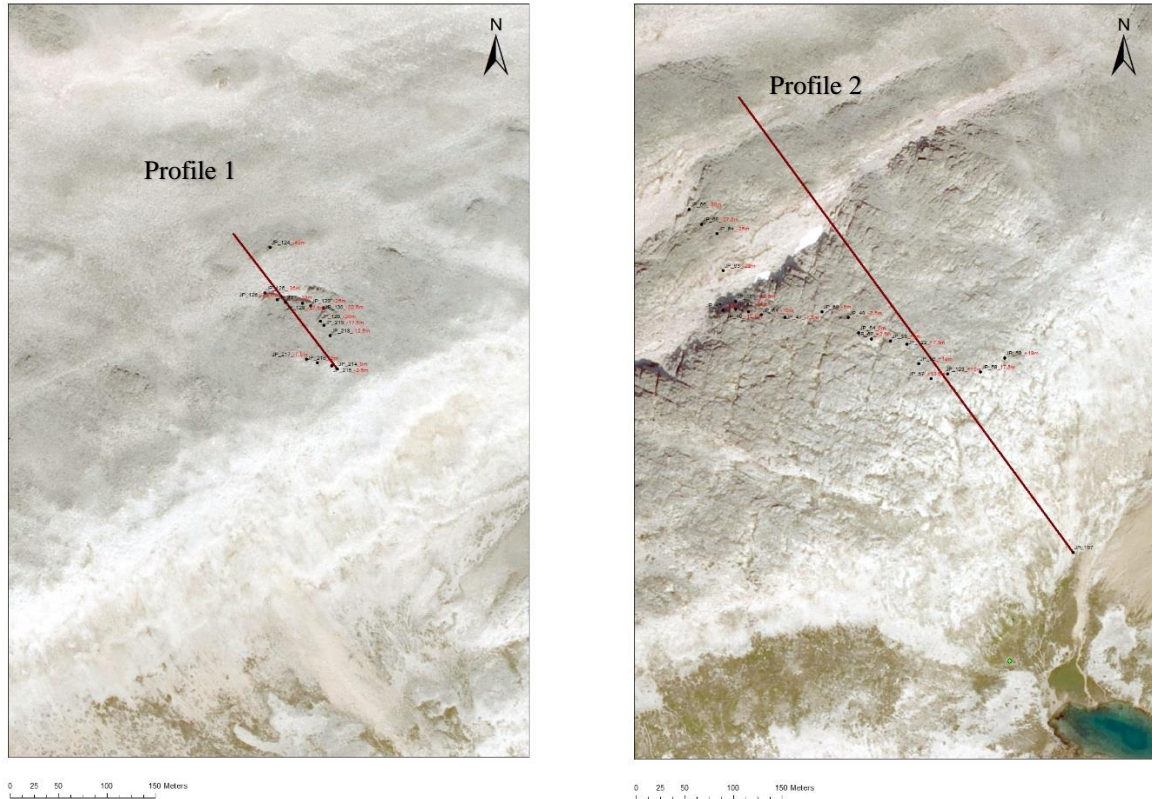


Figure 4.2: Profile 1 (left) and profile 2 (right). Samples collected at outcrops close to profiles.

Samples were collected by chisel and hammer. The desired sample size was 2 kg. Samples were kept in plastic bags, which were marked with sample number and profile number. The sample number corresponded to the approximate depth below the Vagge Formation. GPS coordinates were registered at each sample location.

All samples have been described by color. Only five categories are chosen when presenting the color. The color of Unit B and Unit C could have been divided into several more tints and shades of red, but because no color chart was used, the color description is subjective. Simplifying the categories is therefore considered most practical. The colors used are Light gray, pink, pink/red dark red. Violet is also used in some samples descriptions, but falls under the category dark red when comparing colors.

## 4.5 Crushing and milling

All crushing and milling was performed at Elkem Tana`s laboratories. The samples were crushed using a jaw crusher. The crushed material was put into a miller. After milling, a splitter was used to reduce the amount of material while still preserving the property of the mass being sampled. Two samples of 50g each were prepared. One was sent to laboratory for chemical analysis while the other was kept for reference. All machinery was cleaned with an air hose after each stage of the process.

## 4.6 Microscopy

Thin sections were prepared in the thin section laboratory at the Department of Geology and Mineral Resources Engineering, NTNU. Polarized thin sections prepared 28x48

Of the 50 rock samples collected in the field, 24 samples of quartzites collected at different depths, were selected for petrographic analysis.

Petrographic evaluation of the thin sections was done using polarizing light microscopy at the geology department at NTNU. The microscope used was a Leica DM2500P, micro images were taken with a ProgRes CT3 camera. The microscope was used to describe the mineralogy and texture of the selected samples. The goal was to examine mineralogical and textural changes with depth, focusing particularly on how contaminating minerals appeared.

## 4.7 Electron Micro probe (EMP)

Microprobe analysis was performed on four carbon coated, polished thin sections. These four samples were selected after petrographic evaluation by microscope. They represent quartzites of different color and chemical properties. Phyllosilicates and heavy minerals were characterized by means of microprobe analysis.

Microprobe analysis was performed using a Jeol JXA 8500F. The instrument has five wave dispersive spectrometers (WDS) and one electron dispersive spectrometer (EDS). The instrument was operated with an acceleration voltage of 15 kV, a beam current of 20 nA, with a beam diameter of  $\mu\text{m}$ .



#### 4.8 X-Ray Diffraction (XRD)

XRD analysis and sample preparation was performed at the chemical/mineralogical laboratory at the Department of Geology and Mineral Resources Engineering, NTNU. XRD was used to confirm the presence of hematite. Three samples were selected for evaluation, representing a light gray quartzite (Pr2+17,5), a red quartzite (Pr2-7,5) and a dark red quartzite (Pr2-30).

Prepared samples between 10-40 micron were analyzed using Bruker D8 advance X-ray diffractometer. Cu-K alpha radiation was used and recorded by a detector from 3° to 65° (2θ). Total scan time was 71 minutes. The software Topas from Bruker AXS, was used for quantification (Rietveld method)

#### 4.9 Inductively coupled plasma optical emission spectrometry (ICP-OES)

All 74 samples were sent to Erimisa in Spain, where they were subjected to ICP-OES analysis, measuring 9 major elements in oxides ( $\text{Al}_2\text{O}_3$ ,  $\text{Fe}_2\text{O}_3$ ,  $\text{TiO}_2$ ,  $\text{CaO}$ ,  $\text{Na}_2\text{O}$ ,  $\text{K}_2\text{O}$ ,  $\text{MgO}$ ,  $\text{MnO}$ ,  $\text{P}_2\text{O}_5$ ). In addition,  $\text{B}_2\text{O}_3$  was measured in six samples. The samples were prepared and analyzed to the approved Erimisas procedure.

#### 4.10 Heat Index (HI) and Thermal strength sampling (TSI).

Four representative samples (Pr1-0, Pr1-30, Pr2-2,5, Pr2-7,5) were collected in order to test the heat index (HI) and thermal strength index (TSI) of the quartzite. The samples were partially prepared in the field by crushing and sieving (20-25 mm) the samples to approximately 500g. The partially prepared samples were delivered to Elkems laboratory in Tana, where further preparation and analysis were performed, using the Elkem method (Fiskaa method). The method is described by Aasly (2008) and Johannesen (1998). The names of the samples unfortunately became mixed up after the test, so interpretation of the individual samples are not performed in this thesis.

#### 4.11 DDH positioning and core logging

DDH VR-14-01 was drilled in 2014 on the SE side of the Vaggecearru Mountain, Table 4.3 presents the collar and survey data. The positioning was chosen on the basis of the 3D working model generated from data collected the previous summer. The drill core was kept in wooden boxes with a length of 1,07m. Before studying the core, it was washed and photographed (Appendix F).

Table 4.3 Collar and Survey of DDH - VR-14-01

<i>Collar</i>	<i>East</i>	<i>North</i>	<i>Elevation</i>	<i>Depth</i>
<i>VR-14-01</i>	560499.41	7822072.35	331	69.2
<i>Survey</i>	<i>Depth</i>	<i>Dip</i>	<i>Azimuth</i>	
<i>VR-14-01</i>	69.2	60.0	325.0	

Both geological and chemical analysis was performed on the core. The geological study followed the same procedure as in the field e.t, examining colour variations, mineral content, degree of lithification and looking for lenses of interbedded shale/silt/clay. For the chemical study, the whole length of the core was sampled. The core was manually split into two halves (lengthwise), where one halve was prepared for chemical analysis and the other preserved. The length of each sample was chosen on the basis of color e.t, the core was divided into unequal length segments of similar color.

## 4.12 Structural measurements

### 4.12.1 Bedding

Orientation data was collected using a compass with a built inn clinometer. The orientation of the bedding was measured for its dip and dip azimuth. Data collection comes from strata belonging to the Hanglecearru, Vagge and Gamasfjell Formation. Stereographic projection was used to process the data. The structural measurements form the basis for the 3D model.

### 4.12.2 Fractures

The strata of the Gamasfjell Formation is strongly affected by several joint sets that in many areas have caused the quartzite to break into blocks. Weathering along these joints have altered the rock in close proximity, which has resulted in a loss of mechanical strength and given the quartzite a sugary and porous texture (Fjellanger, 2009). Elkem uses the term “sugar quartz” for very altered quartzite. These are undesirable as a product and can drastically affect the tonnage of the resource (Aasly and Ellefmo, 2014). Part of the field work was therefor to map the joint sets, including their orientation, spacing, persistency, material filling and the interrelationship between

sets. Data collection comes from strata on the southeastern fold limb. The orientation of the joint plains were measured for their dip and dip azimuth. Stereograms were used to analyze the data.

#### 4.13 Modeling

Different types of data were merged into a model by data conversion. Data included DDH data (VR-14-01), topographic contours from Statens Kartverk (35\_2025, with 20m contour lines), aerial images and the geological map produced in this thesis. All structural, lithological and geochemical data from field mapping were also imported. Horizons were constructed from bottom to top by using input data, combined with geological analysis during modeling. DDH data came at a later stage, and the model was refined, with respect to the new information provided. The 3D model comes attached with the thesis, and can be viewed in Leapfrog Viewer.

Input data:

- Topography was created by importing topographic contours from Kartverket.
- The geological map produced in ArcGis was digitized and imported, giving the interpreted boundaries between the different horizons.
- Geometric facts were accumulated from the structural measurements and imported, giving the average strike and dip of outcropping horizons (Appendix H).
- DDH data was used indirectly to manually move each horizon so that they intercepted the boundaries in the core.
- Aerial images, a geological map, all structural, lithological and geochemical data was imported to assist modeling.

## 5 Results

### 5.1 Map description and lithology

The constructed geological map presented in Figure 5.1, shows the main geological formations and subunits in the study area, including the Hanglecearru Formation (blue), the Vagge Formation (green) and the Gamasfjell Formation (yellow, red and violet). The Gamasfjell Formation has been divided into three subunits based on visual characteristics. Boundaries are separated into observed, gradational (also observed), inferred (based on aerial images), and conjured (based on geological analysis).

In Figure 5.2 a cross section (A-B) shows the geometry of the fold and the relationship between the formations and units at the Vaggecearru Mountain. Cross section A-B extends from Lille Leirpollen at the NW flank to Vaggedalen on the SE flank. DDH VR-14-01 is drawn in as a black line at the SE limb.

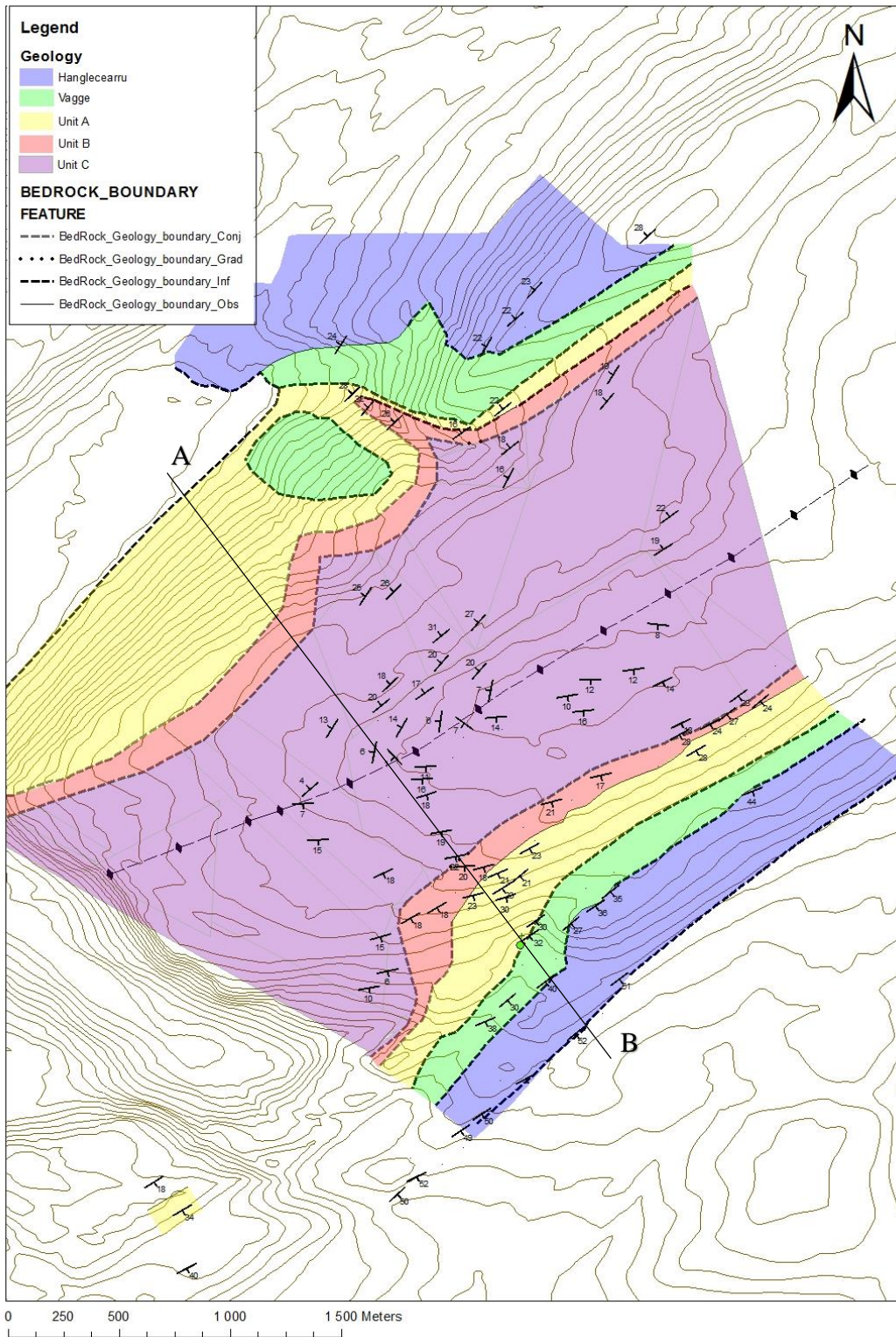


Figure 5.1: Geological map created in ArcGis, Showing the formations, sub units and boundaries in the study area. Bedding measurements and the axial plane trace is also shown.

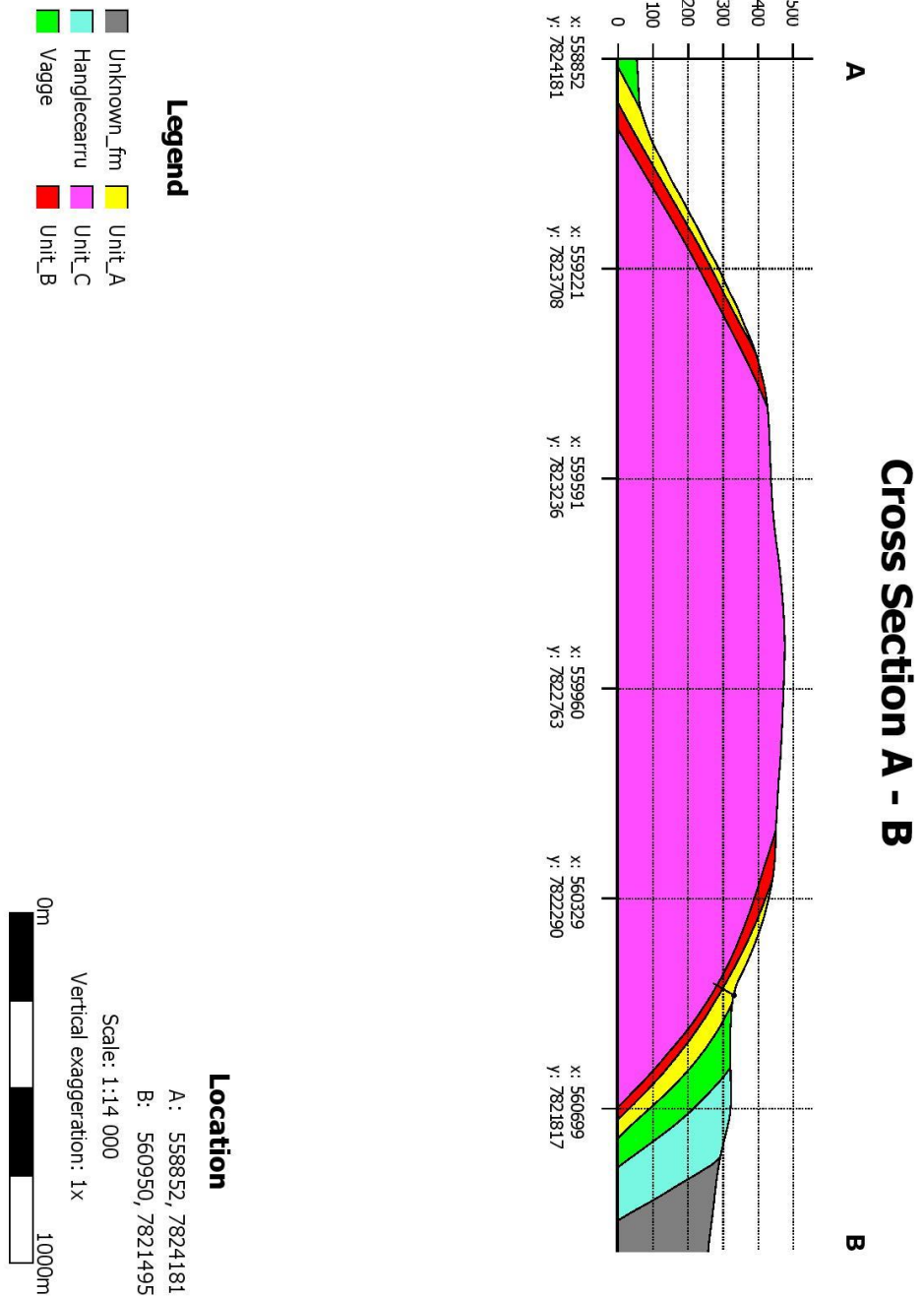


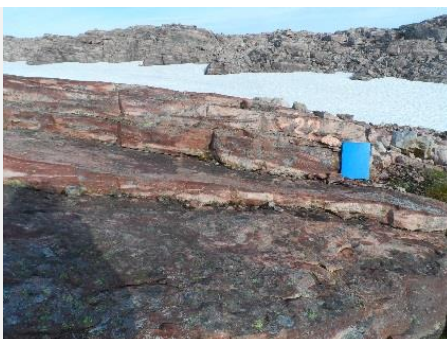


Figure 5.2: Cross section of the fold. Extending from Lilleirpollen (A) to Vaggedalen (B).

The Gamasfjell Formation is relatively homogeneous, but features such as color, sedimentary structures, mineralogy, texture and chemistry undergo changes with depth. These changes form the basis for separating the Gamasfjell Formation into three sub units. A detailed description of the three sub units will be presented in chapter 5.10. A summary of the defining field characteristics of the sub units are presented in Table 5.8 below.

Tabell 5.1: Field characteristics of each sub unit.

<i>Unit</i>	<i>Outcrop</i>	<i>Primary colors</i>	<i>Sedimentary structures</i>	<i>Other</i>
<i>A</i>		Light Gray	Massive, with no visible internal structures.	Circular cavities, resilient.
<i>B</i>		Pink and Red	Mostly massive, with “smeared out” red bands.	Altered quartzite in proximity of joints, circular cavities.
<i>C</i>		Pink, red, brownish red and violet.	Crossbedding (unidirectional and bidirectional).	Lenses of clay, alternating grain size, resilient.

In outcrop the quartzite ranges from light gray to pink/red and violet. The upper part of the formation is light gray in color and thick bedded, while the rest of the formation displays alternating colors of red. The boundary between the gray and red quartzite is distinct and continuous along strike and defines the boundary between Unit A and Unit B. Within the red quartzite of Unit B, the beds alternate between light and dark colors of red. These alternating layers follow bedding planes to a certain degree, but are often smeared out.

With increasing stratigraphic depth, several unique features appear. The color of the quartzite gradually becomes more varied and includes more shades and tints of red (pink, red, dark-red, brownish red, violet). Intensely colored lamina, makes sedimentary structures visible. Lenses and layers of silt and clay are sandwiched between layers of quartzite. Lastly, fractures are closed and the rock seems more resilient. These features were used to define Unit C. The boundary separating Unit B and C is gradational.

In outcrop the surface of the quartzite is often stained with a yellow-brown secondary color (rust color) by iron hydroxide. This is mostly seen along fracture planes. Iron hydroxide usually only penetrates a few millimeters below weathered surfaces, but can also be seen in the upper part of the drill core.

## 5.2 Sedimentary structures

Several bedding types are observed, including massive bedding and crossbedding. The light gray quartzite is massive and seemingly without any internal structures, but small cavities are characteristic. Cross bedding is more visible in the colored quartzite, particularly below depths of about 50m (Unit C), where thin layers of hematite define the sets. The main bedding is on average about 30 cm thick, while the thickness of the cross-beds range from a few millimeters to centimeters. Both unidirectional and bimodal (suggesting alternating currents) cross-bedding patterns were observed. The above lying pink/red quartzite (Unit B) alternates in color, but the red color does not define the bedding very well. Cavities are also characteristic of Unit B. Figure 5.3 shows examples of sedimentary structures observed in the field.



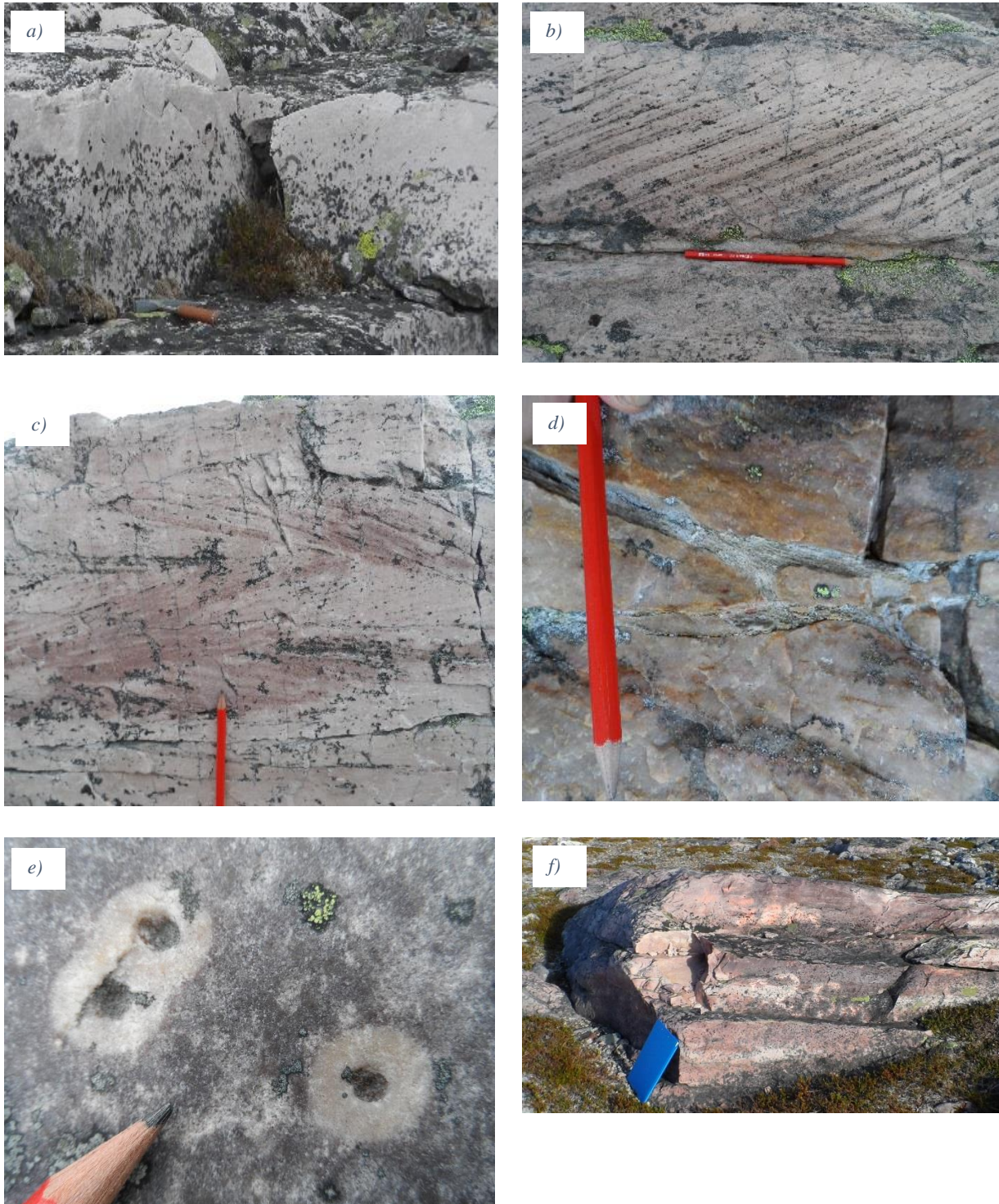


Figure 5.3: Field observation of different sedimentary structures. a) Massive bedding in Unit A. b) Unidirectional crossbedding in Unit C. c) Bimodal crossbedding in Unit C. d) Lense of clay sandwiched between quartzite, in Unit C. e) Small cavities, surrounded by clay. f) A person climbing a rock face with a blue mat.

## 5.3 Microscopy

### 5.3.1 *Texture:*

Generally the Gamasfjell Formation is fine to medium grained, but ranges from very fine to very coarse. Grains are very well rounded (although overgrowth cement often makes grains appearing angular). The Gamasfjell Formation can be classified as an orthoquartzite/quartz arenite by the abundance of quartz grains (>95%) and because fracturing occurs between grain boundaries.

While cementation is normally extensive, giving an interlocking texture, outcrops at several locations are moderate to poorly cemented (grains are easily scraped off). The poorly cemented rocks do not form uniform layers and are mostly found in proximity of joints. With increasing depth the texture changes from equigranular to more bimodal and layered.

### 5.3.2 *Mineralogy*

#### *Detrital:*

**Quartz:** The Gamasfjell Formation is dominated by quartz. This is reflected in the bulk chemical analyses, showing a silica content of over 99%. Both mono- and polycrystalline varieties are present. Monocrystalline grains dominate. The number of polycrystalline grains increases with depth. Quartz cement is present as overgrowths on detrital grains. The rounded outline of the detrital grain is in many cases visible by small dust-like inclusions, but often this line is absent. A variety of grain contacts exist, mainly strait, concavo-convex and sutured. In some of the uppermost samples, grain boundaries interlock at 120 degree triple junctions. With increasing depth, boundaries become more and more sutured. Crystal strain is low, with grains being mostly uniform or slightly undulus in extinction. Figure 5.4 shows some examples of the textures described above.

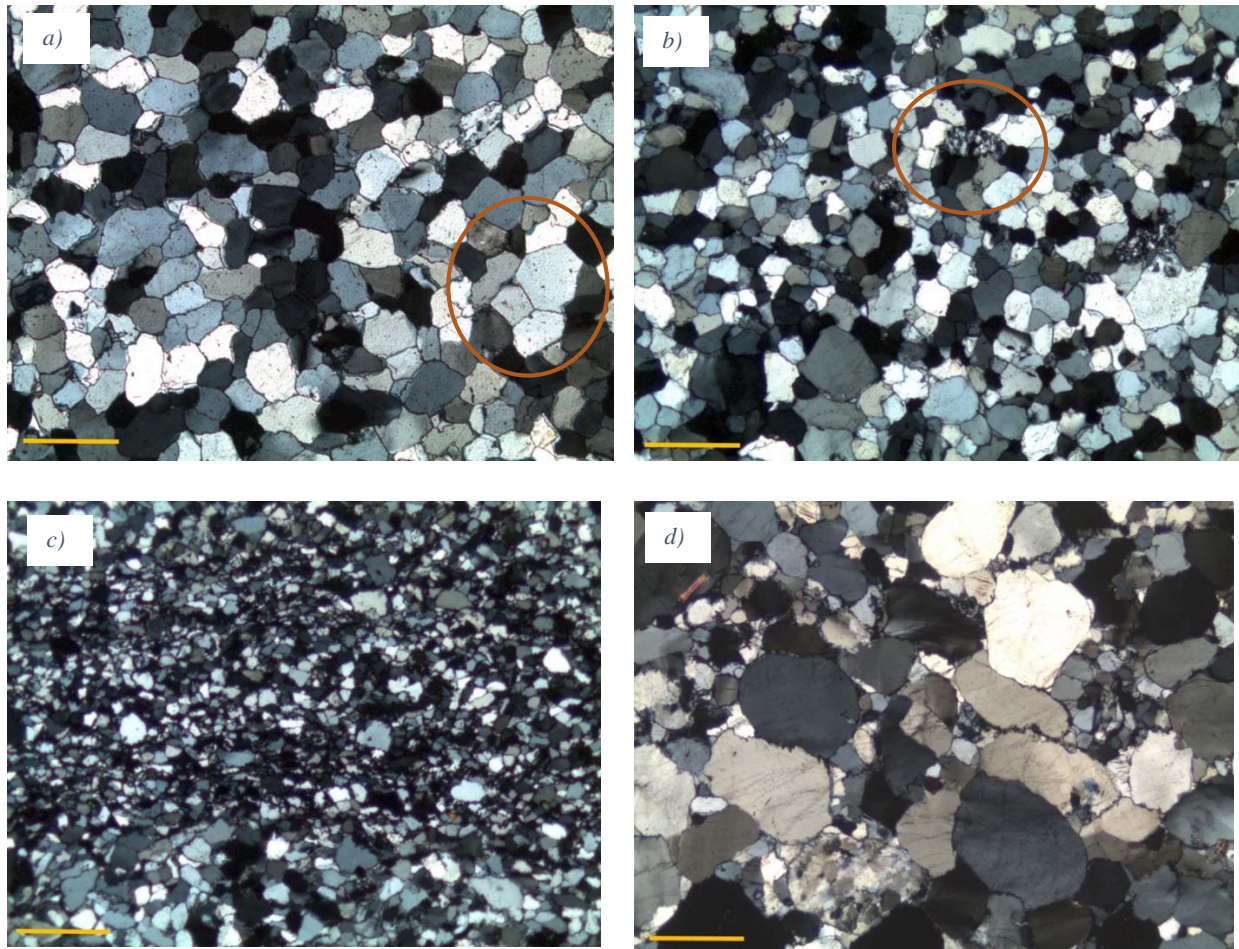
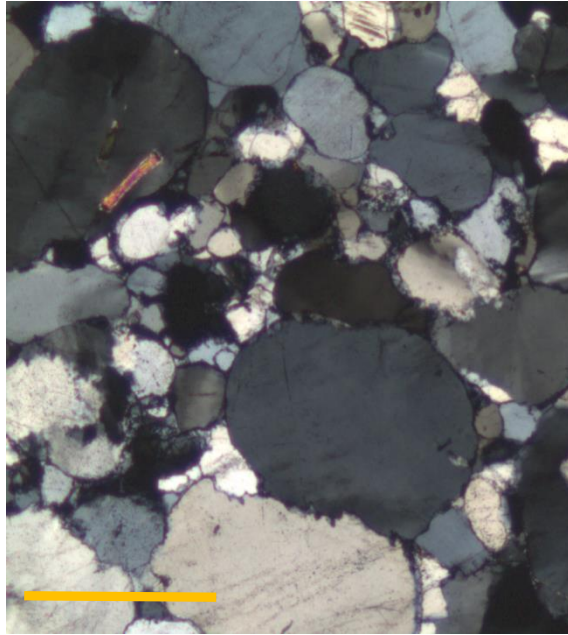


Figure 5.4 Quartz grains at varies depths: a) Tripple junctions between grain (Sample. Pr2+13,5 at 16,5m depth). b) Polycrystaline grains (Sample Pr2-15 at 53m depth). c) Layers of medium grained and fine-very fined grained quartz (Sample Pr2-30 at 69,5m depth). d) Bimodal distribution (poorly sorted) of very coarse grains and fine grains, notice also polycrystaline grains (Pr1-45 at 76m depth). (Scale bar: 1 mm).

**Micas:** The only detrital mica mineral identified is muscovite ( $\text{KAl}_2(\text{AlSi}_3\text{O}_{10})(\text{OH})_2$ ), which is present in trace amounts in several samples. The grains are often bended due to compaction and sometimes present as inclusions in quartz grains. Muscovite appears colorless in plane polarized light, has an elongated shape and 3. order interference colors (Figure 5.5).



*Figure 5.5: Muscovite inclusion in a quartz grain. (Sample PR1-45) at 76m depth. (scale bar: 1 mm)*

#### *Accessory:*

Heavy minerals are found in all samples, the amount increases with depth and Unit C contains the highest abundance. Heavy minerals were characterized by microprobe as mainly zircon, tourmaline and rutile, trace amounts of monazite was also observed. Rutile and Zircon can also be distinguished in microscope (Figure 5.6). Rutile often present as inclusions in quartz grains, taking the form of acicular needles and blades. Rounded detrital varieties are also present. Both rounded and angular varieties of zircon appear and generally have high relief, and high order interference colors. The heavy minerals are generally more concentrated in fine grained layers, often mixed with hematite and clay.

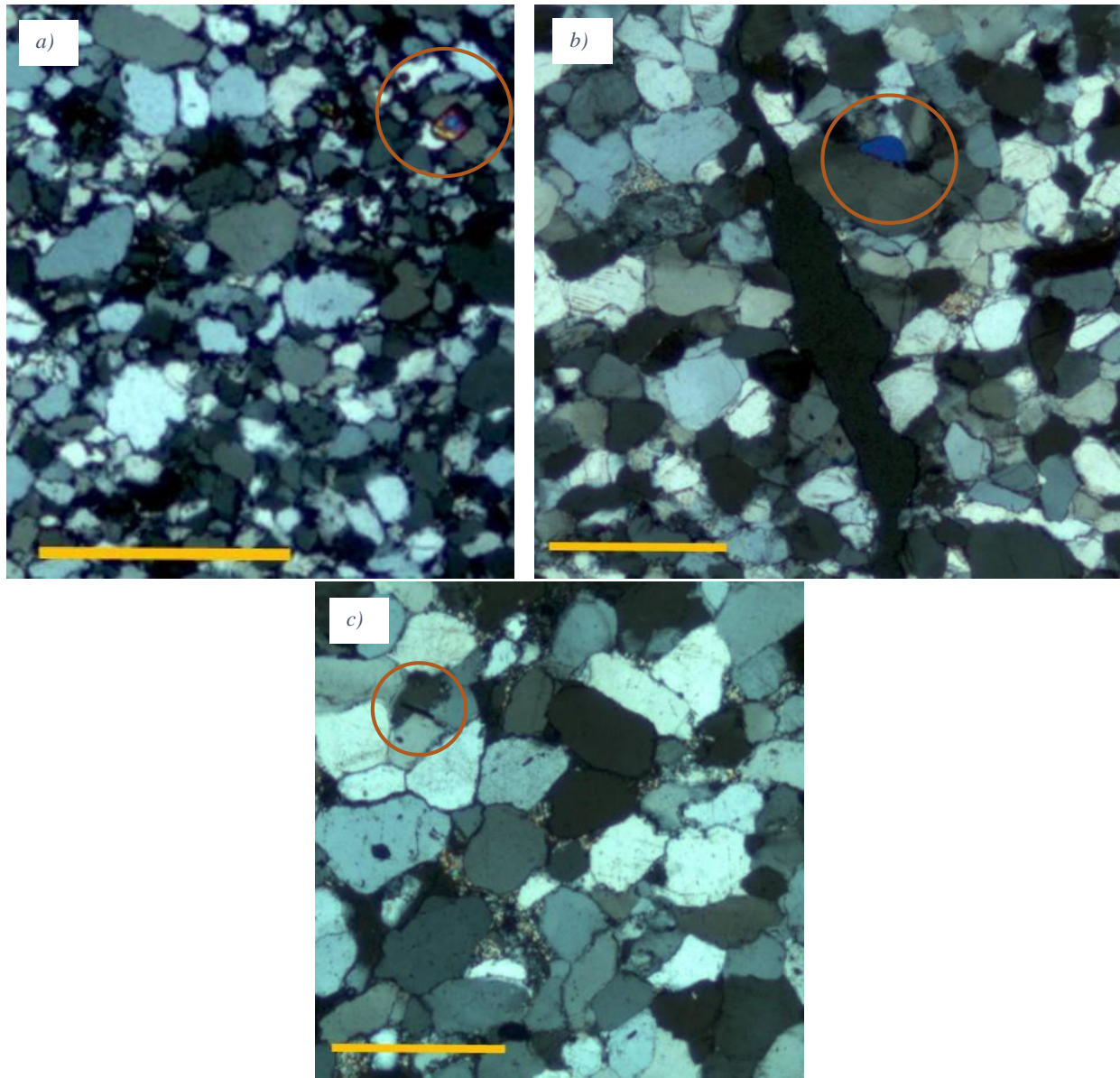


Figure 5.6: a) Angular zircon grain showing high order interference color (Pr2-30, at 69,5m depth). b) Rounded tourmaline grain (Blue) between quartz grains. Note the fracture that follows grain boundaries (Pr2-22, at 61,5m depth). c) Needle shaped rutile inclusion (Prw+13,5, at 16,5 m depth). Scale bar: 1 mm. Note that images are distorted in relation to each other, due to cropping and stretching.

*Chemical constitutes:*

**Sericite:** In microscope, sericite appears very fine grained with a pale greenish color. Sericite mostly occurs in patches occupying grain shaped/sized pore spaces (Figure 5.7). The presence of sericite was verified by microprobe analysis, which revealed its chemical formula. Microprobe analysis reveals a Si/Al ratio of approximately 1/1 (Table 5.1), it also contains Potassium, differentiating it from pyrophyllite. A small amount of sericite is found in all samples.

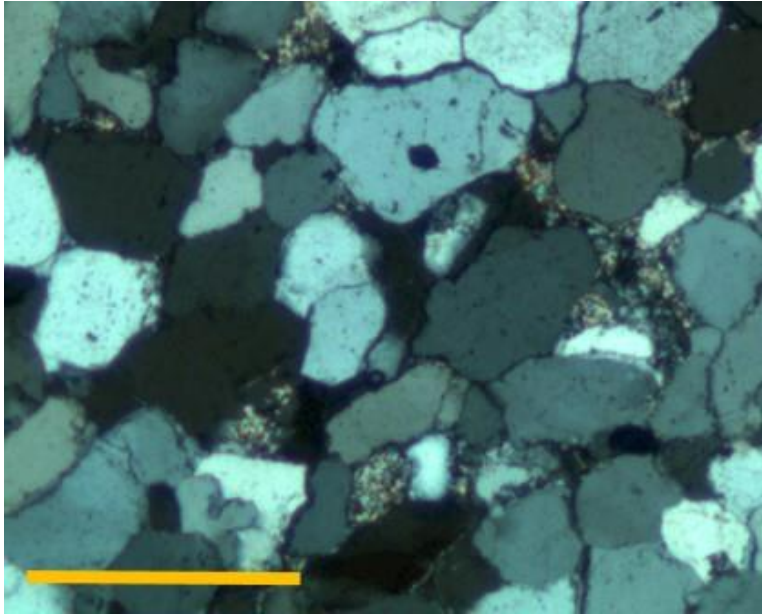
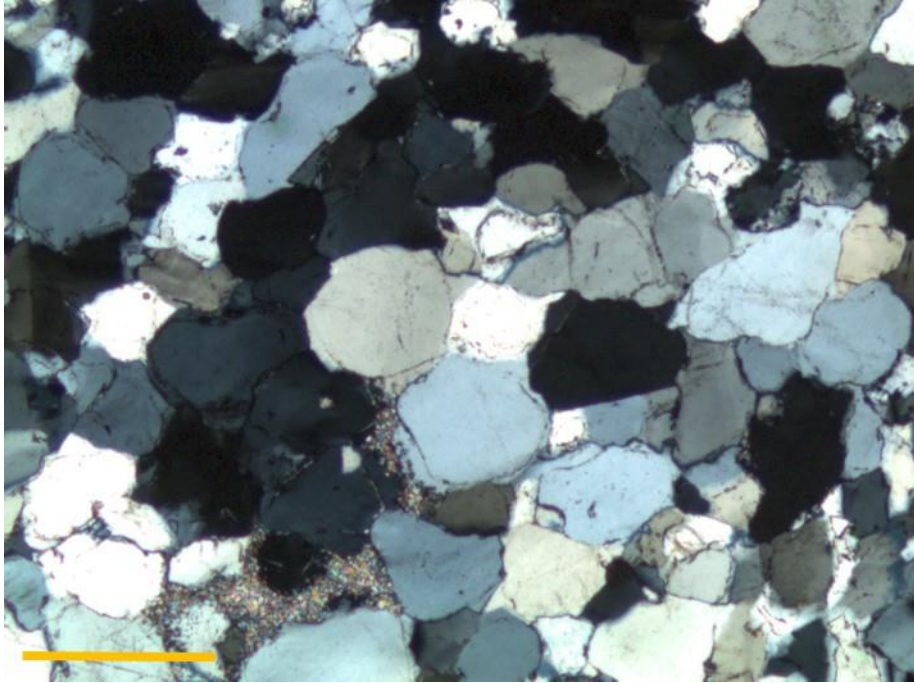


Figure 5.7: Grain sized/shaped pores filled with sericite. Sample (PR2+13.5) at approximately 16.5m depth. (scale bar: 1 mm).

**Pyrophyllite ( $\text{Al}_2\text{Si}_4\text{O}_{10}(\text{OH})_2$ ):** In microprobe, pyrophyllite is revealed by its chemical formula, which is characterized by a Si/Al ratio of 2 (Sauro, 2014) (Table 5.1). Pyrophyllite seems to be the dominant phyllosilicate, with most of the analyzed matrix having a Si/Al ratio of 2. Pyrophyllite can also be distinguished indirectly in microscope, as the process of forming pyrophyllite involves the reaction below, between kaolinite and quartz, which consumes quartz (Dyar et al., 2008):



Figure 5.8 shows a patch of pyrophyllite surrounded by the etched remains of quartz cement. The reaction has here consumed much of quartz, leading to sutured grain boundaries.



*Figure 5.8: Etched quartz bordering pyrophyllite. Note the dust like rims covering detrital quartz grains. From sample (PR2-25) at 64m depth (scale bar: 1 mm).*

**Hematite:** Present in most samples, increases rapidly at 40-50m below Vagge. Hematite is present around detrital grains as well as between grains overgrowths. Hematite is also often concentrated in bands, mixed with clay (Figure 5.9). Hematite was verified by XRD analysis (Figure 5.10).

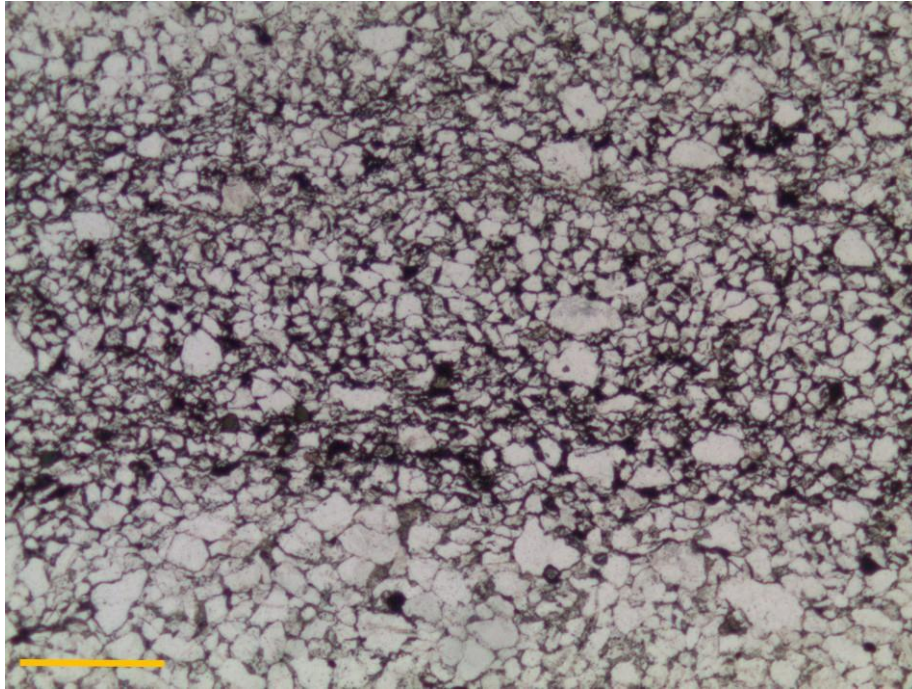


Figure 5.9: Plane light microimage of sample (PR2-30) at approximately 69.5 m depth. Alternating layers of medium and fine-grained quartz, notice how hematite is concentrated in the fine-grained fraction. Scale bar: 1mm.

Table 5.1: Chemical composition (%) of the clay minerals in the Gamafjell Formation, based on microprobe analysis of samples PR1-27,5, PR2+13.5, PR2-22 and PR2-30.

<b>Pyrophyllite</b>	<b>O</b>	<b>Si</b>	<b>Al</b>	<b>K</b>	<b>Mg</b>	<b>Fe</b>
<b>Average:</b>	65,6	23,1	11,0	-	-	0,1
<b>Max:</b>	69,2	25,3	12,4	-	-	0,2
<b>Min:</b>	62,8	20,9	9,8	-	-	0

<b>Sericite</b>	<b>O</b>	<b>Si</b>	<b>Al</b>	<b>K</b>	<b>Mg</b>	<b>Fe</b>
<b>Average:</b>	59.6	19.2	14.4	3.8		1.8
<b>Max:</b>	63.1	23.3	19.2	5.3		5.4
<b>Min:</b>	51.6	15.6	10.3	2.7		0.1



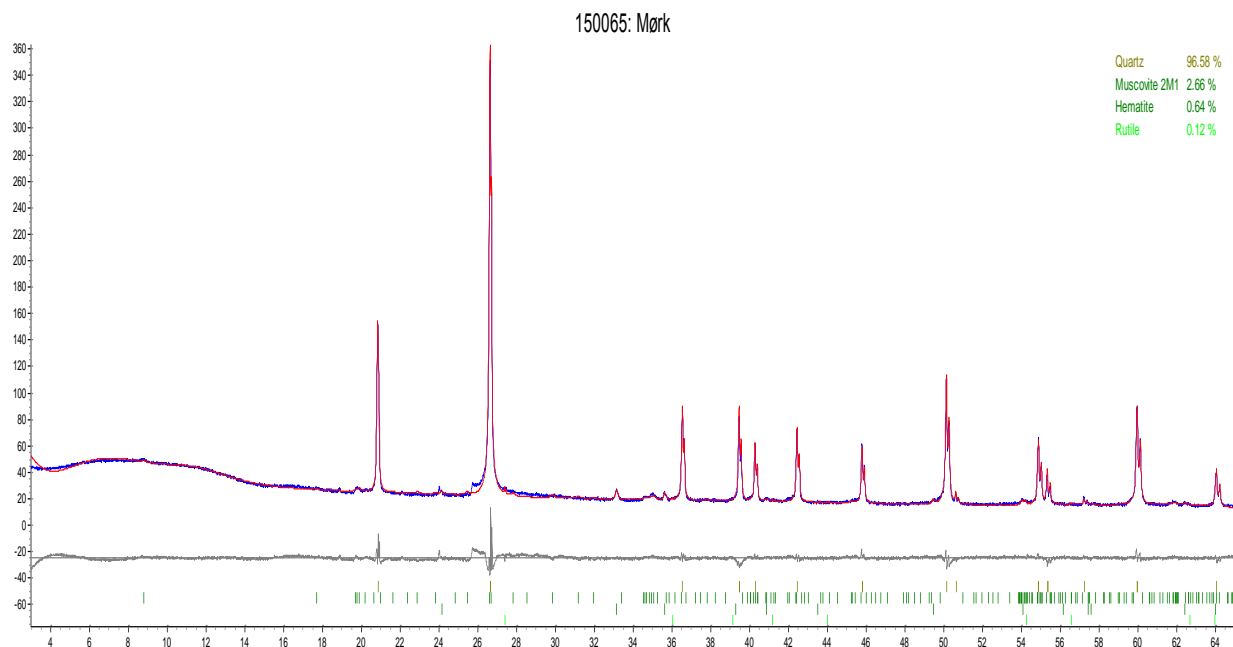


Figure 5.10: XRD analysis of sample PR2-30, showing 0.64% hematite. Note that all clay minerals are categorized as muscovite by XRD.

## 5.4 Geochemistry

### 5.4.1 Bulk geochemical characteristics:

Appendix E presents all the geochemical results, together with depth. This section will present chemical data in the form of diagrams. The three units are recognized by means of bulk chemical analysis. Figure 5.11 and Figure 5.12 show the percentage of samples that fall into categories divided by 0,1% for  $\text{Al}_2\text{O}_3$  and 0,025% for  $\text{Fe}_2\text{O}_3$ . Each category is again divided into sub surface and surface samples. The diagrams are based on the 60 samples collected at the SE fold limb.

As an example, for Unit B, 8 samples (43 % of total samples of Unit B) have an  $\text{Al}_2\text{O}_3$  content between 0,4-0,5%, 5 (26 %) of the samples were collected from the drill core and 3 (16 %) of the samples are from outcrops on the surface. This means that 5/8 or 62,5 % of the samples in this category are from the drill core. When looking at the iron distribution for each unit, one can see that subsurface samples gather further to the right of the diagrams, showing that the general trend is that samples collected in outcrop are purer than those collected from drill core. For  $\text{Al}_2\text{O}_3$ , the subsurface and surface samples do not deviate much.

Unit A is typically low in both iron and aluminum. Unit B has a higher and more variable iron content, while aluminum is relatively low (most samples are below 0,5 %). Unit C has both a higher aluminum and higher iron content.

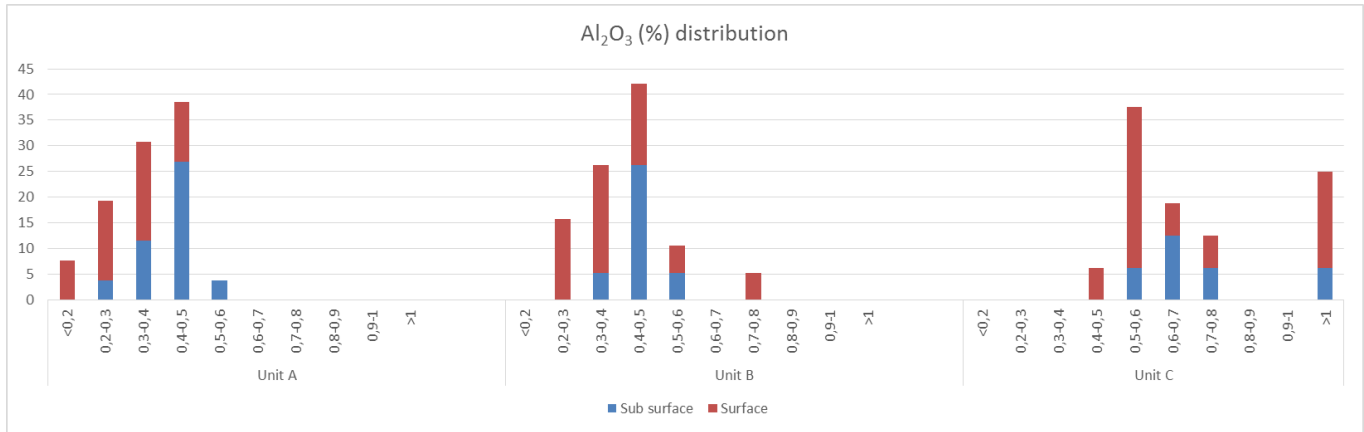


Figure 5.11 Al<sub>2</sub>O<sub>3</sub> distribution withing each sub unit. Sub surface and surface sample are differentiated, as seen, subsurface and surface samples do not differ much in Al<sub>2</sub>O<sub>3</sub>.

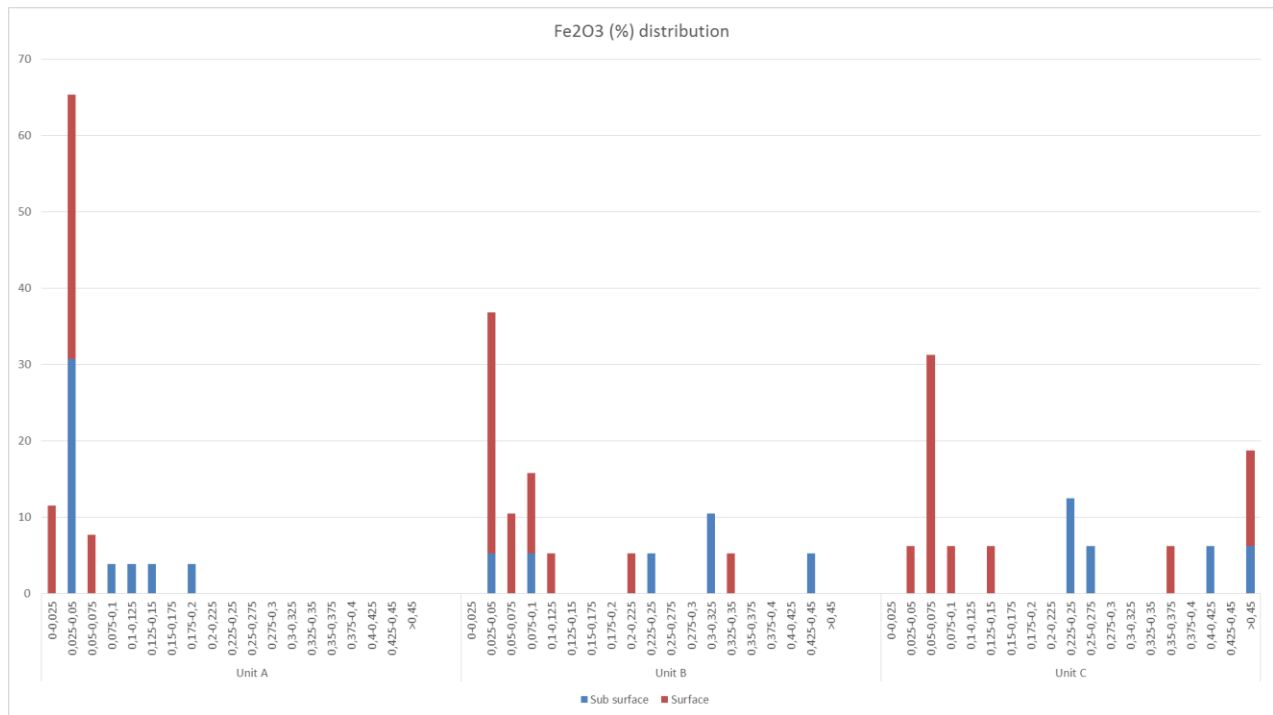


Figure 5.12: Fe<sub>2</sub>O<sub>3</sub> distribution withing each sub unit. Sub surface and surface sample are differentiated, as seen, subsurface samples are typically more rich in Fe<sub>2</sub>O<sub>3</sub>.

### 5.4.2 Chemical relations

Figure 5.13 shows the relationship between  $\text{Al}_2\text{O}_3$  and other common oxides. The scatter diagrams are based on the bulk chemistry of all samples from profile 1, profile 2 and the DDH (Totaling, 60 samples). The strongest correlation is between  $\text{TiO}_2$  and  $\text{Al}_2\text{O}_3$  ( $R^2 = 0,8384$ ), there is also a correlation between  $\text{K}_2\text{O}$  and  $\text{Al}_2\text{O}_3$  ( $R^2 = 0,7708$ ) as well as between  $\text{Na}_2\text{O}$  and  $\text{Al}_2\text{O}_3$  ( $R^2 = 0,5285$ ). The relation between  $\text{Fe}_2\text{O}_3$  and  $\text{Al}_2\text{O}_3$  is weak.

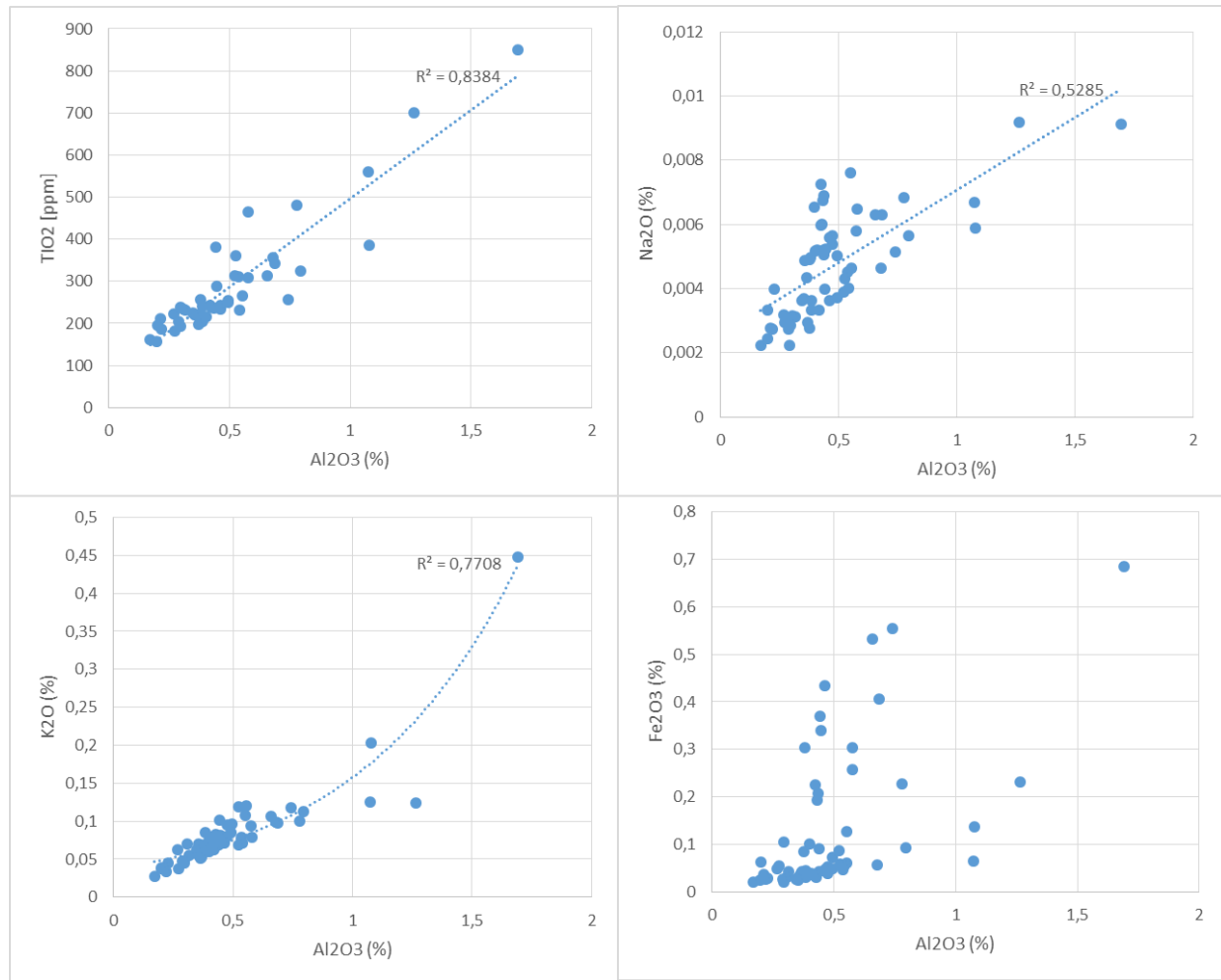


Figure 5.13: Scatter diagrams showing the relation between  $\text{Al}_2\text{O}_3$  and other common oxides ( $\text{TiO}_2$ ,  $\text{K}_2\text{O}$ ,  $\text{Na}_2\text{O}$ ,  $\text{Fe}_2\text{O}_3$ )

## 5.5 Color

Figure 5.14 presents the percentage of samples that fall into each color category for each unit. The figure is based on all field and DDH samples. As can be seen, there is a clear difference in the color between Unit A and B, while Unit B and C are quite similar. Note that the pink and red in Unit A are from two continuous horizons within the unit.

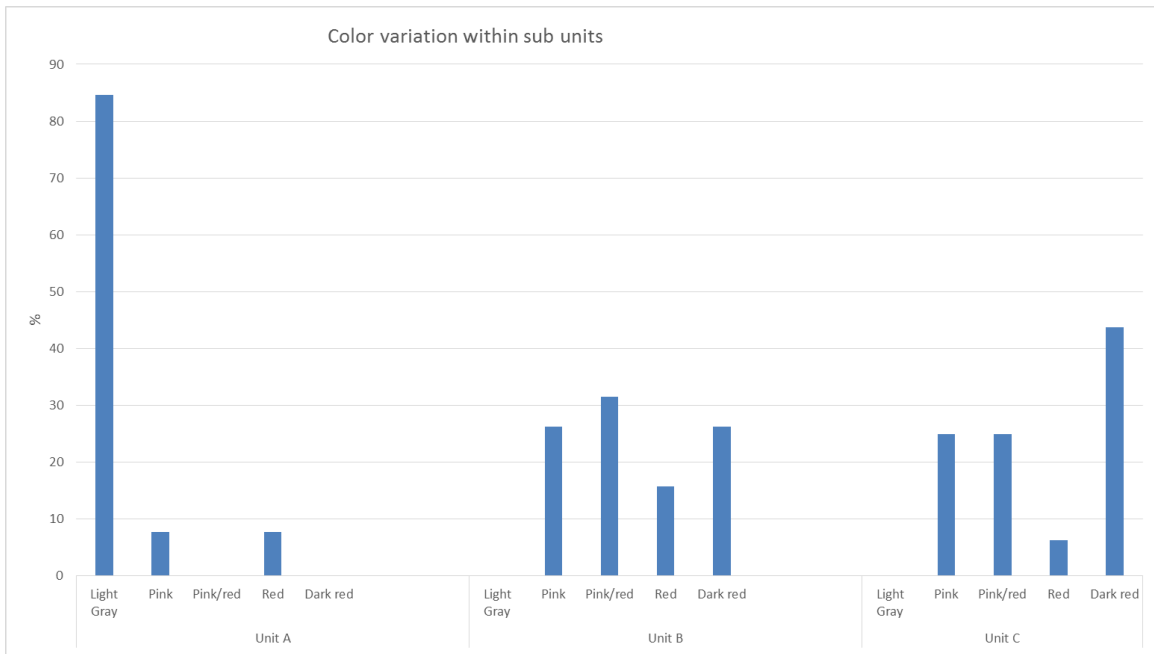


Figure 5.14: The color of the samples collected within each sub unit.

## 5.6 Heat index and thermal strength index:

Results of the HI and TSI of samples Pr1-0, Pr1-30, Pr2-2,5, Pr2-7,5 are presented below. Six results are shown, where two are duplicates. Samples were mixed up, but the HI and TSI is good for all samples.

Table 5.2: Results of TSI test. Six prepared samples, two are duplicates. All samples have a good HI and TSI.

Date	Location	Prepared	Resistance to disintegration					Thermal strength					Avg.	Avg.		
			Index	quality	Weight (g)			Weight (g)	Thermal strength	quality	Avg.					
					25-20	20-10	10-4					4-2			25-20	index
		Sample weight (g)	% 25-20 mm	norm												
27.08.2014	PRI-1	499,210	99,47	1	496,550	0,000	2,090	0,290	0,280	326,010	108,420	13,090	0,730	82,94	A	82,94
		499,530	95,86	1	478,840	16,100	3,820	0,140	0,630	299,650	114,530	13,150	0,870	78,54	B	78,64
27.08.2014	PRI-2	499,730	95,33	1	476,410	21,500	1,520	0,050	0,250	263,740	165,310	11,130	0,620	78,73	B	
		498,400	94,40	1	470,480	27,070	0,260	0,090	0,500	284,840	123,440	4,600	0,770	76,23	B	76,23
02.09.2014	PRI-4	499,200	99,49	1	496,640	1,990	0,060	0,130	0,380	293,580	98,440	4,750	0,610	74,11	B	99,53
		499,170	99,58	1	497,080	0,000	1,640	0,050	0,400	284,160	129,190	4,250	0,200	76,77	B	

## 5.7 Stratigraphy:

### 5.7.1 Lithological logs:

Figure 5.15 presents simple stratigraphic columns of the two profiles and the core log. The thickness of the profiles were measured in the field relative to an arbitrary starting depth, the depth was later estimated geometrically. There is therefore some margin of error. Displaying the logs side by side shows that beds are consistent throughout the strata, that is, red and gray beds found at the surface are also found in the subsurface, at approximately the same stratigraphic depth.

The stratigraphic relations between the different units in each log is briefly described below. A more detailed description of each unit is presented in the chapter 5.10.

**Profile 1:** The log starts at 26m below the Vagge shale. Light gray quartzite (Unit A) extends to depth of about 38m. Pink/Red quartzite (Unit B), extends down to 58m, Unit C lays below 58m.

**Profile 2:** The log starts at the boundary to the Vagge shale. Light gray quartzite (Unit A) extends down to an approximate depth of 38m. Unit A includes two sub horizons of red quartzite. The first horizon is ~ 0,5m thick and stretches from ~ 17m -17,5m. The second horizon is ~1,5m thick, from ~ 28,5 - 30m. Red quartzite (Unit B) extends from 38 to 56m. Unit C lays below 56m. Note that the boundary between Unit B and C is miscalculated in the 3D model, in the location of profile 2. This is discussed in chapter 6.4.

**VR-14-01 (DDH):** The log starts at ~2,3m below Vagge contact. The upper 3,5m is covered by iron hydroxides, giving it a rusty brown color. Light gray quartzite (Unit A) extends to a depth of 38m. Unit A includes two red, sub horizons. The first is 1,1m thick and extends from 16,7 - 17,8m. The second is 2,1m thick and extends from 22,9 - 25,0 m. Red quartzite (Unit B) extends from 38m to 56m. Unit C lays below 56m.

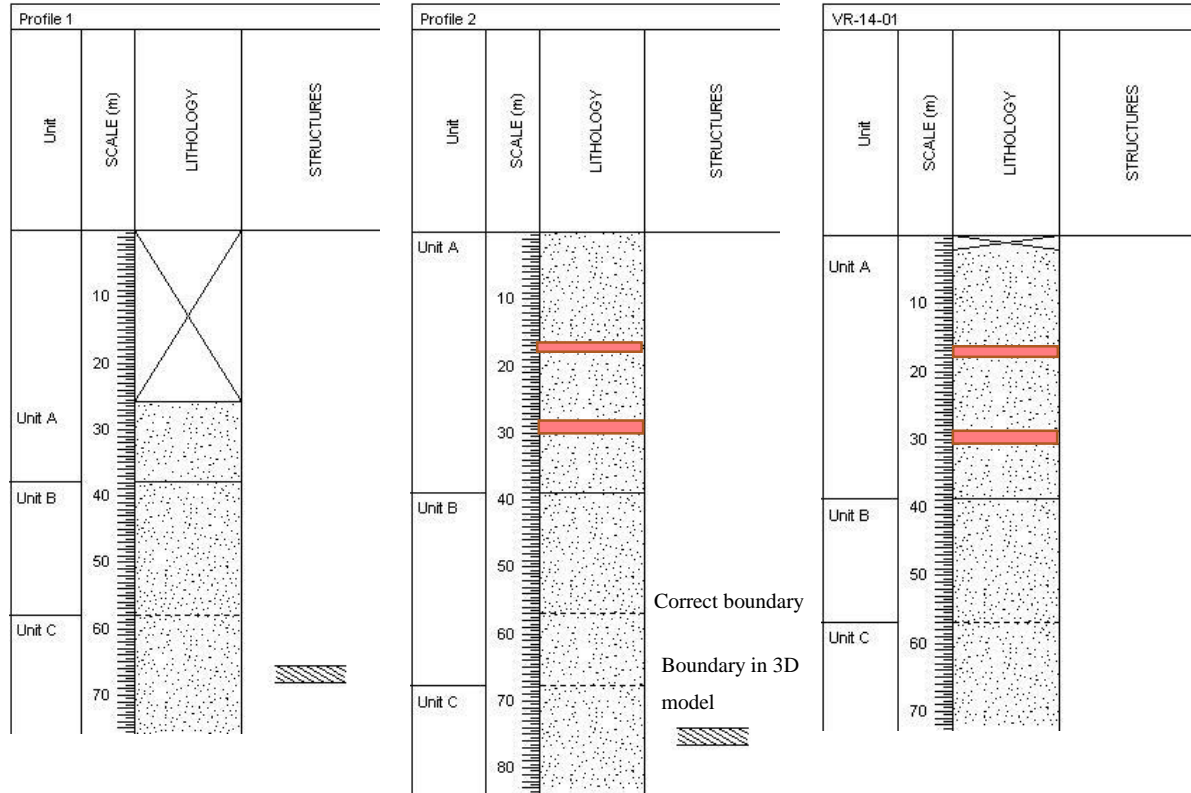


Figure 5.15: Lithological logs of Profile 1, Profile 2 and DDH-VR-14-01. Sedimentary structure observed in outcrop were not observed in the DDH core. Boundaries defined in the field, correspond well with the boundaries in the DDH core.

### 5.7.2 Geochemical log:

In Figure 5.16 the main contaminating chemistry of the two profiles and the DDH are plotted against depth. The figure shows that there is a good correlation between the profiles and the DDH in relation to depth. In all three the  $\text{Al}_2\text{O}_3$  increases suddenly between 50 and 70 meters depth. The  $\text{Fe}_2\text{O}_3$  content varies more. Profile 1 and the DDH have a similar trend, showing spikes between 40-50m and between 55-60m. Profile 2 has a lower  $\text{Fe}_2\text{O}_3$  content, which first increases below 65m. The  $\text{TiO}_2$  amount increases gradually and shows is very similar trend to the  $\text{Al}_2\text{O}_3$ . The drill core is most representative of the chemistry and depth of the different units. This is because it is continuous and includes the thin silty layers that are often absent at the surface due to weathering (Størseth and Wanwik, 1992). However, the plots below demonstrate that surface sampling is reliable for predicting the subsurface chemistry.

From the core log (Figure 5.17) one can see that the chemical quality corresponds relatively well with defined boundary between Unit A and B, but the chemically good quality quartzite, extends

4.2 meters downward into the red quartzite of Unit B. This is taken into consideration when modeling, e.t. Unit A in the 3D model includes the upper part of Unit B.

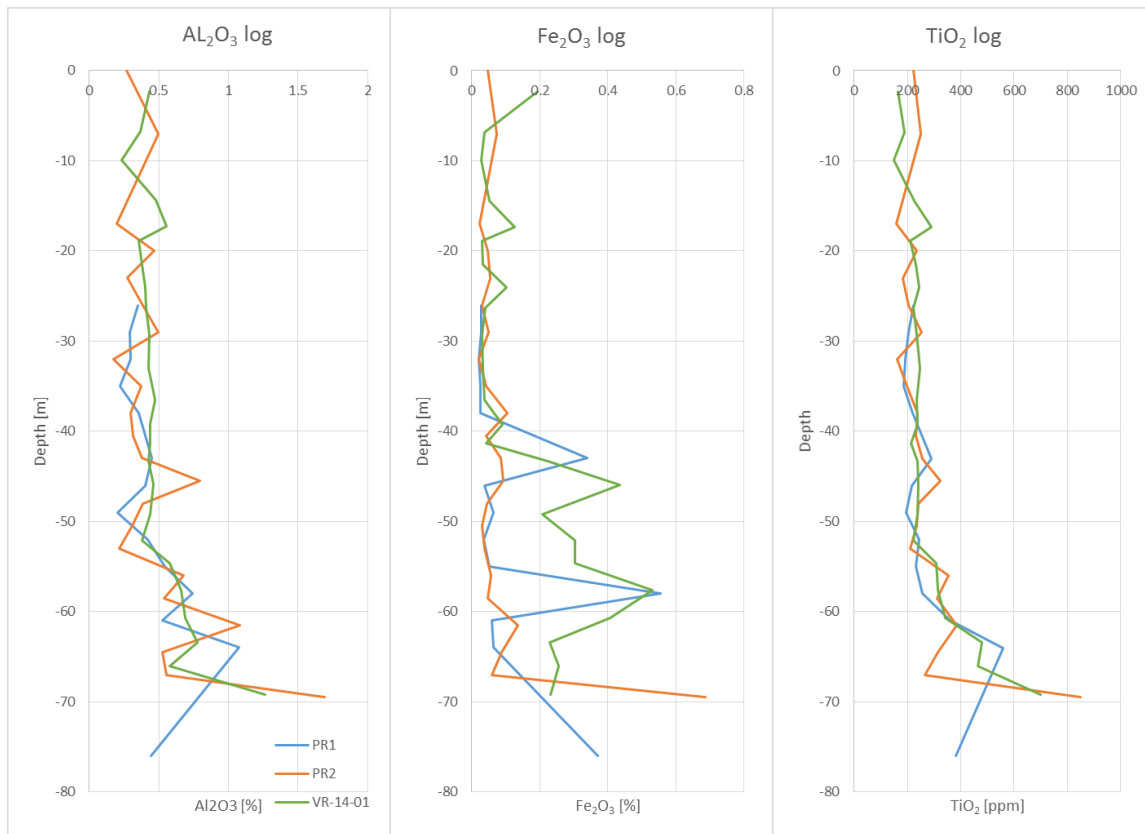


Figure 5.16: Geochemistry of profile 1, profile 2 and DDH-VR-14-01 plotted against depth, showing the same general trend between the geochemistry of the two profiles and the DDH.



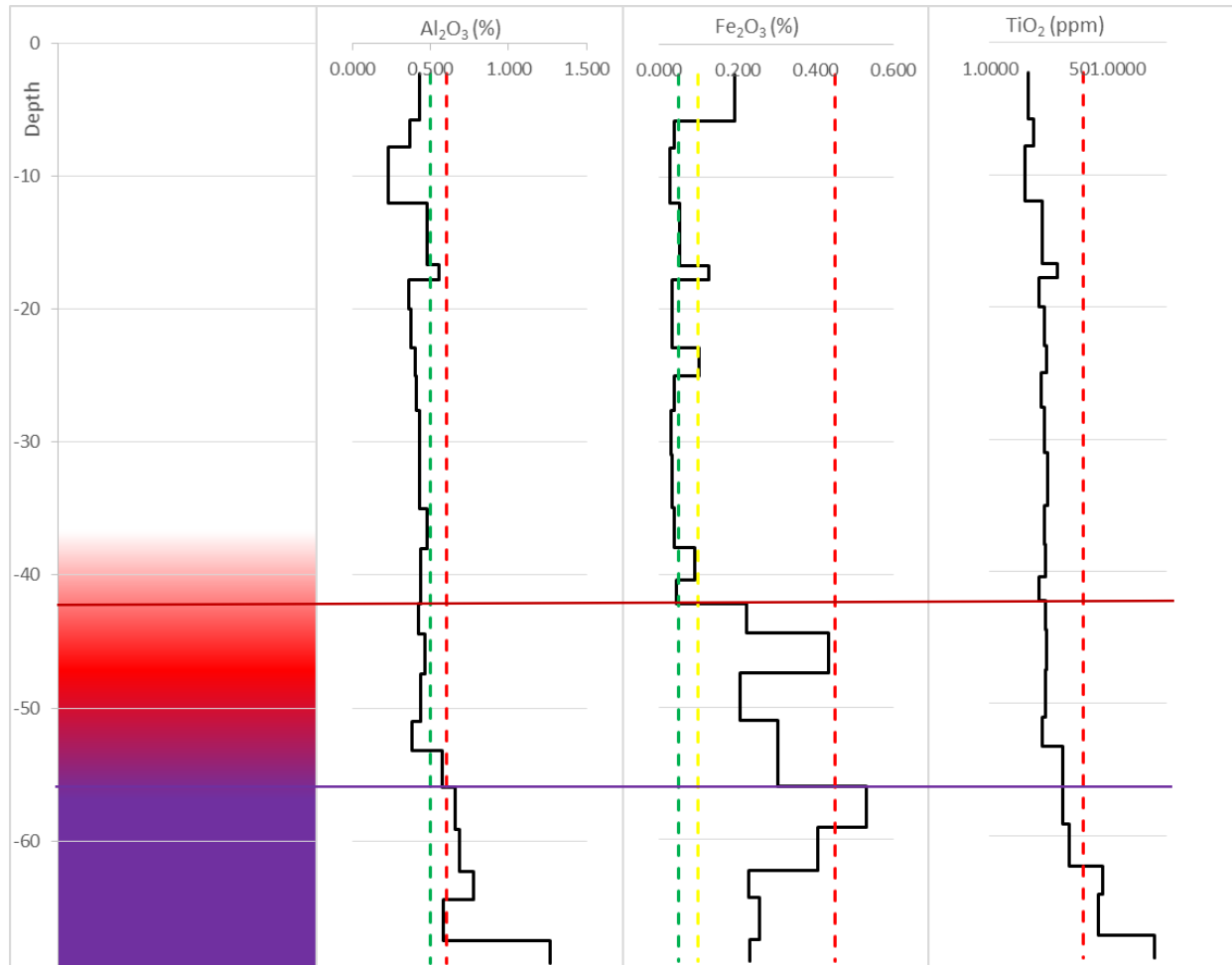


Figure 5.17: DDH log. The lithological and geochemical logs are combined. The Green and red vertical lines show the boundaries of good and bad quality respectively. The yellow vertical line is based on Elkems quality classification. The horizontal red and violet lines show the chemical boundaries used in the 3D model and resource estimation.

## 5.8 Structural Geology

### 5.8.1 *Fold classification*

A total of 186 structural measurements of the bedding were taken in the area. The locations are presented in Appendix G. At the Vaggecearru Mountain, the Gamasfjell Formation is folded into an anticline. Intersection of the folded strata with topographic relief has left older strata of the Gamasfjell Formation exposed at the summit. The younger Vagge- and Hanglecearru Formation outcrop at the flanks. The strike and dip of layers varies across the fold, but there are no signs of any minor folding within the main structure.

A strike line map is presented in Figure 5.18, the strike lines show the average strike and dip in the area, in this way simplifying the geometry of the fold. From the map it can be seen that the limbs of the fold are straight and sub-parallel, dipping SE and NW respectively. Closer to the summit the strike lines curve and dip towards the SW and NW, forming a V-shaped closure in the hinge zone. In areas of low topographic relief, such closure is typical for plunging folds, but high topographic relief affects the outcrop patterns of geological maps and the distinction between horizontal and plunging folds disappears (Weijermars, 1997). Since the strike lines of the fold limbs are sub-parallel, it indicates a slightly plunging fold (Weijermars, 1997).

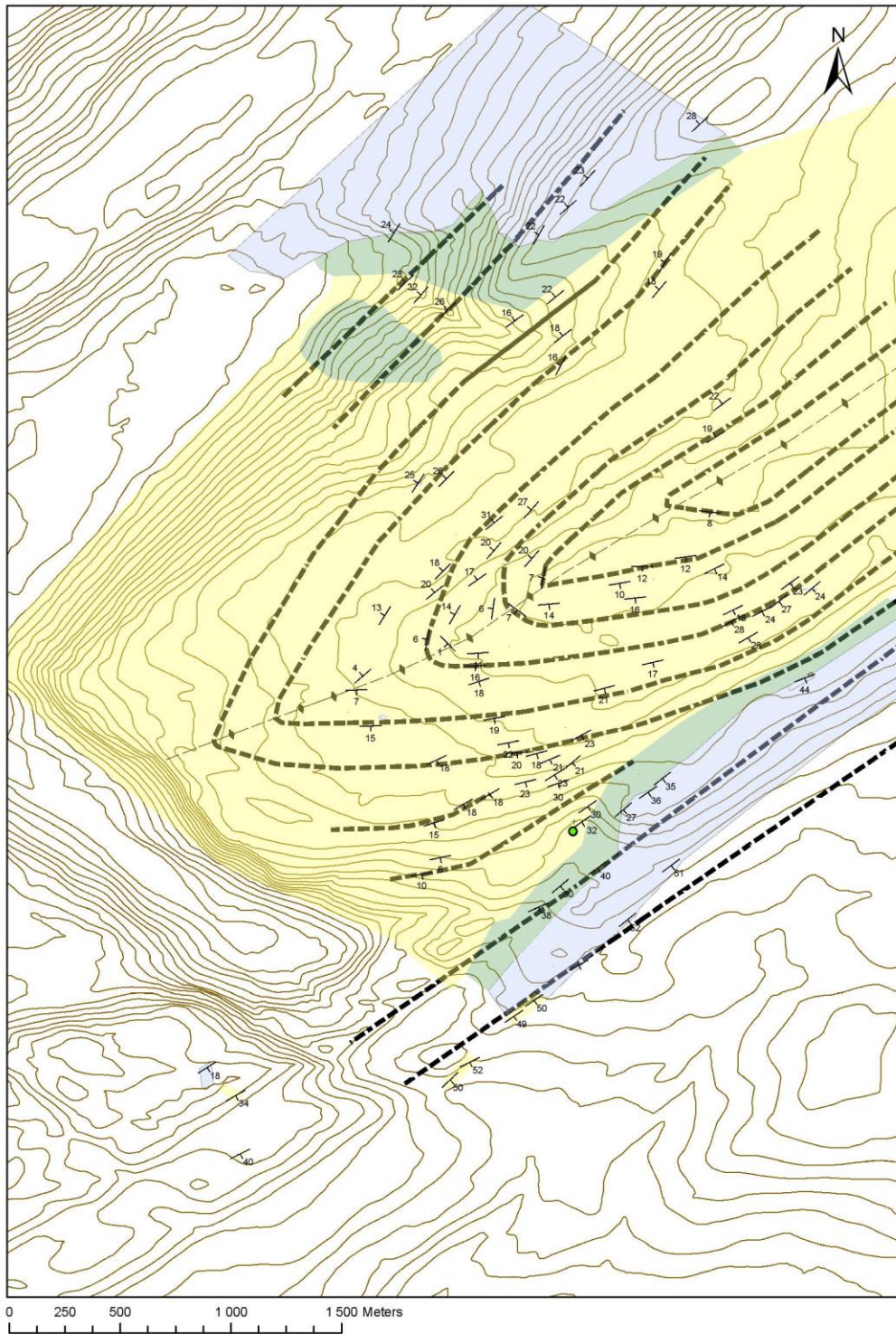


Figure 5.18: Sketch of strike lines, from the structural measurements, overlying a simplified geological map. The axial surface trace is drawn in.

In Figure 5.19a poles to the bedding are presented in a  $\pi$ -diagram. All the data points fall in very close proximity to the  $\pi$ -circle. While some points do depart from the line, more than 90% of the poles fall within an angle of 10% of the constructed  $\pi$ -circle, indicating a cylindrical fold (Ramsay and Huber, 1987).

The points are clustered in two groups close to the  $\pi$ -circle. In Figure 5.19b, contours are drawn, showing two  $\pi$ -pole maxima. These correspond to the fold limbs. The best fit planes of the limbs have a strike and dip of 066/21 SE and 222/22 NW. The orientation of the fold axis (232/04) is represented by the pole of the  $\pi$ -circle (3). The great circle crossing the acute angle of the two  $\pi$ -pole maxima shows the strike and dip of the axial plane (053/04 SE). The distance between the limbs gives an interlimb angle of 138 degrees. Based on orientation data, the fold is classified as an upright, horizontal, gentle anticline (Fleuty, 1964). The results are summarized in Table 5.3 .

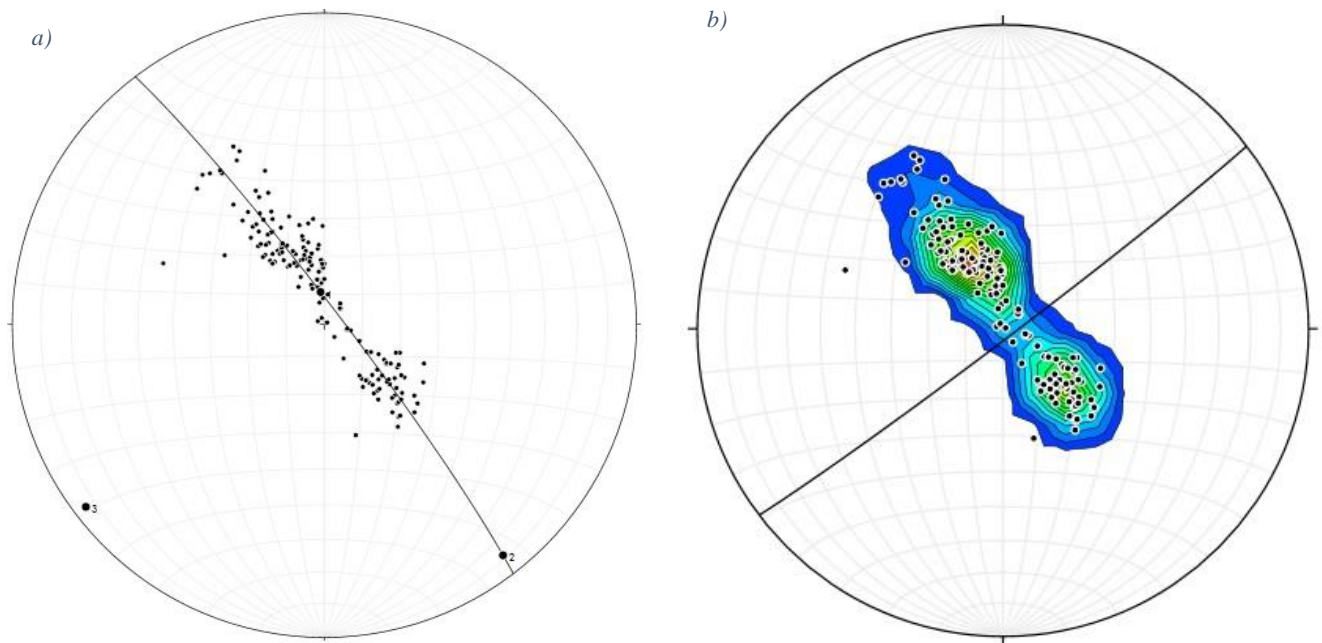


Figure 5.19: a) Measurements of bedding around the fold, including the Gamasfjell Formation., Vagge Formation. and the Hanglecearru Formation. Poles to the bedding plot along a great circle. The pole to this great circle represents the fold axis (trend/plunge). b) 1% area contours of poles.

Table 5.3: Fold classification.

	<b>Observation:</b>	<b>Classification:</b>
<i>Data point distribution</i>	Points plot close to $\pi$ -circle	Cylindrical
<i>Trend and plunge of fold axis</i>	232/04	Upright
<i>Strike and dip of axial plane</i>	053/04 SE	Horizontal
<i>Interlimb angle</i>	140	Gentle
<i>Stratigraphic relations</i>	Oldest layers in core	Anticline

### 5.8.2 Fractures

The strata of the Gamafjell Formation is affected by several joint sets. Fracture planes were measured on the SE fold limb. Joint data and bedding planes in the area are presented in Table 5.4, in the form of dip direction and dip.

Table 5.4: Azimuth and dip of main joint sets and strata within the mapped area on SE fold limb

<i>Joints:</i>
030/68, 024/64, 030/62, 027/58, 024/60, 024/57, 020/66, 026/64, 292/60, 292/72, 292/75, 295/78, 296/74, 294/76, 283/72, 274/72, 296/78, 02/70, 022/64, 335/80, 026/72, 277/67, 344/80, 294/80, 286/76, 282/90, 286/90, 289/90, 288/84, 298/87, 278/84, 307/90, 290/84, 026/88, 02/86, 020/90
<i>Strata:</i>
168/16, 166/20, 165/18, 175/20, 178/17, 155/17, 140/21, 169/22

A total of four unique joint sets were observed. They are labeled as J1, J2, J3 and J4. Figure 5.20a shows the relationship between J1-J3. Joint sets J1 (mean azimuth/dip: 025/62) and J2 (289/79) are perpendicular to each other and form an orthogonal joint system. J3 (340/80) is sub-parallel to the strike of the bedding (diagonal to J1 and J2). J4 is layer-parallel. The spacing between J1 and J2 was measured, averaging approximately 15x15m.

Large depressions extending over the mountain were also observed in the field. In the NW rock face they can be recognized as fractures, reaching down to the valley bottom. The fracture planes of these could not be measured, but from aerial images one can see that they trend in the same

orientation as J1. Because of their persistency and depth, they are differentiated from J1 and are described as master joints. The master joints have a spacing of approximately 200m.

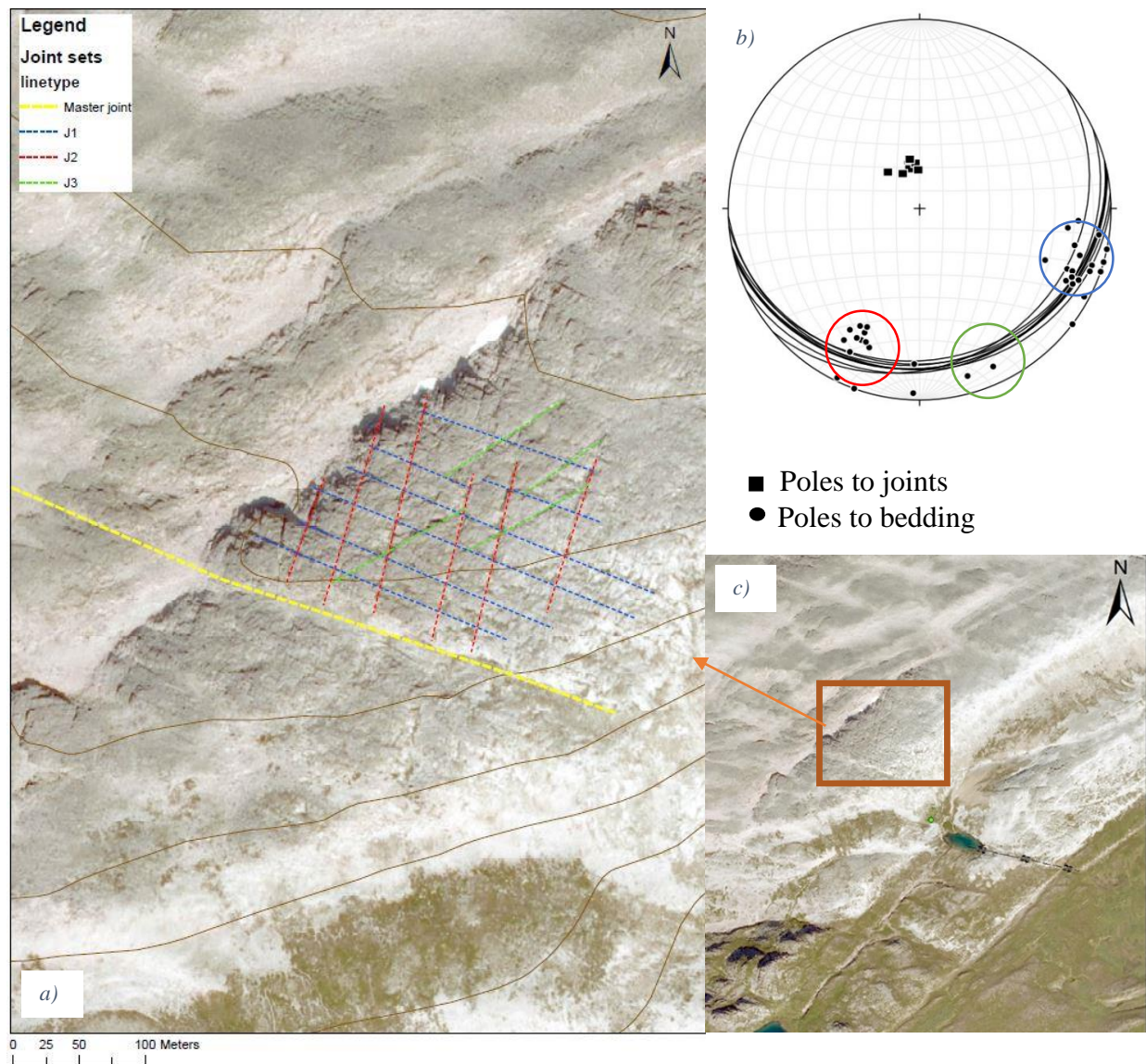
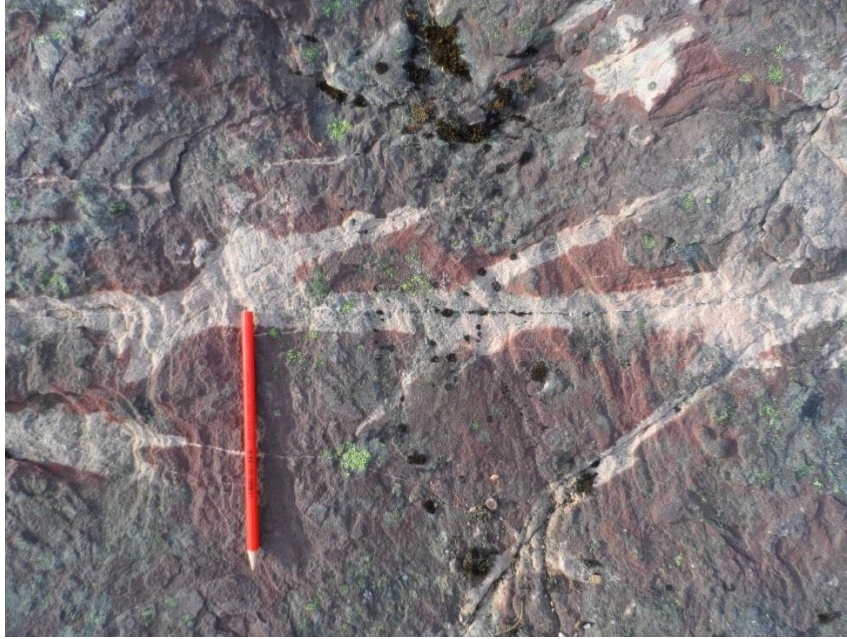


Figure 5.20: a) The main joint sets on the SE fold limb. b) Poles to the joints plot on the average bedding plane, indicating that they are perpendicular to the bedding. c) Shows the area where joints were mapped, master joints are clearly visible as light stripes.

Figure 5.20b shows an equal area projection of the poles to fractures J1-J4. The great circles represent the bedding surfaces in the area, the poles to the bedding correspond to the poles of J4. The poles to J1-J3 are distributed around the average bedding plane, showing that the joints are roughly perpendicular to the inclined bedding. The three main joint sets are encircled with the same color used to mark them in the aerial image. Note that joint sets filled with quartz (veins

and vein arrays) were also observed. These are not analyzed structurally, but an interesting observation is that veins cutting red quartzite have seemingly caused leaching (Figure 5.21).



*Figure 5.21: Color change in proximity of quartz veins, indicating leaching of hematite.*

### 5.8.3 Faults

No displacement was observed along fracture planes in the study area. However, faulting is observed beyond the study area and can be seen in areal images. In Figure 5.22, two faults are marked, which both show sinistral - strike slip displacement. Breccia was observed at the location of fault 1.

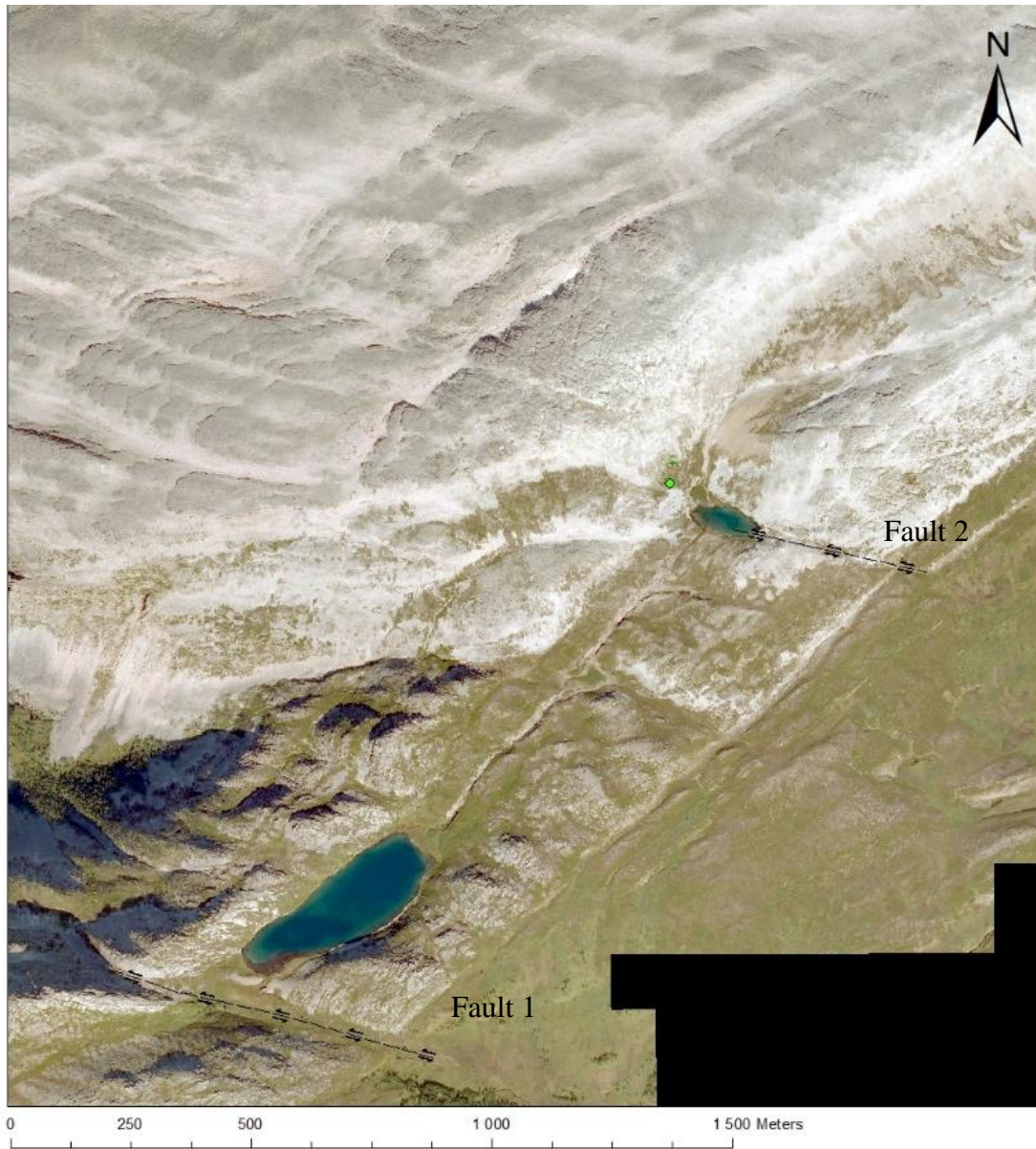


Figure 5.22: Location of two sinistral faults. Breccia observed at fault 1.



## 5.9 Weathering

Altered quartzite with low mechanical strength are characteristic in zones around the three main joint sets, extending a few centimeters to a couple of meters out from the fracture plains. In these zones, grains can easily be scraped off the surface. Fjellanger (2007), observed similar features at the nearby Hanglecearru Mountain.

In several areas, particularly in Unit B, there are open gaps, up to several meters wide (Figure 5.23a). Removal of weak, weathered material has likely resulted in these gaps, but secondary gliding or frost-wedging have probably caused further opening.

The open and weathered joints are characteristic of the fold limbs, at a depth of about 38-60m, where Unit B is exposed. Closer to the fold hinge, at a lower stratigraphic depth, as well as closer to the boundary to the Vagge shale, the joints are closed and the quartzite seems more resistant (Figure 5.23c). The transition from open weathered joints to closed unweathered joints is observed very well in the field between the boundary of Unit B and Unit C.

Much of the top of the mountain is covered by loose blocks and boulders, with unconsolidated sand between. In some areas, sand covering is very extensive (Figure 5.23b).



Figure 5.23: a) Weathering along open joint in Unit B, fracture planes have a sugary texture extending outwards. b) Image from the top of the Vaggecearru Mountain, where unconsolidated sand covers the bedrock. c) Closed joints in Unit C.

## 5.10 Petrography

60 samples were collected along profile 1, profile 2 and the DDH. All samples have been evaluated for their chemistry, 24 thin sections were made from profile 1 and profile 2. Based on the petrographic studies three quartzite types are presented below.

### *5.10.1 Unit A: Light gray quartzite*

A total of 26 samples representing Unit A were collected. 14 samples were collected along two profiles on the SE flank of the fold. Of these 12 were light gray and 2 were pink/red. 12 samples were collected from DDH, where all were light gray, but the upper sample was covered by iron hydroxides, giving a rusty secondary color. The macroscopic description and bulk chemistry is based on all 26 samples. The microscopic description is based on examination of the following seven samples; PR1-0, PR1-2,5, PR1-7,5, PR2+30, PR2+17,5, PR2+13,5, PR2+10

#### Field relations:

The light gray quartzite is representative of the uppermost part of the Gamasfjell quartzite. It is about 38 m thick and is overlain by shale of the Vagge Formation. The light gray quartzite lays above the pink-red quartzite. The boundary to the Vagge Formation appears sharp.

#### Hand-specimen:

The quartzite is light gray in color (Figure 5.24), often spotted with vugs/cavities. Areas in proximity of fractures are usually covered by rust brown iron hydroxide. The quartzite is massive and seemingly without any internal sedimentary structures. The upper part is spotted by cavities. Grains are well sorted and fine to medium in size. Cementation is extensive, but fracturing follows grain boundaries. Grains appear angular, but cement hides detrital outlines.



*Figure 5.24: A typical sample of Unit A, taken from a depth of approximately 32m below the Vagge Formation (Sample: Pr2+5).*

#### *Texture:*

Equigranular texture, dominated by medium sized monocrystalline quartz grains. Grains are well sorted and very well rounded.

All samples of Unit A are seemingly completely cemented. The cement is present as overgrowths in optical continuity with detrital grains. Contacts between mutual interfering overgrowths are mostly concavo-convex or long. In some cases the overgrowths meet at triple junctions. Some hematite is present, lining overgrowths.

Original detrital grain boundaries are in most cases difficult to observe in microscope, but in some cases dust like rims mark the original grain outline. Crystal strain is low, with quartz grains showing mostly uniform or slightly undulus extinction. Very few minerals other than quartz were observed. Some clay is present, in small local patches and dispersed between grains. Trace amounts of heavy minerals are also dispersed throughout.

*Mineralogy:**Detrital:*

- a) Quartz: Quartz is present as monocrystalline grains and as secondary overgrowths. Quartz grains are very well rounded, but can be difficult to see because of overgrowth cement.
- b) Heavy minerals observed were rutile and zircon. In microscope, zircon was identified by its high relief and high order interference colors. Both rounded and angular varieties are present. Rutile is present as acicular needles and blades, often as inclusions in quartz grains. Heavy minerals confirmed by microprobe.

*Chemical constituents:*

- a) Hematite: Only a small amount of hematite is present in Unit A, as coatings around quartz cement. Identified by XRD
- b) Authigenic quartz: Present as secondary overgrowths around detrital grains. Quartz overgrowth is in optical continuity with detrital grains.
- c) Authigenic clay: Sericite and pyrophyllite are present in trace amounts, usually concentrated in small patches. Sericite normally occupies grain shaped/sized pores, while pyrophyllite is more dispersed. Sericite and pyrophyllite were confirmed by microprobe.

*Bulk chemistry:*

26 samples of Unit A were analyzed. Table 5.5 presents the average weight percent and ppm of the main contaminating oxides. The average for surface and sub-surface samples are presented separately for comparison.

*Table 5.5: Average major element composition of Unit A.*

Oxides	Average content (Surface)	Average content (Sub-Surface)	Range (Surface)	Range (Sub-Surface)
Al <sub>2</sub> O <sub>3</sub> (%)	0,330	0,4104	0,17-0,49	0,23-0,55
Fe <sub>2</sub> O <sub>3</sub> (%)	0,037	0,0618	0,02-0,07	0,03-0,19
TiO <sub>2</sub> [ppm]	207	221	158-255	150-290
P <sub>2</sub> O <sub>5</sub> [ppm]	59,45	47,90	29,7-97,6	37,0-63,8

### 5.10.2 Unit B: Pink and red quartzite

A total of 18 samples were collected of Unit B, where 12 were from surface sampling and 6 from the DDH core. All samples were pink to red in color. The macroscopic description and bulk chemistry is based on all 18 samples. The microscopic description is based on examination of the following nine samples; PR1-17,5, PR1-20, PR1-22,5, PR1-25, PR1-27,5, PR2-0, PR2-2,5, PR2-5, PR2-15.

#### *Field relations:*

The boundary was defined in the field and in the drill core. Stratigraphically, Unit B is approximately 38 meters below the Vagge Formation.

#### *Hand specimen:*

Generally massive, alternates in color, between mostly pink and red (Figure 5.25). Internal sedimentary structures are visible in some cases, but the red color does not usually define sedimentary structures, but rather has a smeared out appearance. Cementation appears to be relatively extensive.



Figure 5.25: Typical sample of Unit B, Collected at a depth of approximately 46m below the Vagge Formation (Sample: Pr2-7,5).

*Texture:*

In general has a bimodal distribution of fine- and medium-grained quartz. The majority of quartz grains are monocrystalline. Cementation is extensive. Detrital grains are often coated by fine material, revealing well rounded original grains. Grain contacts are concavo-convex and sometimes sutured. Sutured contacts are more typical for fine grains in contact with clay. Most quartz grains are low to moderately undulous in extinction. Some sericite and pyrophyllite is present in small patches, the latter seemingly replaces quartz cement. The amount of hematite varies between samples. Hematite lining quartz overgrowths is normal. Hematite is also often present in patches together with clay minerals.

*Mineralogy:**Detrital:*

- a) Quartz is the dominate mineral, most are monocrystalline, but some polycrystalline grains are also present. Secondary overgrowths present on most grains.
- b) Heavy minerals are dominantly zircon, tourmaline and rutile. Monazite is also present, identified by microprobe. Heavy minerals confirmed by microprobe.

*Chemical constitutes:*

- a) Hematite: Hematite is present as thin films coating grain overgrowths. Often the hematite is concentrated on one side of grains, as small globs. identified by XRD..
- b) Authigenic quartz: Present as secondary overgrowths around detrital grains. Quartz overgrowth is in optical continuity with detrital grains.
- c) Authigenic clay: Sericite is present in small to trace amounts, usually concentrated in local patches. Pyrophyllite is the dominant clay mineral, but is also present in small amounts. Recognized indirectly in microscope by the disintegrating effect it has on quartz cement. Clays were confirmed by microprobe.

*Chemistry:*

18 samples of Unit B were analyzed by ICP-IOS. Table 5.6 presents the average weight percent and ppm of the main contaminating oxides. Surface and sub-surface samples are separated when calculating the average, so that they can be compared.

*Table 5.6: Average major element composition of Unit B.*

Oxide	Average content (Surface)	Average content (Sub-Surface)	Range (Surface)	Range (Sub-Surface)
Al <sub>2</sub> O <sub>3</sub> (%)	0,3918	0,4508	0,20-0,80	0,38-0,58
Fe <sub>2</sub> O <sub>3</sub> (%)	0,0802	0,2295	0,04-0,11	0,04-0,43
TiO <sub>2</sub> [ppm]	243	243	197-324	213-310
P <sub>2</sub> O <sub>5</sub> [ppm]	43,1	36,7	31,8-57,5	25,2-64,9



### 5.10.3 Unit C: Pink/red/violet quartzite

A total of 15 samples were collected of Unit C, where 10 were from exposures at the surface and 5 came from the DDH core. Samples vary in color. The macroscopic description and bulk chemistry is based on all 15 samples. The microscopic description is based on examination of the following eight samples; PR1-30, PR1-32,5 PR1-45, PR2-17, PR2-19,5, PR2-22, PR2-25, PR2-30,

#### *Field relations:*

Unit C is the lowest unit defined and represents uneconomical quartzite/the footwall. The boundary lays approximately 55-60 meters below the Vagge Formation.

#### *Hand specimen:*

The quartzite shows variation in color, alternating between pink, red, dark red, brownish red and violet (Figure 5.26). Primary sedimentary structures are well preserved. Sedimentary structures include crossbedding, both unidirectional and bimodal. Crossbedding consists of alternating layers of fined grained and medium to coarse-grained quartz (sometimes very coarse grains). The fine grained layers are stained darker red to violet by iron oxide. The quartzite is seemingly very resistant.



Figure 5.26: Typical sample of Unit B, Collected at a depth of approximately 70m below the Vagge Formation ((Sample: Pr2-30).

*Texture:*

Bimodal distribution, with alternating layers of fine grained and coarse grained quartz. Cementation is extensive. Monocrystalline grains dominate, but there is also a relatively large amount of polycrystalline. Strain in crystals varies, but most are non- or slightly undulatory, some crystals exhibit sweeping extinction. Grain boundaries are often sutured, particularly in the fine grained fraction. A relatively large amount of hematite is present. The highest concentration is in fine-grained layers. Clay minerals such as sericite and pyrophyllite are common, concentrated in patches, between grain boundaries and in layers. Small dust rims are present on detrital rims of some grains.

*Mineralogy:**Detrital:*

- a) Quartz is the dominant mineral, present are both monocrystalline and polycrystalline varieties. Polycrystalline quartz is more common than in above lying units.
- b) Heavy minerals are dominantly zircon, tourmaline and rutile. Monazite is also present in lesser amounts. Heavy minerals are most abundant in the fine grained quartz layers. Zircon is present as both rounded and angular varieties. Rutile is present as acicular needles and blades. Small tourmaline grains are also present. All heavy minerals were confirmed by microprobe analysis.

*Chemical constituents:*

- a) Hematite: Samples are peppered by hematite. Highest concentration in fine grained layers. Identified by XRD.
- b) Authigenic quartz: Present as secondary overgrowths around detrital grains. Quartz overgrowth is in optical continuity with detrital grains.
- c) Authigenic clay: Sericite is present in small amounts, usually concentrated in grain sized patches. Pyrophyllite is the dominating clay mineral and is present in relatively large amounts. Typically occurs in patches filling pore voids and in fine-grained layers, mixed with quartz and hematite. Quartz boundaries surrounding pyrophyllite are usually sutured. Confirmed by microprobe.

*Chemistry:*

15 samples of Unit C were analyzed by ICP-IOS, giving the bulk chemistry. Table 5.7 presents the average weight percent and ppm of the main contaminating oxides. The average for surface and sub-surface samples are presented separately for comparison.

*Table 5.7: Average major element composition of Unit C.*

Oxide	Average content (Surface)	Average content (Sub-Surface)	Range (Surface)	Range (Sub-Surface)
Al <sub>2</sub> O <sub>3</sub> (%)	0,7626	0,7928	0,44-1,69	0,58-1,26
Fe <sub>2</sub> O <sub>3</sub> (%)	0,1975	0,3306	0,05-0,69	0,23-0,53
TiO <sub>2</sub> [ppm]	388	461	231-850	314-701
P <sub>2</sub> O <sub>5</sub> [ppm]	74,39	61,82	18,95-218,9	27,44-98,57

## 5.11 3D model

A 3D model of the study area has been created in Leapfrog. The model includes the most persistent joints (master joints) as well as the Hanglecearru Formation, the Vagge formation and the Gamasfjell Formation (divided into Unit A, Unit B and Unit C). The boundaries between the units in the 3D model, have been updated to correspond to the qualities; good, intermediate and bad (Table 2.2). The only change made was that the boundary between Unit A and Unit B was moved from 38m (Figure 5.27) to 42,2m (Figure 5.28) in the subsurface (The cross sections are on the same profile as A-B in Figure 1.1.) Figure 5.17 shows the log that this decision is based on. The outcropping horizons have not been changed.

### 5.11.1 Assumptions and constraints

This chapter presents the assumptions made during modeling and the constraints of the 3D model.

#### *Chemistry*

- Unit B is more iron rich in the subsurface, then on the surface. The subsurface samples (DDH – samples) will represent Unit B.
- In the subsurface, the good quality quartzite associated with Unit A, extends 4,2 meters below where the boundary to Unit B is visually defined. That is, the upper part of the red colored quartzite is low in iron and aluminum. The boundary has been moved accordingly.
- Unit A includes two sub-horizon totaling 3.2m thickness (Figure 5.15). These sub-horizons are red in color, more rich in iron and therefore more similar to Unit B. These two horizons will however not be separated from Unit A.
- In the drill core the top 3.5m of Unit A is covered by iron hydroxides, giving it a rusty color and causing an increased iron content. The top 3,5m will however be modeled as Unit A.

#### *Structural*

- A total of 186 structural measurements were taken over the fold. It is not practical to use all of them when generating a 3D model, therefore geometric facts were accumulated from the measurements, giving the average strike and dip of layers.

- The fold is assumed to be a 1B type fold, e.t. having equal layer thickness. When constructing the fold in leapfrog, isogons were therefor drawn normal to the structural measurements on the surface and extended downward in order to create subsurface layers.
- To get a geologically reasonable model, horizons were adjusted manually based on geological analysis.
- Master joints are included in the model. They are traced on the basis of aerial images, and are assumed to have the same azimuth and dip as J1 (025/62). Eventual uneconomic quartzite associated with joints, is not taken into consideration.
- Boundaries are inferred for the NW limb and are not as accurate as on the SE limb.

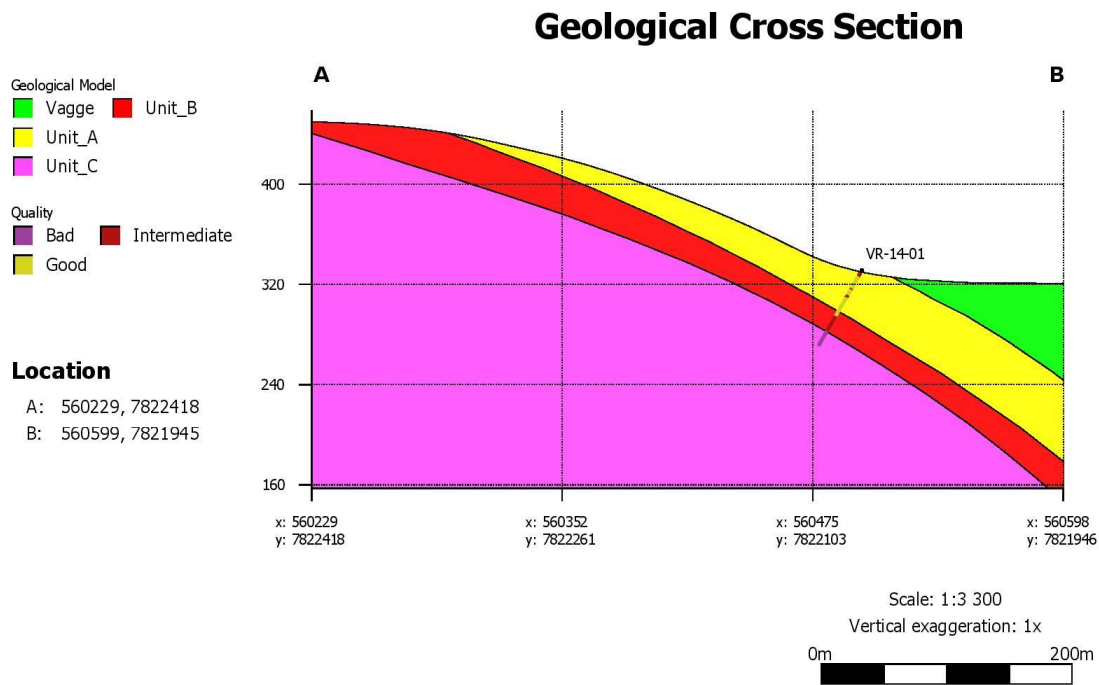


Figure 5.27: Cross section of the fold (053/90). Made by taking a vertical slice through the 3D model in leapfrog. The DDH is included, showing quality. As can be seen, the good quality extends downward into Unit B.

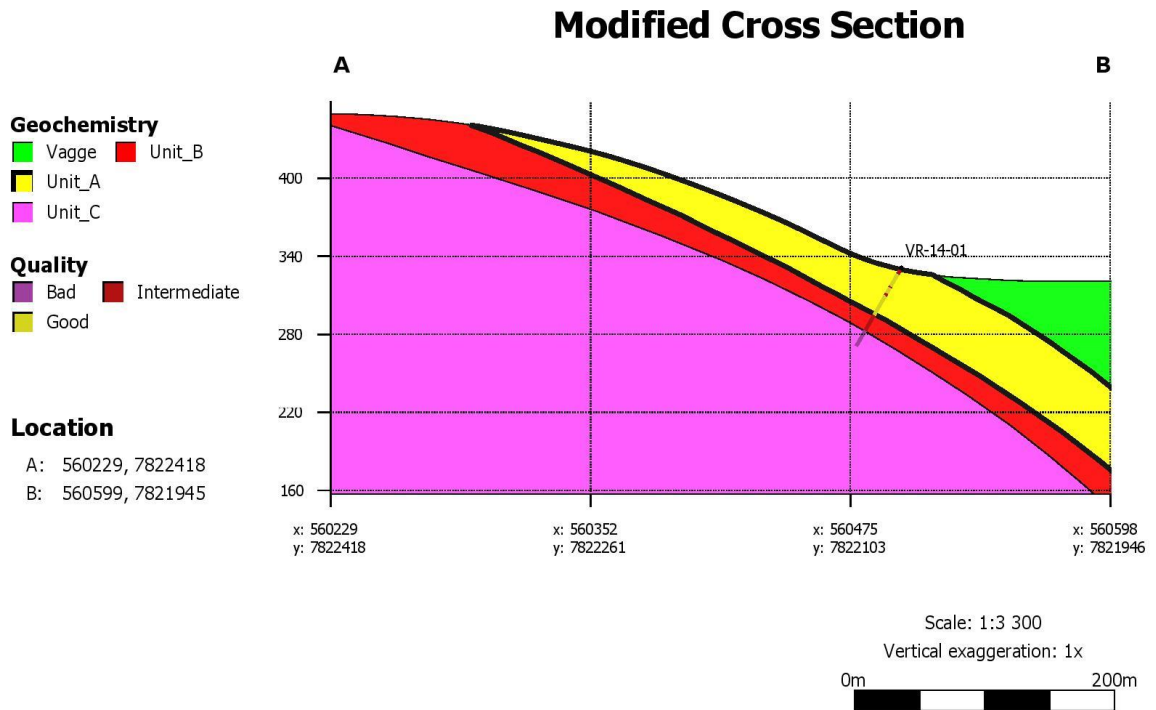


Figure 5.28: Cross section of the fold (053/90), same as figure 5.25, but Unit A has been made thicker in order to include the good quality in the pink/red quartzite.

### 5.11.2 Presentation of model

Figure 5.29 - Figure 5.32 presents images of the model, from different views. This thesis includes an attachment of the 3D model (requires Leapfrog Viewer), where the model can be examined in more detail.

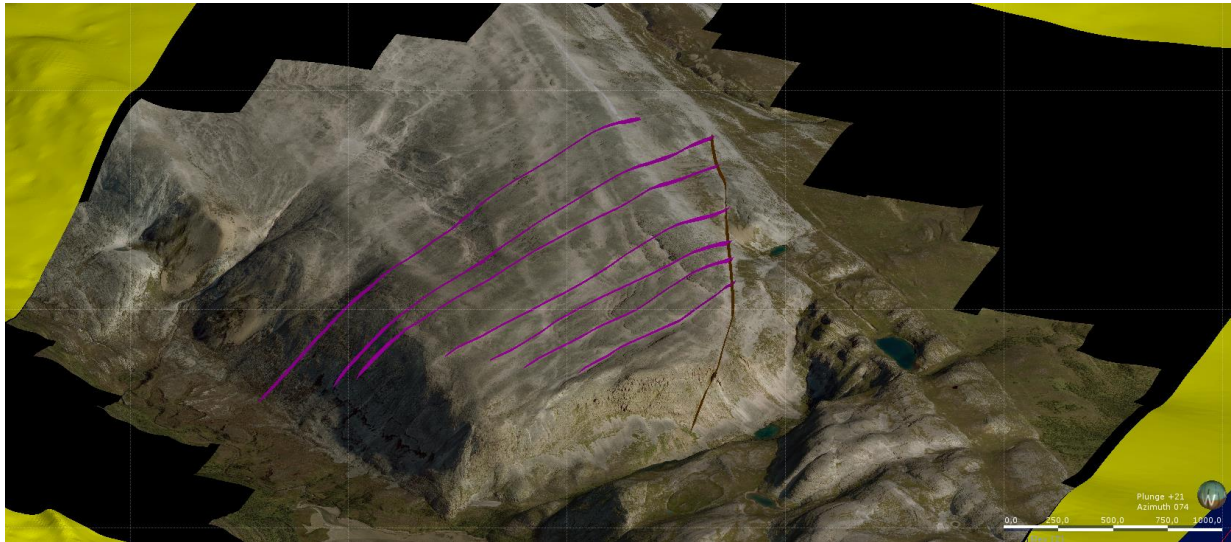


Figure 5.29: Eastern view of the Vaggecearru Mountain. Aerial images are draped over the topography. Master joints are drawn in, crossing the Mountain.

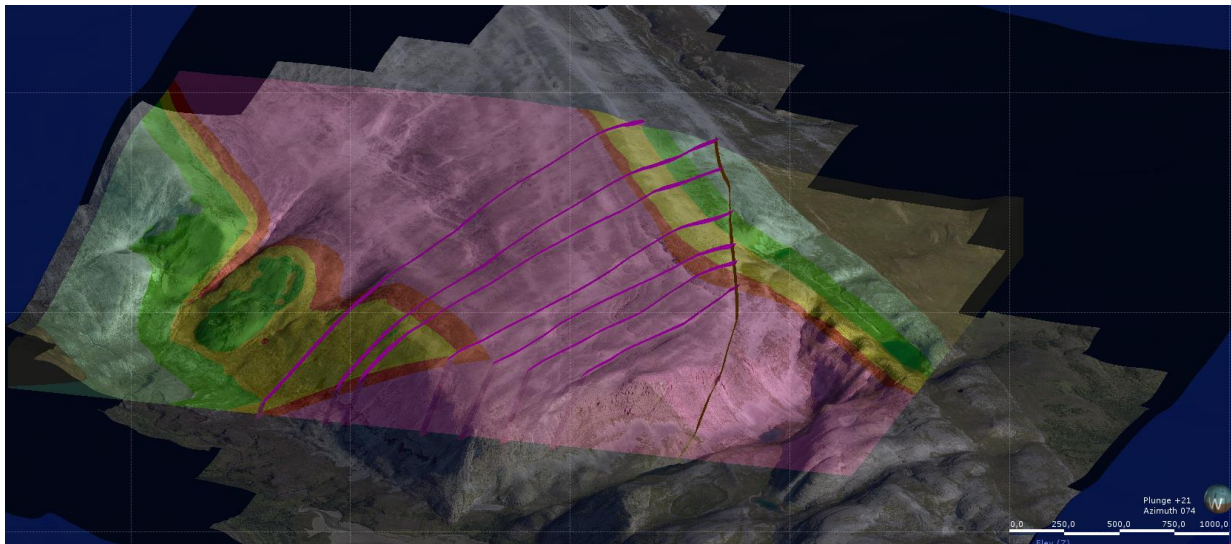


Figure 5.30: Same view as above, but with transparent topography. The different formations and units become visible.

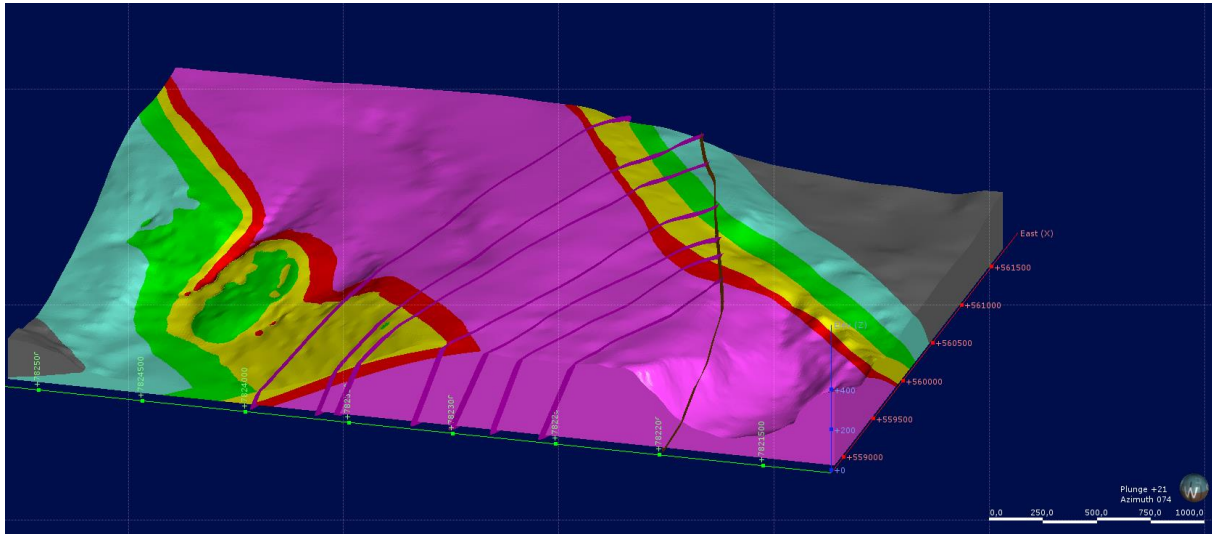


Figure 5.31: Same view as in the figures two above. Here the aerial images are removed, making the formations and units clearly visible.

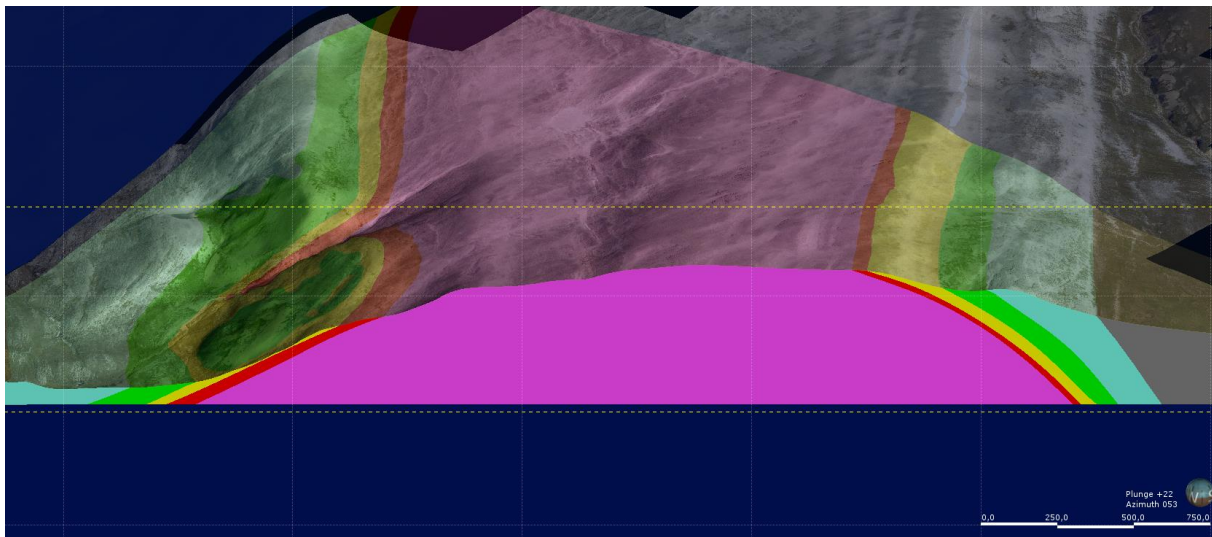


Figure 5.32: NE view. Cross section (053/90). The geometry of the fold is revealed.



### 5.11.3 Resource estimation

The volume and tonnage of the deposit have been estimated within the defined boundary (Table 5.8), shown in Figure 5.33. The tonnage is calculated, assuming a quartzite density of 2600 kg/m<sup>3</sup>. The boundary encompasses profile 1, profile 2 and the DDH. The estimation is based on the geological model, with the assumptions and constraints described in chapter 5.11.1. Table 5.9 presents the results.

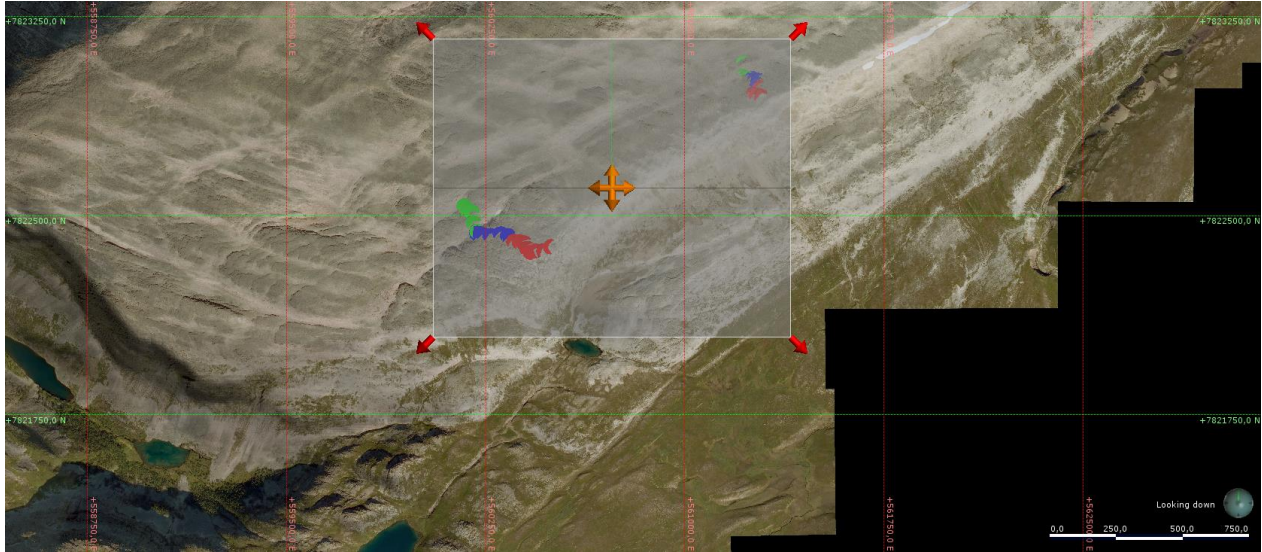


Figure 5.33: Boundary of resource estimation, limited by profile 1 and profile 2 and the DDH VR-14-01.

Table 5.8: Boundary of resource estimation

X (East):	Min: 560051.9077517288	Max: 561398.1951496056
Y (North):	Min: 7822042.495095255	Max: 7823164.551765226
Z (Elev):	Min: 270.0	Max: 530

Table 5.9: Results of resource estimation (rounded to nearest 100 000)

Quality	Volume (m <sup>3</sup> )	Tonnage ((D*V)/1000)
Unit A (Good)	17 200 000	44 720 000
Unit B (Intermediate)	11 700 000	30 160 000

## 6 Discussion

This chapter will first discuss the relationship between visual features and chemical properties, with a focus on the differences between Unit B and Unit C, as this boundary has generally been difficult for Elkem to define visually. A short discussion of the diagenetic history will be presented, focusing on how clay minerals, rutile and hematite formed. Structural geology will also be discussed, focusing on how the deposit is affected by jointing and weathering.

### 6.1 Geochemistry and appearance

Once the different units had been defined by visual characteristics in the field, part of the goal was to see if these characteristics were linked to unique chemical properties. This would be helpful for future mapping and planning, as one could use visual characteristics as an indicator of the quality of the resource.

There is a relatively good correlation between the geochemistry of the samples and visual characteristics, e.t each visually defined unit can be linked to a chemical signature. The only divergence is that some samples of Unit B (e.g. the upper part of Unit B in the DDH) are chemically, more like Unit A. This chapter will discuss all the relationships that were found between visual characteristics and geochemistry.

Firstly, the color of the three units give a visual clue to the amount of iron oxide that is present. Typically when iron oxide content is above 0.05%, the rock will show a pink to red color. However, the amount of iron oxide does not necessarily correspond with the intensity of the red color. Typically, the color intensity of red beds is more controlled by the grain size of the hematite than the amount, with fine grains typically causing more intense colors (Mücke, 1994). This is seen in the Gamasfjell Formation. In alternating sedimentary beds and lamina of coarse and fine grains, the fine grained fraction typically show a more intense color. Other minerals contributing with iron are also present, such as iron hydroxide, which leads to locally high iron oxide measurements (e.g. upper 3,5m in Figure 5.17).

Color was used to divide Unit A and Unit B, which chemically represent good and intermediate quality. While the boundary between good and intermediate quality is easy to observe and has generally not been a problem for Elkem. The boundary separating intermediate quality and the

footwall has been difficult for Elkem to define visually. The following discussion will therefore focus on the defining characteristics of the footwall, termed Unit C in this report.

Primarily it is the increase of aluminum that leads to bad quality. The problem is that aluminum does not give any defining color to the rock. However certain characteristics were observed in the field that were associated with a higher aluminum content.

Small scale sedimentary structures were the first thing that was noticed in the field at a stratigraphic depth of about 50m below the Vagge shale and was the main criteria used when defining the boundary between Unit B and Unit C. When the geochemical results returned, they showed that this was also the chemical boundary between the intermediate quality and the footwall.

In the drill core these structures were not observable. This may be due to the drill core having a small diameter, and because it was not cut lengthwise before logging. With a larger diameter and/or by cleanly cutting the core before logging, the sedimentary structures observed at the surface may also become visible in the core.

Another important visual characteristic of the footwall is that it is seemingly more resistant to weathering, then the above lying Unit B. This is seen particularly well near fractures. When passing the boundary between Unit B and Unit C, at the SE limb it is very visible. The fractures go from open to closed. The altered texture typically extending out from the fracture planes above are not present in unit C. Sauro, (2014), examined sandstones in Venezuela and found aluminum-silicate rich sandstones were more resilient than pure quartz sandstones. He attributed this to the fact that the aluminum-silicate rich sandstones had less porosity, because of clay minerals.

The quartz in the Gamafjell Formation seems to be completely cemented and interlocking when studied in microscope, if however thin sections are prepared with florescent epoxy, it is seen that certain samples have more porosity between quartz boundaries then others (Johannesen, 1998). This may explain why the footwall is more resilient. It most likely has less porosity and permeability, due to clay minerals blocking the passageway that the water travels through in the above lying unit. Note that the upper part of the Gamafjell Formation (Unit A) is also less affected by weathering, this may be because of its more quartzitic texture.

Microscopically, there are also some unique features that are typical for the footwall. Firstly, the macroscopic features, such as sedimentary structures are also seen in microscope and can be studied in more detail. The sedimentary bands are finer grained, clay is more abundant in these bands, so is hematite and heavy minerals. According to (Edward, 1968), this type of lamination is typical in beach zones. He found that fine and/or heavy mineral rich layers are concentrated at the base and grade upwards into coarser and heavy mineral poor layers.

The clay minerals increase with depth and are diagenetic in origin. The precursor mineral was most likely feldspar, this is supported by grain shaped/sized pores (Figure 5.7). If more feldspar survived in the depositional zone of Unit C compared to Unit A and B, it explains why there is more clay present. The survival of feldspar may indicate less recycling of these sediments.

Polycrystalline grains also increase with depth. This may also indicate less recycling, making the survival of polycrystalline grains possible. It can also indicate that the source may have changed during deposition. As polycrystalline grains are not dominating, they are interpreted as protholiths, e.t they were deposited, and not a result of later deformation and sub grain boundary formation.

The amount of  $\text{TiO}_2$  increases nearly linearly with stratigraphic depth and is strongly related to the  $\text{Al}_2\text{O}_3$  content. The relationship between  $\text{TiO}_2$  and depth is shown in Figure 5.16. As can be seen,  $\text{TiO}_2$  steadily increases with depth, reaching around 350-400 ppm at the footwall and is very strongly correlated to  $\text{Al}_2\text{O}_3$  with an  $R^2$  of 0,8384 (Figure 5.13). Another interesting observation is that the amount of  $\text{TiO}_2$  in surface samples and core samples do not differentiate very much. The only mineral observed containing  $\text{TiO}_2$  is rutile. However, it is possible that titanium is substituted in the clay minerals (Dolcater et al., 1970). The increase in rutile with depth can be an effect of less recycling or that the source rock changed. Another, possibility, considering the strong relation between  $\text{Al}_2\text{O}_3$  and  $\text{TiO}_2$ , is that much of the rutile is diagenetic in origin, and could be the mineral Anatase. Anatase is a polymorph of rutile that may contain minor amounts of Fe and Sn. It is a relatively common mineral in sediments, where it is often autigenic in origin (Deer et al., 1992). Thus, anatase may have precipitated from a titanium rich solution, and then have become embedded in, or between quartz and clay minerals (Morad and Aldahan, 1987).

Either way,  $\text{TiO}_2$  could be a good supplement for indicating the quality of the quartzite. Other oxides such as  $\text{K}_2\text{O}$  and  $\text{Na}_2\text{O}$ , which are expected to be correlated to  $\text{Al}_2\text{O}_3$  as they typically constitute clay minerals, show a weaker correlation.

Thus, it seems that both the mineralogical and textural maturity of the Gamasfjell formation increases upwards. It is not uncommon that sands in a sedimentary sequence show such a trend (Pettijohn et al., 1987). A progressive decrease in feldspar and rock particles with decreasing age can indicate multicycling (Pettijohn et al., 1987), for example, cycles of transgression and regression may have caused reworking of the sediments, making the last sediments deposited most mature.

## 6.2 Diagenesis

The Gamasfjell Formation formed as a result of intense chemical weathering of the Proterozoic surface. The sand was deposited in a shallow marine environment (Johnson et al., 1978), where the back and forth movement of the tide cleaned and rounded the sand.

During burial, quartz precipitated as overgrowths completely filling intergranular pore spaces. The presence of concavo-convex and sutured boundaries could indicate that the source of silica came from pressure solution at grain contacts, but other sources are also possible (McBride, 1989 and references therein). Although feldspar was not observed in this study, the Gamasfjell quartzite is described to contain some (Siedlecka, 1990). Most of the original detrital feldspar grains were likely dissolved during diagenesis. Wilkinson et al., (2001), found that dissolution of feldspar takes place at temperatures between 60 and 160 °C, during deep burial (1,5-4,5 km). Feldspars grains were likely replaced by sericite and probably also kaolinite. However, kaolinite was not observed in the Gamasfjell Formation. The more rare mineral pyrophyllite (Deer et al., 1992) was detected. The presence of pyrophyllite indicates temperatures of at least 300 °C., but no more than 420 °C (Deer et al., 1992). This is a region between late diagenesis and early metamorphism (Worden and Burley, 2003). During burial, kaolinite probably reacted with quartz cement and formed pyrophyllite (Dyar et al., 2008). This is also what Fjellanger, (2007) thought to be the cause of pyrophyllite in the Hanglecearru Formation. The kaolinite may have contained titanium. The dissolution of kaolinite may then have led to titanium rich fluids that allowed for the precipitation of anatase (Morad and Aldahan, 1987).

The red color of the lower part of the Gamafjell formation is due to hematite (Figure 5.10), while more recent weathering and hydration oxygenation has caused the rust color associated with iron hydroxide.

Red quartz arenites are mostly associated with aeolian environments, while gray quartz arenites are associated with marine environments. Red beds may however form in marine environments close to land (Mücke, 1994 and references therein). The Gamafjell is interpreted as marine in origin (Johnson et al., 1978), the origin of the red color will be briefly discussed below.

There are several explanations for the origin of hematite. Mücke, 1994 summarizes the leading hypothesis as; 1) Iron hydroxide coating sand grains were dehydrated with during or shortly after deposition and converted to hematite. 2) Dissolution of Fe-bearing detrital minerals and precipitation of hematite during diagenesis. 3) Postdiagenetic replacement of iron hydroxides by hematite.

Observations done in this thesis point mostly with the first two hypothesis 1) Thin films of hematite coat detrital grains (Figure 5.8) 2) Smear out red layers (not following sedimentary layers) (Figure 5.3f) and cavities (Figure 5.3e). The leached red quartzite surrounding what is most likely syntectonic quartz veins (Figure 5.21), suggests that the hematite was not of postdiagenetic origin, e.t formed after uplift.

### 6.3 Structural geology:

The Gamafjell Formation is folded by an upright, sub horizontal, gentle fold. The folding of the Formation has not caused any significant deformation, evident by e.g, preserved primary bedding and unstrained quartz.

The fractures were most likely created during uplift and denudation, as the poles to the fractures plot along the average bedding plane (Ramsay and Huber, 1987). In areas bordering the fractures, the quartzite is often altered. Fjellanger, (2007) studied the nearby quartzite at the Hanglecearru Mountain and explained the altered quartzite as a result of teleogenesis, where water flushing through the joints over long periods of time weakened the mechanical strength of the quartzite.

Johansen, 1998 mapped the Gamasfjell Formation at Tananeset, and differentiated between quartzite and quartzitic sandstone. Johansen concludes that the quartzitic sandstone are layers that during burial were less cemented.

From observations done during the present field study, altered quartzite seems to be related to fractures, however the highest concentration of altered zones is located around joints in Unit B. Unit B may be more in resemblance of a sandstone and less resilient towards weathering. The joints seem less affected by alteration closer to the flanks of the fold, as well as lower down in the stratigraphy. The uppermost stratigraphy (Unit A) has a more quartzitic texture (interlocking grains, triple junctions etc.), while Unit C, contains a higher abundance of clay, both of these facts may have prohibited water circulation. Unit B, having neither a high amount of clay, nor a quartzitic texture may therefore have been most effected by chemical weathering.

The quartzitic texture of Unit A, may not be related to a higher strain, but rather a result of the absence of clay minerals, making grain boundary growth more extensive. Structurally, folds often experience outer arc extension and inner arc contraction, which would mean that Unit A experienced the least amount of strain. Outer arc extension also explains the jointing. Stored elastic strain was probably released during uplift, causing development of joints (especially in the hinge zone), extending down to the zone of contraction.

Unit A has been completely eroded at the hinge zone. The layers in the hinge zone have a low dip, and the joints are normal to the bedding surface, which could have made chemical weathering more effective as water could be stored for longer periods, compared to the more steeply dipping limbs.

Thus, Unit B, likely has the most porosity and permeability. The limbs of the fold were probably less effected by chemical weathering, as the layers are more steeply dipping. Unit C may be more resilient as a result of being closer to the zone of contraction.

The association of joints with altered quartzite may reduce the volume of the resource.

Particularly the master joints, which cross the whole mountain and are observed reaching all the way down to the valley bottom along the NNW rock face. When planning a drilling campaign the master joints should be avoided, as the drill crown can become stuck in these zones. J1-J3 are probably not as problematic for drilling, but may reduce the volume of the resource somewhat.

However, no altered quartzite was observed in drill-core VR-14-01. This may indicate that the altered zones surrounding J1-J3 do not penetrate very deep.

In several areas, fracturing and weathering has caused the quartzite to break into blocks. Because the area was covered by cold based glaciers, which are not the type of glaciers that erode underlying bedrock, the blocks are interpreted to lay in situ (Fjellanger et al., 2006). It would therefore be interesting to set a profile across the blocks for comparison with DDH cores and other profiles.

#### 6.4 Assumptions, constraints and inaccuracies in model

This chapter discusses some of the chemical and structural assumptions and constraints used when generating the 3D model and resource estimation. Inaccuracies in the model are also listed.

Chemistry:

- Unit B is more iron rich in the subsurface. If Unit B has a relative high porosity and permeability, hematite may have been washed out near the surface. There could also be lateral differences in the iron content. Since the whole core was sampled, it gives a better average and was therefore used to represent Unit B. More sampling and drilling must be conducted to establish if the surface is in fact less rich in iron and how extensive this eventually is.
- In the subsurface, the good quality quartzite, extends 4,2 meters below where the boundary to Unit B is defined (Figure 5.27). That is, the upper part of the red colored quartzite is low in iron and aluminum. This, together with the first point, implies that the color of the quartzite is not necessarily correlated to the iron content. Generally, coarse grained hematite will barely influence color, while fine grained hematite will produce intense red colors (Mücke, 1994).
- In the drill core the top 3.5m of Unit A is covered by iron hydroxides, giving it a rusty color and causing an increased iron content. It is not known if this is a local occurrence or if it is representative of the top meters throughout. It is assumed that it is local, therefore the top meter was modeled as Unit A.



- 

Inaccuracies:

- Unit B is modeled to thicken towards the upper part of the limb at the southern part of the SE fold limb. The thickness has likely been miscalculated. The miscalculation most likely occurred because of the change in strike in the location of profile 2 (see Figure 5.18) was not respected properly. A corrected thickness is presented in Figure 5.15.

## 6.5 Future drilling campaign suggestion

In order to increase geological knowledge, a future DDH campaign is proposed. The planned drill hole positions are incorporated in the 3D model. Collar and survey data are listed in Table 7.1 and Table 7.2 respectively. The following considerations were taken when choosing the DDH positions:

- The azimuth and dip of the DDH are (322/59), which is perpendicular to the fold axis strike (143) and the opposite to the angle of local dip (31)
- Master joints are avoided, to prevent the DDH from becoming stuck.
- The spacing between DDH positions is 200m.
- The depth is chosen at 70m. This to include the lower part of the Vaggge Formation.
- Unit B (intermediate quality) is expected to be hit at 38-42m depth below the Vagge Formation.
- Unit C (Bad quality) is expected to be hit between 56 - 58m depth below the Vagge Formation.

Table 6.1: Collar

HOLE	EAST	NORTH	ELEVATION	DEPTH
VR-YY-02	560660.7	7822310.8	404.2	70
VR-YY-03	560808.1	7822445.2	428.1	70
VR-YY-04	560970.2	7822562.8	436.8	70
VR-YY-05	561140.0	7822668.33	436.5	70
VR-YY-06	561315.65	7822764.5	436	70

*Table 6.2: Survey*

HOLE	DEPTH	DIP	AZIM
VR-YY-02	70	59	322
VR-YY-03	70	59	322
VR-YY-04	70	59	322
VR-YY-05	70	59	322
VR-YY-06	70	59	322

## 7 Conclusion

- A gentle, upright, horizontal fold with an axial plane strike extending southeast, folds the Gamafjell Formation.
- Textural and mineralogical maturity decreases with depth impairing the quality of the quartzite.
- Three units could be defined on the basis of visual characteristics and are associated with a recognizable geochemical signature (Table 7.1)

Table 7.1: Characteristics of each unit and their associated quality and maturity.

Units and depths	Characteristics	Quality	Decreasing maturity — ↓
<b>Unit A (0~38m)</b>	Light grey, massive	Good quality	
<b>Unit B (38~56m)</b>	Pink/red, smeared out red bands	Intermediate quality	
<b>Unit C (Below ~56m)</b>	Altering colors of red, crossbedding	Bad quality	

- Surface and DDH analysis are generally in good agreement with each other, both visually and chemically. Surface samples are therefore generally representative of the subsurface. There are however two main deviations.
  - Unit B is more iron rich in the subsurface.
  - The upper 4.2 m of Unit B in the subsurface resembles Unit A chemically.
- There is a strong relation between  $\text{TiO}_2$ ,  $\text{Al}_2\text{O}_3$  and depth. With decreasing depth,  $\text{TiO}_2$  increases and reaches 350-400 ppm at the footwall.
- The strata is highly affected by three main joint sets (J1-J3), in addition to a set of master joints. Joints are often open with weathered surfaces and altered quartzite extending

outwards from the fracture planes, particularly in Unit B. However, no altered quartzite was found in the drill core, indicating that the altered quartzite may not be pervasive.

- The master joints are pervasive and penetrate deep. Severely altered quartzite is associated with these joints. Because the spacing between them is large, they should not be particularly problematic for mining, but the master joints should be avoided when drilling.
- The resource estimation shows that there are large amounts of good and intermediate quality quartzite on the SE fold limb of the Vaggecearru Mountain (Table 7.2). If further drilling proves that the altered quartzite associated with fractures are non-pervasive, the Vaggecearru Mountain should be a promising deposit.

*Table 7.2: Volume and tonnage from resource estimation (rounded to nearest 100 000).*

Quality	Volume (m <sup>3</sup> )	Tonnage
Unit A (Good)	17 200 000	44 720 000
Unit B (Intermediate)	11 700 000	30 160 000

## 8 Futher Work

For Elkem further work will be to continue mapping the area. A profile should be traversed between profile 1 and profile 2, although outcrops are difficult to find in that area. It would however be interesting to see if loose blocks are reliable for sampling, as they should be autoctounious. Diamond Drill holes can be placed at the suggested positions. It will be important to examine how pervasive the altered quartzite in relation to the joints are. HI and TSI test must be performed on more samples, as only four were tested during this project. The 3D model will be exported to a format that can be imported in Vulcan, the modelling software that Elkem uses. The model will have to be updated as geological knowledge increases.

More generally, the Vaggecearru Mountain is a locality, where the region between diagenesis and metamorphism can be studied, as this region is not well defined. Structurally, the there are many interesting features, such as faults, joints and vein arrays that are well displayed. The origin of quartz arenites is still debated, e.g. Dott Jr (2003) suggests that they were formed as a result of, among other things, Precambrian subaerial life forms. The well preserved sedimentary structures makes the Gamasfjell formation well suited for studying quartz arenites.

## 9 References:

- AASLY, K. 2008. *Properties and behavior of quartz for the silicon process*. PhD, NTNU.
- AASLY, K. & ELLEFMO, S. 2014. Geometallurgy applied to industrial minerals operations. *MINERALPRODUKSJON*, 5, A21-A34.
- BOGGS, S. J. 2009. *Petrology of Sedimentary Rocks*, Cambridge University Press.
- BROWN, M. 2015. *AutoStitch* [Online]. Available: <http://www.cs.bath.ac.uk/brown/autostitch/autostitch.html> [Accessed 03 May 2015].
- CHANDLER, F. 1988. Quartz arenites: review and interpretation. *Sedimentary Geology*, 58, 105-126.
- DEER, W., HOWIE, R. & ZUSSMAN, J. 1992. An introduction to the rock-forming minerals (2nd Edition). Longman, England.
- DOLCATER, D., SYERS, J. & JACKSON, M. 1970. Titanium as free oxide and substituted forms in kaolinites and other soil minerals. *Clays Clay Miner*, 18, 71-79.
- DOTT JR, R. 2003. The importance of eolian abrasion in supermature quartz sandstones and the paradox of weathering on vegetation-free landscapes. *The Journal of geology*, 111, 387-405.
- DOTT, R. H. J. 1964. Wacke, Graywacke and Matrix--What Approach to Immature Sandstone Classification? *Journal of Sedimentary Petrology*, 34, 625-632.
- DYAR, GUNTER & TASA 2008. *Mineralogy and Optical Mineralogy*, Mineralogical Society of America.
- FENNER, C. N. 1913. The stability relations of the silica minerals. *American Journal of Science*, 36, 331-384.
- FJELLANGER, J., SØRBEL, L., LINGE, H., BROOK, E. J., RAISBECK, G. M. & YIOU, F. 2006. Glacial survival of blockfields on the Varanger Peninsula, northern Norway. *Geomorphology*, 82, 255-272.
- FJELLANGER, J. N., JOHAN PETTER 2007. Diagenesis and weathering of quartzite at the palaeic surface on the Varanger Peninsula, northern Norway. *Norwegian Journal of Geology*, 87, 133.
- FLEUTY, J. M. 1964. The description of folds. *Proceedings of the Geologists' Association*, 75, 461-492.
- FOSEN, H. 2010. *Structural Geology*, Cambridge, Cambridge University Press.
- JOHNSON, H. D., LEVELL, B. K. & SIEDLECKI, S. 1978. Late Precambrian sedimentary rocks in East Finnmark, north Norway and their relationship to the Trollfjord-Komagelvfelt fault. *Journal of the Geological Society*, 135, 517-533.
- KARTVERK, S. 2014. *Kongsfjorden 2008*.
- KOGEL, J. E., TRIVEDI, N. C., BARKER, J. M. & KRUKOWSKI, S. T. 2006. Industrial Sand and Sandstone. *Industrial Minerals and Rocks - Commodities, Markets, and Uses (7th Edition)*. Society for Mining, Metallurgy, and Exploration (SME).
- MCBRIDE, E. F. 1989. Quartz cement in sandstones: a review. *Earth-Science Reviews*, 26, 69-112.
- MILLIKEN, K. 2003. Late diagenesis and mass transfer in sandstone shale sequences. *Treatise on geochemistry*, 7, 159-190.
- MORAD, S. & ALDAHAN, A. 1987. Diagenetic "replacement" of feldspars by titanium oxides in sandstones. *Sedimentary geology*, 51, 147-153.
- MÜCKE, A. 1994. Part I. Postdiagenetic Ferruginization of Sedimentary Rocks (Sandstones, Oolitic Ironstones, Kaolins and Bauxites)—Including a Comparative Study of The Reddening of Red Beds. *Developments in Sedimentology*, 51, 361-395.
- PETTIJOHN, F. J., POTTER, P. E. & SIEVER, R. 1987. *Sand and Sandstone*, New York, Springer-Verlag New York Inc.
- RAMBERG, I. B., NØTTVEDT, A., BRYHNI, I., SOLLI, A. & NORDGULEN, Ø. 2006. *Landet blir til: Norges geologi*, Norsk geologisk forening.
- RAMSAY, J. G. & HUBER, M. I. 1987. *The Techniques of Modern Structural Geology: Folds and fractures*, Academic Press.

- ROBERTS, D. 1996. Caledonian and Baikalian tectonic structures on Varanger Peninsula, Finnmark, Norway, and coastal areas of Kola Peninsula, NW Russia. *Nor. geol. unders. Bull.*, 431, 59-65.
- ROBERTS, D. & SIEDLECKA, A. 2012. Provenance and sediment routing of Neoproterozoic formations on the Varanger, Nordkinn, Rybachi and Sredni peninsulas, North Norway and Northwest Russia: a review. *Norges geologiske undersøkelse Bulletin*, 452, 1-19.
- SAURO, F. 2014. Structural and lithological guidance on speleogenesis in quartz–sandstone: Evidence of the arenisation process. *Geomorphology*, 226, 106-123.
- SCHEI, A., TUSET, J. K. & TVEIT, H. 1997. *Production of High Silicon Alloys*, Tapir.
- SIEDLECKA, A. 1975. Late Precambrian stratigraphy and structure of the north-eastern margin of the Fennoscandian shield (East-Finnmark - Timan Region). *NGU; Petroleum geology and geology of the North Sea and Northeast Atlantic; Continental Margin.*, Pr 316, 313-348.
- SIEDLECKA, A. 1988. *Tana Berggrunnskart 2335 4, 1:50000*. NGU.
- SIEDLECKA, A. 1990. The bedrock geology of Varanger Peninsula. Excursion Guide. *In: NGU (ed.)*. Trondheim: NGU.
- SOEGAARD, K. & ERIKSSON, K. A. 1989. Origin of thick, first-cycle quartz arenite successions: Evidence from the 1.7 Ga Ortega Group, northern New Mexico. *Precambrian research*, 43, 129-141.
- STØRSETH, L. R. & WANWIK, J. E. 1992. Kvartsressurser i Finnmark. *In: NGU (ed.)*. Trondheim: NGU.
- TANGSTAD, M. 2013. Chapter 6 - Ferrosilicon and Silicon Technology. *In: GASIK, M. (ed.) Handbook of Ferroalloys*. Oxford: Butterworth-Heinemann.
- WEIJERMARS, R. 1997. *Structural geology and map interpretation*, Alboran Science Publishing.
- WILKINSON, M., MILLIKEN, K. L. & HASZELDINE, R. S. 2001. Systematic destruction of K-feldspar in deeply buried rift and passive margin sandstones. *Journal of the Geological Society*, 158, 675-683.
- WORDEN, R. H. & BURLEY, S. 2003. *Sandstone diagenesis: the evolution of sand to stone*, Wiley Online Library.

# Appendix A Sample Locations

SampleID	Sample_Type	Orig_Grid_ID	Orig_North	Orig_East	Orig_RL	Orig_Survey	Method	Orig_Survey	Depth	Date_Sampled	Comments	Has_Duplicate
PR1-10m	SURFACE	Euref89_35N	564283.97	7822948.44	487.045	JP	Jun-Aug 2013	JP	0.0	31.07.2013	IG/G12	YES
PR1-2.5m	SURFACE	Euref89_35N	564283.98	7822950.85	488.045	JP	Jun-Aug 2013	JP	-2.5	31.07.2013	IG/G12	YES
PR1-5.0m	SURFACE	Euref89_35N	564283.96	7822954.23	489.045	JP	Jun-Aug 2013	JP	-5.0	31.07.2013	IG/G12	YES
PR1-7.5m	SURFACE	Euref89_35N	564257.79	7822957.72	489.045	JP	Jun-Aug 2013	JP	-7.5	31.07.2013	IG/G12	YES
PR1-12.5m	SURFACE	Euref89_35N	564282.28	7822982.04	491.045	JP	Jun-Aug 2013	JP	-12.5	31.07.2013	IG/G12	NO
PR1-17.5m	SURFACE	Euref89_35N	564272.13	7822993.74	492.045	JP	Jun-Aug 2013	JP	-17.5	31.07.2013	P/Ind/G12	YES
PR1-20.0m	SURFACE	Euref89_35N	564274.23	7822993.74	493.045	JP	Jun-Aug 2013	JP	-20.0	31.07.2013	P/Ind/G12	YES
PR1-22.5m	SURFACE	Euref89_35N	564274.15	7822910.73	493.045	JP	Jun-Aug 2013	JP	-22.5	04.08.2013	P/Ind/G12	YES
PR1-25.0m	SURFACE	Euref89_35N	564284.95	7822913.17	494.045	JP	Jun-Aug 2013	JP	-25.0	04.08.2013	P/Ind/G12	YES
PR1-27.5m	SURFACE	Euref89_35N	564254.11	7822916.31	494.045	JP	Jun-Aug 2013	JP	-27.5	04.08.2013	P/Ind/G12	YES
PR1-30.0m	SURFACE	Euref89_35N	564255.79	7822917.26	494.045	JP	Jun-Aug 2013	JP	-30.0	04.08.2013	P/Ind/G12	YES
PR1-32.5m	SURFACE	Euref89_35N	564227.25	7823028.18	495.045	JP	Jun-Aug 2013	JP	-32.5	04.08.2013	P/Ind/G12	YES
PR1-35.0m	SURFACE	Euref89_35N	564214.86	7823028.18	495.045	JP	Jun-Aug 2013	JP	-35.0	04.08.2013	P/Ind/G12	NO
PR1-45.0m	SURFACE	Euref89_35N	564221.46	7823072.66	497.045	JP	Jun-Aug 2013	JP	-45.0	04.08.2013	P/Ind/G12	YES
PR2-30m	SURFACE	Euref89_35N	569554.3564	7822183.986	361.045	JP	Jun-Aug 2013	JP	0.0	21.06.2013	IG/G12	YES
PR2-19m	SURFACE	Euref89_35N	569483.6346	7822183.986	341.045	JP	Jun-Aug 2013	JP	-11.0	21.06.2013	IG/G12	YES
PR2-17.5m	SURFACE	Euref89_35N	569486.6346	7822183.986	340.045	JP	Jun-Aug 2013	JP	-12.5	21.06.2013	IG/G12	YES
PR2-15m	SURFACE	Euref89_35N	569484.6501	7822183.986	342.045	JP	Jun-Aug 2013	JP	-15.0	21.06.2013	IG/G12	YES
PR2-13.5m	SURFACE	Euref89_35N	569415.0912	7822183.986	340.045	JP	Jun-Aug 2013	JP	-16.5	21.06.2013	IG/G12	YES
PR2-11.5m	SURFACE	Euref89_35N	569335.1246	7822183.986	340.045	JP	Jun-Aug 2013	JP	-20.0	21.06.2013	IG/G12	YES
PR2-9.5m	SURFACE	Euref89_35N	569332.4455	7822183.986	351.045	JP	Jun-Aug 2013	JP	-26.0	21.06.2013	IG/G12	YES
PR2-7.5m	SURFACE	Euref89_35N	569332.4455	7822183.986	351.045	JP	Jun-Aug 2013	JP	-27.5	21.06.2013	P/Ind/G12	YES
PR2-5.5m	SURFACE	Euref89_35N	569332.4455	7822183.986	352.045	JP	Jun-Aug 2013	JP	-30.0	21.06.2013	P/Ind/G12	YES
PR2-3.5m	SURFACE	Euref89_35N	569332.4455	7822183.986	352.045	JP	Jun-Aug 2013	JP	-32.5	21.06.2013	P/Ind/G12	YES
PR2-1.5m	SURFACE	Euref89_35N	569332.4455	7822183.986	352.045	JP	Jun-Aug 2013	JP	-35.0	21.06.2013	P/Ind/G12	YES
PR2-10m	SURFACE	Euref89_35N	569338.0545	7822183.986	451.045	JP	Jun-Aug 2013	JP	-10.0	21.06.2013	P/Ind/G12	YES
PR2-12.5m	SURFACE	Euref89_35N	569338.0545	7822183.986	451.045	JP	Jun-Aug 2013	JP	-12.5	21.06.2013	P/Ind/G12	YES
PR2-15m	SURFACE	Euref89_35N	569338.0545	7822183.986	451.045	JP	Jun-Aug 2013	JP	-15.0	21.06.2013	P/Ind/G12	YES
PR2-17.5m	SURFACE	Euref89_35N	569338.0545	7822183.986	451.045	JP	Jun-Aug 2013	JP	-17.5	21.06.2013	P/Ind/G12	YES
PR2-20m	SURFACE	Euref89_35N	569338.0545	7822183.986	451.045	JP	Jun-Aug 2013	JP	-20.0	21.06.2013	P/Ind/G12	YES
PR2-22.5m	SURFACE	Euref89_35N	569338.0545	7822183.986	451.045	JP	Jun-Aug 2013	JP	-22.5	21.06.2013	P/Ind/G12	YES
PR2-25m	SURFACE	Euref89_35N	569338.0545	7822183.986	451.045	JP	Jun-Aug 2013	JP	-25.0	21.06.2013	P/Ind/G12	YES
PR2-27.5m	SURFACE	Euref89_35N	569338.0545	7822183.986	451.045	JP	Jun-Aug 2013	JP	-27.5	21.06.2013	P/Ind/G12	YES
PR2-30m	SURFACE	Euref89_35N	569338.0545	7822183.986	451.045	JP	Jun-Aug 2013	JP	-30.0	21.06.2013	P/Ind/G12	YES
PR3-30m	SURFACE	Euref89_35N	559730.79	7824375.47	112.045	JP	16.07.2014	JP	0.0	16.07.2014	IG/G12	NO
PR3-2.5m	SURFACE	Euref89_35N	559730.79	7824375.47	112.045	JP	16.07.2014	JP	-2.5	16.07.2014	IG/G12	NO
PR3-5m	SURFACE	Euref89_35N	559730.79	7824375.47	112.045	JP	16.07.2014	JP	-5.0	16.07.2014	IG/G12	NO
PR3-7.5m	SURFACE	Euref89_35N	559811.45	7824445.26	164.045	JP	16.07.2014	JP	-7.5	16.07.2014	IG/G12	NO
PR3-10m	SURFACE	Euref89_35N	559811.45	7824445.26	164.045	JP	16.07.2014	JP	-10.0	16.07.2014	IG/G12	NO
PR3-12.5m	SURFACE	Euref89_35N	559811.45	7824445.26	164.045	JP	16.07.2014	JP	-12.5	16.07.2014	IG/G12	NO
PR3-15m	SURFACE	Euref89_35N	559900.65	7824445.26	212.045	JP	16.07.2014	JP	-15.0	16.07.2014	IG/G12	NO
PR3-17.5m	SURFACE	Euref89_35N	559900.65	7824445.26	212.045	JP	16.07.2014	JP	-17.5	16.07.2014	IG/G12	NO
PR3-20m	SURFACE	Euref89_35N	559900.65	7824445.26	212.045	JP	16.07.2014	JP	-20.0	16.07.2014	IG/G12	NO
PR3-22.5m	SURFACE	Euref89_35N	559900.65	7824445.26	212.045	JP	16.07.2014	JP	-22.5	16.07.2014	IG/G12	NO
PR3-25m	SURFACE	Euref89_35N	559900.65	7824445.26	212.045	JP	16.07.2014	JP	-25.0	16.07.2014	IG/G12	NO
PR3-27.5m	SURFACE	Euref89_35N	559900.65	7824445.26	212.045	JP	16.07.2014	JP	-27.5	16.07.2014	IG/G12	NO
PR3-30m	SURFACE	Euref89_35N	559900.65	7824445.26	212.045	JP	16.07.2014	JP	-30.0	16.07.2014	IG/G12	NO
PR3-32.5m	SURFACE	Euref89_35N	560256.49	7824392.38	323.045	JP	26.07.2014	JP	-32.5	26.07.2014	P/Ind/G12	NO
PR3-35m	SURFACE	Euref89_35N	560256.49	7824392.38	323.045	JP	26.07.2014	JP	-35.0	26.07.2014	P/Ind/G12	NO
PR3-40m	SURFACE	Euref89_35N	560256.49	7824392.38	323.045	JP	26.07.2014	JP	-40.0	26.07.2014	P/Ind/G12	NO
PR3-45m	SURFACE	Euref89_35N	560256.49	7824392.38	323.045	JP	26.07.2014	JP	-45.0	26.07.2014	P/Ind/G12	NO



## Appendix B Material and methods

List of methods used to analyze specific samples.

Reference	ICP - IOS	Microscopy	Microprobe	XRD	TSI
Pr1-0m	x	x			x
Pr1-2.5m	x	x			
Pr1-5.0m	x				
Pr1-7.5m	x	x			
Pr1-12.5m	x				
Pr1-17.5m	x	x			x
Pr1-20.0m	x	x			
Pr1-22.5m	x	x			
Pr1-25.0m	x	x			
Pr1-27.5m	x	x	x		
Pr1-30.0m	x	x			
Pr1-32.5m	x	x			
Pr1-35.0m	x				
Pr1-45.0m	x	x			
PR2+30.0m	x	x			
PR2+19m	x				
PR2+17.5m	x	x		x	
PR2+15.0m	x				
PR2+13.5m	x	x	x		
PR2+10m	x	x			
PR2+7.5m	x				
PR2+5m	x				
PR2+2.5m	x				
PR2-0	x	x			
PR2-2.5m	x	x			x

PR2-5m	x	x		x	
PR2-7.5m	x				x
PR2-10m	x				
PR2-12.5m	x				
PR2-15m	x	x			
PR2-17.0m	x	x			
PR2-19.5m	x	x			
PR2-22m	x	x	x		
PR2-25m	x	x			
PR2-27.5m	x				
PR2-30m	x	x	x	x	
PR3-0m	x				
PR3-2.5m	x				
PR3-5m	x				
PR3-7.5m	x				
PR3-10m	x				
PR3-12.5m	x				
PR3-15m	x				
PR3-17.5m	x				
PR3-30m	x				
PR3-32.5m	x				
PR3-37.5m	x				
PR3-40m	x				
PR3-42.5m	x				
PR3-44m	x				
VR-14-01-001	x				
VR-14-01-002	x				

VR-14-01-003	x				
VR-14-01-004	x				
VR-14-01-005	x				
VR-14-01-006	x				
VR-14-01-007	x				
VR-14-01-008	x				
VR-14-01-009	x				
VR-14-01-010	x				
VR-14-01-011	x				
VR-14-01-012	x				
VR-14-01-013	x				
VR-14-01-014	x				
VR-14-01-015	x				
VR-14-01-016	x				
VR-14-01-017	x				

VR-14-01-018	x				
VR-14-01-019	x				
VR-14-01-020	x				
VR-14-01-021	x				
VR-14-01-022	x				
VR-14-01-023	x				
VR-14-01-024	x				

## Appendix C Microprobe results

Results from microprobe, expressed in Wt % (normalized) of element.

Comment							
	Zirkon	Zirkon	Rutil	Hematite	Hematite	Rutile	Rutile
Sample	PR2-30.1	PR2-30.2	PR2-30.3	PR2-30.4	PR2-30.5	PR2-30.6	PR2-30.7
Total	100.0000	100.0000	100.0000	100.0000	100.0000	100.0001	100.0000
La	0.0000	0.0000	0.0000	0.0000	0.0000	0.0000	0.0000
Ce	0.0000	0.0000	0.0000	0.0000	0.0000	0.0000	0.0000
Nd	0.0000	0.0000	0.0000	0.0000	0.0000	0.0000	0.0000
Zr	16.4102	15.7344	0.0131	0.0159	0.0532	0.0085	0.0199
Y	0.0303	0.1651	0.0017	0.0099	0.0497	0.0014	0.0000
Ti	0.0035	0.0138	29.6401	0.4172	0.7968	30.3548	29.6952
Si	18.2526	17.0984	0.5661	12.0308	7.0388	0.4767	0.3927
Ca	0.0000	0.0199	0.0000	0.0265	0.0297	0.0088	0.0027
Al	0.0000	0.0611	0.0650	9.2216	4.8001	0.0966	0.0759
K	0.0000	0.0022	0.0320	2.1229	1.0553	0.0280	0.0172
Fe	0.0062	0.1104	1.0919	12.9332	26.4829	0.8626	1.2244
Mg	0.0000	0.0000	0.0000	0.1776	0.0912	0.0005	0.0000
P	0.0012	0.2378	0.0022	0.0160	0.0576	0.0062	0.0163
B	0.0000	0.0000	0.0000	2.2007	2.5092	0.0746	0.0105
Mn	0.0239	0.0000	0.0000	0.0000	0.0109	0.0000	0.0060
O	65.2685	66.5534	68.5879	60.7734	57.0247	68.0790	68.4998
Na	0.0036	0.0035	0.0000	0.0542	0.0000	0.0024	0.0394
No.	1	2	3	4	5	6	7

			Tourmalin		Tourmalin		Tourmalin		Tourmalin		Tourmalin		Tourmalin		Zirkon			
Rutile	Zirkon	Rutile	e	e	e	Rutile	e	e	e	e	Zirkon	?						
PR2-30.8	PR2-30.9	PR2-30.10	PR2-30.11	PR2-30.12	PR2-30.13	PR2-30.14	PR2-30.15	PR2-30.16	PR2-	PR2-	100.0000	100.0000	100.0000	100.0000	100.0000	100.0000	100.0000	100.0000
100.0000	100.0000	100.0000	100.0000	100.0000	100.0000	100.0000	100.0000	100.0000	100.0000	100.0000	100.0000	100.0000	100.0000	100.0000	100.0000	100.0000	100.0000	100.0000
0.0000	0.0000	0.0000	0.0000	0.0000	0.0000	0.0000	0.0000	0.0000	0.0000	0.0000	0.0000	0.0000	0.0000	0.0000	0.0000	0.0000	0.0000	0.0000
0.0000	0.0000	0.0000	0.0000	0.0000	0.0000	0.0000	0.0000	0.0000	0.0000	0.0000	0.0000	0.0000	0.0000	0.0000	0.0000	0.0000	0.0000	0.0000
0.0000	0.0000	0.0000	0.0000	0.0000	0.0000	0.0000	0.0000	0.0000	0.0000	0.0000	0.0000	0.0000	0.0000	0.0000	0.0000	0.0000	0.0000	0.0000
0.0128	16.1157	0.0000	0.0008	0.0046	0.0062	0.0000	0.0000	0.0000	0.0000	0.0000	15.9690	0.0702						
0.0000	0.0000	0.0287	0.0000	0.0000	0.0000	0.0288	0.0099	0.0052	0.0000	0.0000	0.0000	0.0000						
29.4944	0.0036	30.1816	0.1175	0.3489	0.1885	29.9916	0.1889	0.1034	0.0007	0.0007	0.0007	0.1182						
0.7411	18.2402	0.5153	11.7194	11.5040	11.4638	0.4299	11.5036	11.5809	18.2560	26.4979								
0.0000	0.0055	0.0012	0.7876	0.4408	0.1929	0.0049	0.1451	0.0667	0.0055	0.0305								
0.0211	0.0404	0.0260	8.8498	9.9530	10.8447	0.1782	10.0710	11.9703	0.0141	2.6518								
0.0053	0.0111	0.0005	0.0224	0.0218	0.0349	0.0203	0.0254	0.0220	0.0085	0.6509								
0.8848	0.0591	0.9261	4.5306	3.8743	2.6853	0.7188	2.1702	1.9891	0.0218	5.4806								
0.0000	0.0000	0.0000	3.4061	2.6082	3.0805	0.0060	4.1198	2.7854	0.0072	0.0680								
0.0000	0.0000	0.0096	0.0056	0.0016	0.0016	0.0060	0.0001	0.0068	0.0000	0.2465								
0.0000	0.0000	0.0000	8.6090	8.4981	8.1604	0.0000	8.5010	7.9498	0.0000	0.0000								
0.0000	0.0369	0.0054	0.0185	0.0061	0.0046	0.0000	0.0100	0.0018	0.0021	0.0041								
68.8405	65.4538	68.3056	61.1884	61.5606	61.8145	68.6107	61.6160	62.3490	65.6929	64.1549								
0.0000	0.0336	0.0000	0.7444	1.1780	1.5221	0.0047	1.6390	1.1696	0.0221	0.0265								
8	9	10	11	12	13	14	15	16	17	18								

									Tourmalin	
Matrix	Matrix	Hematite	Hematite	Rutile	Rutile	Rutile	Matrix	Matrix	e	Hematite
PR2-	PR2-	PR2-	PR2-	PR2-	PR2-	PR2-	PR2-	PR2-	PR2-	PR2-
100.0000	100.0000	100.0000	100.0000	100.0000	100.0000	100.0000	100.0000	100.0000	99.9999	100.0000
0.0000	0.0000	0.0000	0.0000	0.0000	0.0000	0.0000	0.0000	0.0000	0.0000	0.0000
0.0000	0.0000	0.0000	0.0000	0.0000	0.0000	0.0000	0.0000	0.0000	0.0000	0.0000
0.0000	0.0000	0.0000	0.0000	0.0000	0.0000	0.0000	0.0000	0.0000	0.0000	0.0000
0.0352	0.1314	0.1004	0.0000	0.0054	0.0031	0.0000	0.0435	0.0192	0.0008	0.0041
0.0000	0.0000	0.0039	0.0000	0.0121	0.0000	0.0000	0.0221	0.0176	0.0000	0.0000
0.0525	0.2116	0.5292	1.3024	25.8920	30.6338	30.7450	0.4262	0.3707	0.1859	0.1079
17.7460	15.5719	10.2935	1.0350	2.3340	0.4923	0.4182	11.9933	9.0230	11.3324	1.5500
0.0420	0.0527	0.0310	0.0000	0.0067	0.0000	0.0014	0.0246	0.0026	0.1469	0.0000
13.2144	10.3009	7.9688	0.2618	1.2573	0.0185	0.0351	9.4542	6.9722	12.4722	0.5729
3.6398	3.1573	2.0900	0.0306	0.3773	0.0057	0.0090	2.5302	1.8059	0.0238	0.0046
2.4724	5.3866	19.3407	36.0614	0.3278	0.6771	0.3751	18.4690	16.9993	1.8165	35.5723
0.3290	0.4038	0.2189	0.0000	0.0409	0.0000	0.0000	0.2033	0.1746	2.6336	0.0315
0.0517	0.1849	0.1356	0.0312	0.0346	0.0110	0.0087	0.0352	0.0076	0.0069	0.0730
0.5826	1.3907	0.7691	2.4900	0.0000	0.0000	0.0000	1.2447	3.5049	7.5052	4.7393
0.0011	0.0126	0.0088	0.0182	0.0000	0.0000	0.0107	0.0000	0.0107	0.0105	0.0079
61.7668	63.0747	58.4164	58.7693	69.6961	68.1585	68.3804	55.4490	61.0280	62.7631	57.3365
0.0664	0.1209	0.0937	0.0000	0.0158	0.0000	0.0164	0.1046	0.0636	1.1021	0.0000
19	20	21	22	23	24	25	26	27	28	29

Tourmalin e	Tourmalin				Matrinks +				Pyrophyllit e	
	Hematite	Matrix	Rutile	Matrix	Hematite	Rutile	Hematite	Hematite		
PR2-	PR2-	PR2-	PR2-	PR2-	PR2-	PR2-	PR2-	PR2+13,5	PR2+13,5	
100.0000	100.0000	100.0000	100.0000	100.0000	100.0000	100.0000	100.0001	100.0000	100.0000	
0.0000	0.0000	0.0000	0.0000	0.0000	0.0000	0.0000	0.0000	0.0000	0.0000	
0.0000	0.0000	0.0000	0.0000	0.0000	0.0000	0.0000	0.0000	0.0000	0.0000	
0.0000	0.0000	0.0000	0.0000	0.0000	0.0000	0.0000	0.0000	0.0000	0.0000	
0.0000	0.0251	0.0253	0.0096	0.0120	0.0000	0.0103	0.0000	0.0061	0.0044	
0.0078	0.0962	0.0000	0.0000	0.0423	0.0000	0.0052	0.0440	0.0287	0.0000	
0.1279	1.6732	0.5059	29.6929	0.0253	0.2482	0.7944	0.7915	0.0747	0.0006	
11.3726	0.5686	1.3205	0.5964	21.4242	11.4199	0.4121	9.0335	1.0358	25.3134	
0.0381	0.0000	0.6933	0.0000	0.0246	0.1803	0.0000	0.0227	0.0000	0.0225	
12.0979	0.2445	15.6595	0.0446	13.9658	11.3301	0.2986	6.4858	0.0875	11.6535	
0.0126	0.0144	0.1234	0.0165	2.7013	0.0197	0.0118	1.6801	0.0350	0.0231	
2.4879	38.4259	0.5677	0.9703	0.9320	2.9679	36.3573	29.7101	40.1922	0.0313	
1.8794	0.0087	0.0486	0.0023	0.3978	1.9070	0.0000	0.0930	0.0143	0.0279	
0.0050	0.0166	6.4504	0.0000	0.0100	0.0000	0.1857	0.0038	0.0000	0.0010	
7.8844	2.9358	0.8681	0.0000	0.0000	8.5411	2.7767	4.6643	2.6408	0.0000	
0.0113	0.0007	0.0000	0.0118	0.0000	0.0123	0.0000	0.0000	0.0802	0.0040	
62.8213	55.9902	73.7373	68.6555	60.3026	62.1760	59.1342	47.3790	55.7164	62.7978	
1.2539	0.0000	0.0000	0.0000	0.1622	1.1976	0.0137	0.0924	0.0882	0.1205	
30	31	32	33	34	35	36	37	38	39	40



Pyrophyllit	e			Horblend	e?					
	Rutile	Rutile	Quartz		Inclusion	Rutile	Monazite	Quartz	Sericite	Sericite
PR2+13,5	PR2+13,5	PR2+13,5	PR2+13,5	PR2+13,5	PR2+13,5	PR2+13,5	PR2+13,5	PR2+13,5	PR2+13,5	PR2+13,5
100.0000	99.99999	100.00000	100.00000	100.00000	100.00002	100.00000	100.00000	100.00000	100.00000	100.00000
0.0000	0.0000	0.0000	0.0000	0.0000	2.9568	0.0000	3.2562	0.0000	0.0000	0.0000
0.0000	0.0000	0.0000	0.0000	0.0000	6.5214	0.0000	7.2408	0.0000	0.0000	0.0000
0.0000	0.0000	0.0000	0.0000	0.0000	3.3025	0.0000	2.9017	0.0000	0.0000	0.0000
0.0033	0.0040	0.0103	0.0000	0.0020	0.0016	0.0018	0.0235	0.0000	0.0000	0.0087
0.0000	0.0000	0.0000	0.0000	0.0080	0.3616	0.0256	0.9658	0.0000	0.0002	0.0000
0.0000	30.6692	31.7580	0.0000	0.3002	0.0000	29.7359	0.0042	0.0006	0.0099	0.0141
20.8522	0.5452	0.5168	28.9379	18.2554	1.5252	0.4738	2.2349	28.4856	18.1522	23.3468
0.0096	0.0000	0.0016	0.0213	0.0187	0.4074	0.0013	0.1405	0.0020	0.0552	0.0614
9.8344	0.1397	0.0160	0.0154	13.3564	0.0000	0.0402	0.0000	0.2317	15.3229	19.1872
0.0206	0.0039	0.0000	0.0000	3.3230	0.0022	0.0000	0.0011	0.0491	4.3632	5.3372
0.0087	0.2585	0.2015	0.0042	1.6142	0.0000	0.8880	0.0000	0.0122	0.1160	0.1182
0.0000	0.0023	0.0039	0.0539	0.2713	0.0000	0.0224	0.0010	0.0000	0.0871	0.0599
0.0037	0.0000	0.0000	0.0025	0.0005	16.0430	0.0000	16.0739	0.0000	0.0000	0.0124
0.0000	0.0000	0.0000	0.0000	0.0216	0.0000	0.0000	0.2072	0.0000	0.5856	0.0000
0.0009	0.0000	0.0000	0.0000	0.0104	0.0000	0.0000	0.0000	0.0000	0.0000	0.0000
69.2438	68.3771	67.4919	70.9648	62.6860	68.8785	68.7690	66.9491	71.2188	61.1352	51.6298
0.0228	0.0000	0.0000	0.0000	0.1323	0.0000	0.0420	0.0000	0.0000	0.1726	0.2244
41	42	43	44	45	46	47	48	49	50	51

Zirkon	Imnestlutnin		Pyrophyllit		Pyrophyllit		Pyrophyllit		Pyrophyllit		Pyrophyllit		Pyrophyllit		Pyrophyllit		Pyrophyllit		Pyrophyllit		
	g		e		e		e		e		Quartz		Quartz		e		Matrix				
PR2+13,5	PR1-	PR1-	PR1-	PR1-	PR1-	PR1-	PR1-	PR1-	PR1-	PR1-	PR1-	PR1-	PR1-	PR1-	PR1-	PR1-	PR1-	PR1-	PR1-	PR1-	
100.0000	100.0000	100.0000	99.9998	100.0000	100.0000	100.0000	100.0000	100.0000	100.0000	100.0000	100.0001	100.0000	100.0000	100.0000	100.0000	100.0000	100.0000	100.0000	100.0000	100.0000	
0.0000	0.0000	0.0000	0.0000	0.0000	0.0000	0.0000	0.0000	0.0000	0.0000	0.0000	0.0000	0.0000	0.0000	0.0000	0.0000	0.0000	0.0000	0.0000	0.0000	0.0000	
0.0000	0.0000	0.0000	0.0000	0.0000	0.0000	0.0000	0.0000	0.0000	0.0000	0.0000	0.0000	0.0000	0.0000	0.0000	0.0000	0.0000	0.0000	0.0000	0.0000	0.0000	
0.0000	0.0000	0.0000	0.0000	0.0000	0.0000	0.0000	0.0000	0.0000	0.0000	0.0000	0.0000	0.0000	0.0000	0.0000	0.0000	0.0000	0.0000	0.0000	0.0000	0.0000	
14.9459	0.0006	0.0145	0.0000	0.0090	0.0018	0.0009	0.0009	0.0009	0.0009	0.0000	0.0000	0.0050	0.0000	0.0000	0.0000	0.0000	0.0000	0.0000	0.0000	0.0000	
0.1240	0.0004	0.0132	0.0081	0.0046	0.0000	0.0121	0.0000	0.0121	0.0000	0.0000	0.0000	0.0075	0.0000	0.0000	0.0000	0.0000	0.0000	0.0000	0.0000	0.0000	
0.0191	0.0020	0.0000	0.0000	0.0009	0.0013	0.0057	0.0537	0.0281	0.0000	0.0000	0.0537	0.0281	0.0000	0.0000	0.0000	0.0000	0.0000	0.0000	0.0000	0.0016	
19.1426	0.8305	22.5570	23.5217	23.0640	21.7322	22.5683	28.6512	29.0544	24.8492	15.1584	28.6512	29.0544	24.8492	15.1584	24.8492	15.1584	24.8492	15.1584	15.1584	15.1584	15.1584
0.0237	14.3816	0.0110	0.0067	0.0061	0.0027	0.0056	0.0000	0.0000	0.0067	0.0055	0.0000	0.0000	0.0000	0.0067	0.0055	0.0000	0.0055	0.0055	0.0055	0.0055	
0.0292	0.0076	10.5897	11.0405	10.8651	10.1652	10.7337	0.1349	0.1648	11.4245	18.4177	0.1349	0.1648	11.4245	18.4177	11.4245	18.4177	11.4245	18.4177	18.4177	18.4177	
0.0000	0.0041	0.0051	0.0563	0.0183	0.0136	0.0270	0.0248	0.0355	0.0116	0.5217	0.0248	0.0355	0.0116	0.5217	0.0116	0.5217	0.0116	0.5217	0.5217	0.5217	
0.0230	0.0000	0.0933	0.0776	0.0820	0.1005	0.0760	0.0235	0.2920	0.0628	0.2267	0.0235	0.2920	0.0628	0.2267	0.0628	0.2267	0.0628	0.2267	0.2267	0.2267	
0.0152	0.0146	0.0108	0.0057	0.0182	0.0060	0.0149	0.0026	0.0145	0.0000	0.0117	0.0026	0.0145	0.0000	0.0117	0.0000	0.0117	0.0000	0.0117	0.0117	0.0117	
0.0218	0.0099	0.0000	0.0063	0.0000	0.0039	0.0000	0.0044	0.0000	0.0000	0.0000	0.0044	0.0000	0.0000	0.0000	0.0000	0.0000	0.0000	0.0000	0.0000	0.0000	
0.0000	3.9598	0.0000	0.0000	0.2597	1.8103	0.0000	0.0000	0.0000	0.0000	0.1875	0.0000	0.0000	0.0000	0.1875	0.0000	0.1875	0.0000	0.1875	0.1875	0.1875	
0.0073	0.0000	0.0024	0.0000	0.0000	0.0000	0.0000	0.0000	0.0000	0.0052	0.0000	0.0000	0.0000	0.0052	0.0000	0.0052	0.0000	0.0052	0.0052	0.0052	0.0052	
65.6483	80.7559	66.6490	65.2663	65.6254	66.1371	66.5379	71.1050	70.3982	63.6401	65.4511	71.1050	70.3982	63.6401	65.4511	63.6401	65.4511	63.6401	65.4511	65.4511	65.4511	
0.0000	0.0330	0.0540	0.0106	0.0467	0.0254	0.0179	0.0000	0.0000	0.0000	0.0181	0.0000	0.0000	0.0000	0.0181	0.0000	0.0181	0.0000	0.0181	0.0181	0.0181	
52	53	54	55	56	57	58	59	60	61	62											

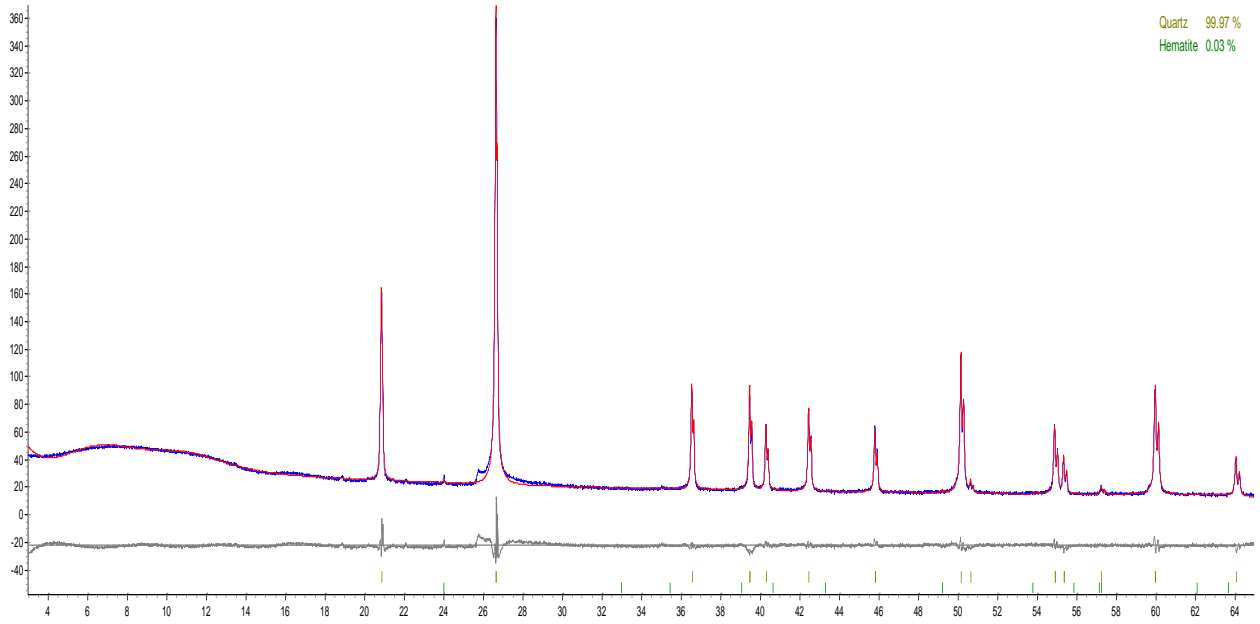


					Pyrophyllit e	Hornbleen de ?	Zirkon
Rutile	Quartz	Zirkon	?				
PR2-	PR2-	PR2-	PR2-	PR2-	PR2-	PR2-	PR2-
100.0000	100.0000	99.9999	100.0000	100.0000	100.0000	100.0000	100.0000
0.0000	0.0000	0.0000	0.0000	0.0000	0.0000	0.0000	0.0000
0.0000	0.0000	0.0000	0.0000	0.0000	0.0000	0.0000	0.0000
0.0000	0.0000	0.0000	0.0000	0.0000	0.0000	0.0000	0.0109
0.0000	0.0049	15.3387	0.0005	0.0000	0.0000	0.0000	14.1836
0.0031	0.0000	0.0000	0.0000	0.0000	0.0000	0.0011	0.8707
30.4793	0.0014	0.0000	0.0047	0.0054	0.1335	0.0138	0.0138
0.7406	28.3398	18.0661	23.9358	24.0583	16.9542	15.5787	15.5787
0.0055	0.0070	0.0007	0.0000	0.0144	2.9489	0.0803	0.0803
0.0597	0.2441	0.0050	7.5336	12.3610	4.8232	0.5756	0.5756
0.0000	0.0070	0.0000	5.8734	0.0490	0.8474	0.0000	0.0000
0.6972	0.0022	0.0271	0.0000	0.1441	7.0417	0.4173	0.4173
0.0000	0.0010	0.0226	0.0000	0.0362	4.4598	0.0274	0.0274
0.0000	0.0292	0.0000	0.0000	0.0109	0.0000	1.1236	1.1236
0.0000	0.0000	0.0000	0.0000	0.0000	1.3048	0.0000	0.0000
0.0072	0.0000	0.0128	0.0000	0.0006	0.1692	0.0000	0.0000
68.0073	71.3633	66.4458	62.0062	63.2928	60.0244	67.1182	67.1182
0.0000	0.0000	0.0810	0.6458	0.0273	1.2919	0.0000	0.0000
74	75	76	77	78	79	80	

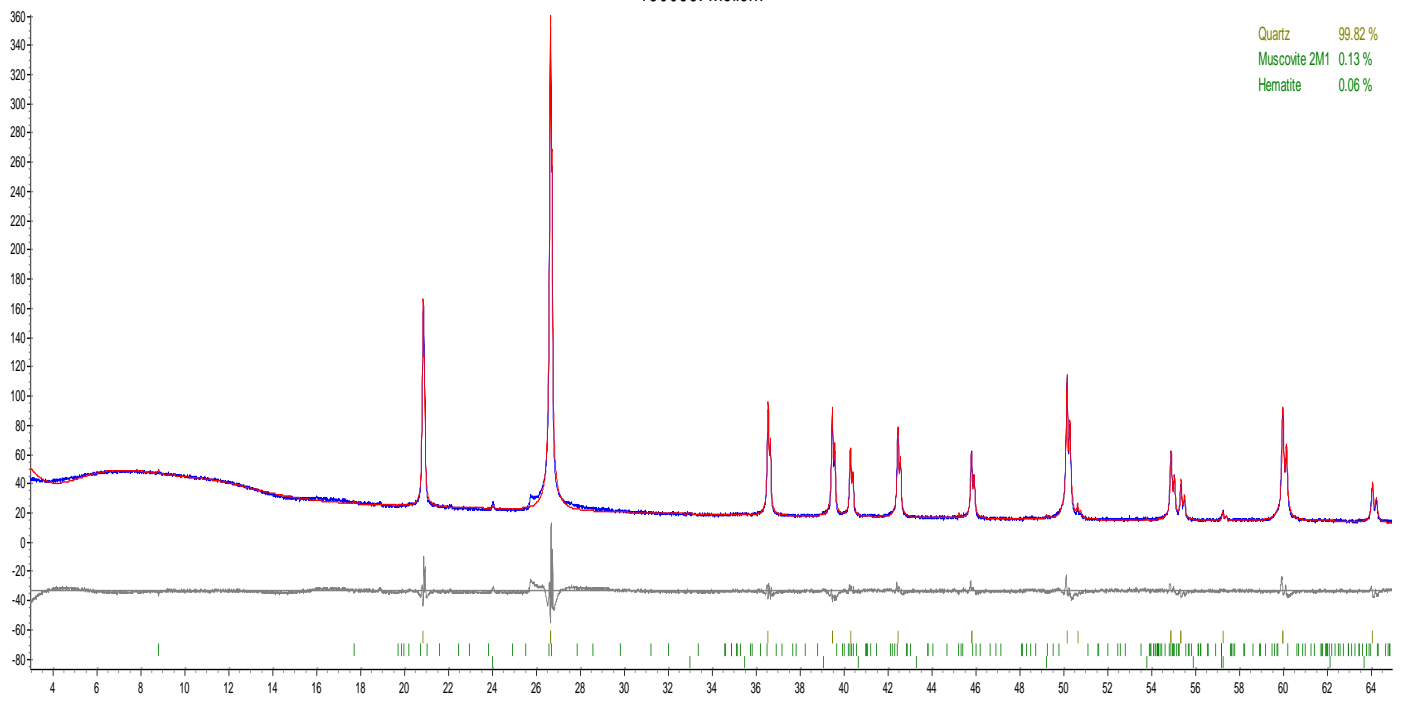
## Appendix D XRD Results:

Results of XRD. Lys corresponds to (Pr2+17,5), Mellom corresponds to (Pr2-5), Mørk corresponds to (Pr2-30),

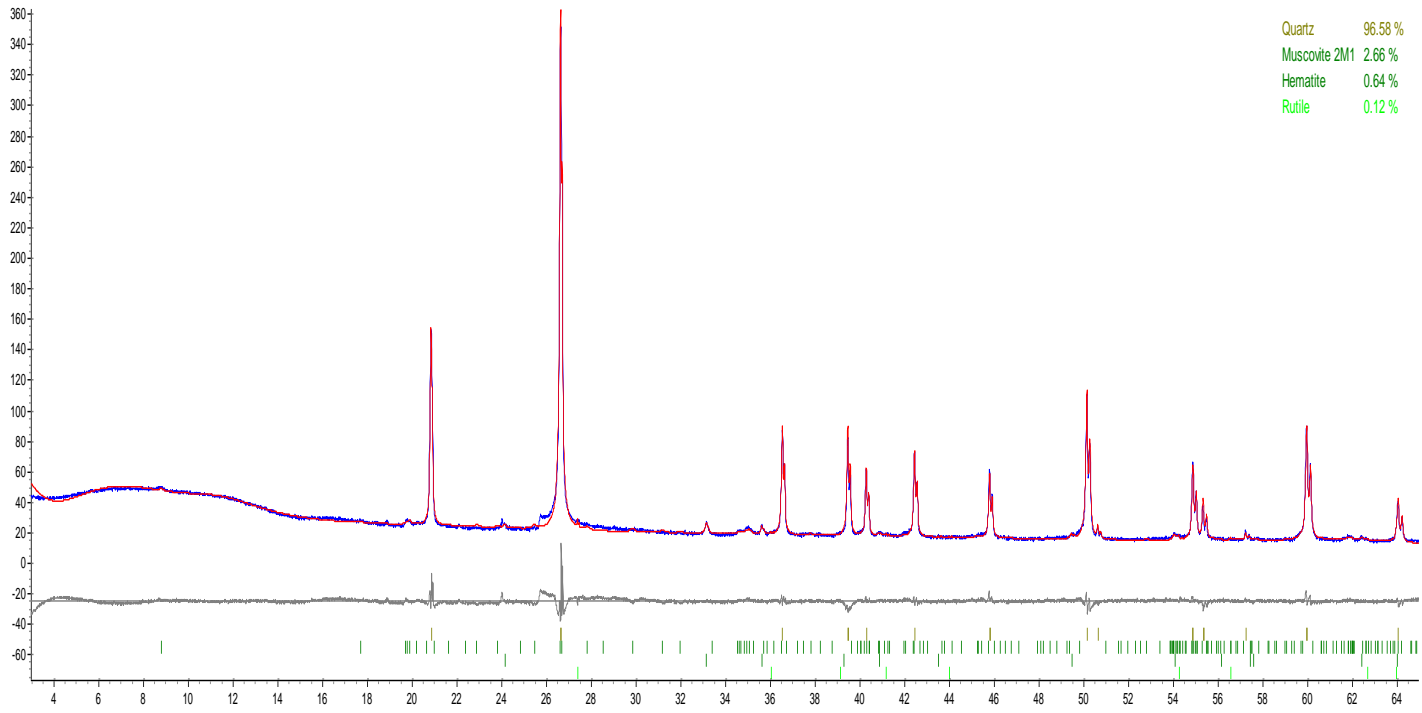
150067: Lys



150066: Mellom



150065: Mørk



## Appendix E Bulk chemistry of all samples

Results from ICP – OES analysis.

Org. Ref:	Org. Depth	Estimated Depth	Profile 1															
			Al2O3	Fe2O3	TiO2	CaO	Mn2O	K2O	MgO	MnO	P2O5	B2O3	Pil. Color	Sec. Color				
	m	m	%	%	ppm	%	%	%	%	%	ppm	ppm	ppm	ppm	ppm			
P1-0m	0.0	-26	0.347	0.0273	223.9	0.0027	0.0036	0.0620	0.0038	1.5	97.5					Light Gray		
P1-2.5m	-2.5	-29	0.290	0.0259	205.4	0.0028	0.0027	0.0474	0.0030	2.6	89.1					Light Gray		
P1-5.0m	-5.0	-32	0.296	0.0204	193.3	0.0033	0.0029	0.0447	0.0030	2.8	52.6					Light Gray		
P1-7.5m	-7.5	-35	0.219	0.0264	187.0	0.0030	0.0027	0.0341	0.0028	2.6	56.0					Light Gray		
P1-12.5m	-12.5	-38	0.355	0.0251	219.8	0.0037	0.0037	0.0554	0.0034	2.5	66.0					Light Pink		
P1-17.5m	-17.5	-43	0.446	0.3404	288.7	0.0037	0.0052	0.0816	0.0050	5.9	43.3					Dark Red	Red	
P1-20.0m	-20.0	-46	0.402	0.0376	216.5	0.0032	0.0052	0.0604	0.0044	1.2	36.7					Light Pink	Pink	
P1-22.5m	-22.5	-49	0.202	0.0635	196.6	0.0030	0.0033	0.0379	0.0033	3.1	35.6					Dark Red	Pink	
P1-25.0m	-25.0	-52	0.420	0.0345	244.1	0.0030	0.0033	0.0622	0.0041	10.4	38.7					Light Pink		
P1-27.5m	-27.5	-55	0.541	0.0528	230.9	0.0028	0.0040	0.0716	0.0042	3.8	31.8					Red		
P1-30.0m	-30.0	-58	0.741	0.5550	256.7	0.0026	0.0051	0.1181	0.0058	50.7	18.9					Dark Red		
P1-32.5m	-32.5	-61	0.525	0.0587	361.5	0.0034	0.0043	0.0683	0.0053	3.7	44.0					Red	Pink	
P1-35.0m	-35.0	-64	1.074	0.0657	559.1	0.0035	0.0067	0.1253	0.0059	4.1	100.3					Red	Pink	
P1-45.0m	-45.0	-76	0.442	0.3896	381.9	0.0037	0.0040	0.1014	0.0066	4.4	49.3					Violet	Pink	

Org. Ref:	Org. Depth	Estimated Depth	Profile 2															
			Al2O3	Fe2O3	TiO2	CaO	Mn2O	K2O	MgO	MnO	P2O5	B2O3	Pil. Color	Sec. Color				
	m	m	%	%	ppm	%	%	%	%	ppm	ppm	ppm	ppm	ppm				
PR2+30.0m	0.0	0	0.267	0.0482	223.4	0.0032	0.0032	0.0628	0.0081	9.3	61.7					Light Gray		
PR2+19m	-11.0	-7	0.49	0.073	251	0.004	0.005	0.097	0.005	15.4	82.5					Light Gray		
PR2+17.5m	-12.5	-17	0.20	0.023	158	0.003	0.002	0.039	0.003	16.8	48.7					Light Gray		
PR2+15.0m	-15.0	-20	0.464	0.0474	234.3	0.0032	0.0036	0.0719	0.0045	6.3	45.0					Light Gray		
PR2+13.5m	-16.5	-23	0.27	0.055	183	0.003	0.003	0.037	0.003	87.0	47.3					Light Gray		
PR2+10m	-20.0	-26	0.39	0.030	204	0.003	0.003	0.066	0.004	5.9	50.1					Light Gray		
PR2+7.5m	-22.5	-29	0.493	0.0493	254.7	0.0033	0.0037	0.0846	0.0052	6.0	60.1					Pink	Red	
PR2+6m	-25.0	-32	0.17	0.021	161	0.003	0.002	0.028	0.002	11.3	46.0					Light Gray		
PR2+2.5m	-27.5	-35	0.370	0.0433	198.6	0.0032	0.0029	0.0530	0.0031	19.9	29.7					Light Pink		
PR2 0	-30.0	-38	0.29	0.105	239	0.002	0.002	0.047	0.003	2.4	48.1					Red	Pink	
PR2-2.5m	-32.5	-40.5	0.316	0.0416	232.5	0.0034	0.0031	0.0551	0.0037	5.3	57.5					Pink	Pink	
PR2-5m	-35.0	-43	0.38	0.085	257	0.003	0.003	0.062	0.004	6.1	37.7					Light Pink	Red	
PR2-7.5m	-37.5	-45.5	0.796	0.0952	324.3	0.0039	0.0056	0.1124	0.0060	33.7	47.3					Pink		
PR2-10m	-40.0	-48	0.39	0.044	241	0.003	0.004	0.086	0.005	9.4	34.5					Light Pink		
PR2-12.5m	-42.5	-50.5	0.306	0.0295	234.1	0.0036	0.0032	0.0699	0.0043	4.3	49.8					Red		
PR2-15m	-45.0	-53	0.21	0.036	212	0.004	0.003	0.037	0.003	16.7	56.4					Light Pink		
PR2-17.0m	-47.0	-56	0.679	0.0556	355.6	0.0039	0.0045	0.0986	0.0061	9.1	70.1					Pink		
PR2-19.5m	-49.0	-58.5	0.537	0.0471	311.2	0.0033	0.0045	0.0789	0.0043	14.4	85.8					Pink	Red	
PR2-22m	-52.0	-61.5	1.08	0.136	386	0.004	0.006	0.204	0.011	32.0	69.2					Red	Pink	
PR2-25m	-55.0	-64.5	0.52	0.087	314	0.004	0.004	0.118	0.007	10.1	66.8					Pink		
PR2-27.5m	-57.5	-67	0.55	0.060	285	0.004	0.005	0.120	0.006	5.1	63.2					Pink		
PR2-30m	-60.0	-69.5	1.69	0.686	850	0.006	0.009	0.448	0.026	7.9	218.9					Violet	Pink	

Profile 3										
Org. Ref:	Al2O3	Fe2O3	TiO2	CaO	Na2O	K2O	MgO	MnO	P2O5	B2O3
	%	%	ppm	%	%	%	%	ppm	ppm	ppm
PR3-0m	0.217	0.0346	166.8	0.0032	0.0031	0.0425	0.0034	37.2	40.8	
PR3-2.5m	0.305	0.0437	131.6	0.0033	0.0051	0.0516	0.0033	44.7	52.8	
PR3-5m	0.550	0.0645	240.0	0.0040	0.0042	0.1197	0.0057	13.4	102.8	15.0
PR3-7.5m	0.521	0.0512	294.3	0.0035	0.0052	0.1096	0.0058	34.1	44.7	15.5
PR3-10m	0.252	0.0383	197.7	0.0031	0.0036	0.0542	0.0035	23.7	62.4	
PR3-12.5m	1.613	0.1745	644.6	0.0042	0.0146	0.2303	0.0093	7.7	107.7	
PR3-15m	0.338	0.0739	226.2	0.0046	0.0084	0.0618	0.0038	19.6	54.8	
PR3-17.5m	0.585	0.0504	223.7	0.0040	0.0101	0.1173	0.0054	9.9	48.4	
PR3-30m	0.488	0.0570	489.9	0.0051	0.0081	0.0653	0.0053	17.7	64.6	
PR3-32.5m	1.207	0.0924	419.9	0.0060	0.0139	0.1163	0.0061	4.3	74.7	
PR3-37.5m	0.370	0.0431	179.8	0.0050	0.0070	0.0636	0.0049	6.6	53.6	
PR3-40m	0.581	0.0458	234.0	0.0046	0.0078	0.1130	0.0061	6.9	94.1	
PR3-42.5m	1.090	0.0834	509.6	0.0076	0.0075	0.2478	0.0106	6.8	225.1	
PR3-44m	0.500	0.0655	430.5	0.0062	0.0061	0.1192	0.0068	13.0	57.8	



VR-14-01

References:	From	To	A203	Fe203	TiO2	CaO	Na2O	K2O	MgO	MnO	P2O5	B2O3	Color	Sec. Color
VR-14-01-001	2.3	5.8	0.432	0.1922	166.0221	0.0045	0.0068	0.0804	0.0071	18.1847	39.1414		Light Gray	
VR-14-01-002	5.8	7.8	0.365	0.0383	189.0732	0.0045	0.0043	0.0516	0.0044	9.3936	59.8731		Light Gray	Pink
VR-14-01-003	7.8	12.0	0.229	0.0277	150.3730	0.0041	0.0040	0.0454	0.0044	9.7048	38.7448		Light Gray	
VR-14-01-004	12.0	16.7	0.476	0.0515	225.6286	0.0040	0.0056	0.0958	0.0059	35.3898	44.7340		Light Gray	
VR-14-01-005	16.7	17.8	0.552	0.1259	289.5014	0.0043	0.0076	0.1082	0.0065	3.3716	36.9569		Dark Red	Pink
VR-14-01-006	17.8	20.0	0.356	0.0314	209.2586	0.0040	0.0049	0.0705	0.0046	5.4171	40.7893		Light Gray	Pink
VR-14-01-007	20.0	22.9	0.376	0.0330	232.0735	0.0037	0.0049	0.0687	0.0045	15.6090	44.5780		Light Gray	
VR-14-01-008	22.9	25.0	0.400	0.1015	243.0862	0.0047	0.0065	0.0754	0.0049	22.8590	37.8581		Pink	Dark Red
VR-14-01-009	25.0	27.6	0.408	0.0391	221.8290	0.0040	0.0052	0.0768	0.0046	4.5143	45.4881		Light Gray	Pink
VR-14-01-010	27.6	31.0	0.430	0.0299	235.4091	0.0038	0.0060	0.0831	0.0045	18.5032	61.7577	14.3792	Light Gray	
VR-14-01-011	31.0	35.0	0.426	0.0329	248.8915	0.0035	0.0060	0.0801	0.0045	16.4231	63.7507		Light Gray	
VR-14-01-012	35.0	38.0	0.475	0.0384	235.9738	0.0039	0.0054	0.0805	0.0047	10.8399	61.1736		Light Gray	
VR-14-01-013	38.0	40.4	0.439	0.0911	237.0150	0.0045	0.0069	0.0700	0.0047	67.3421	64.8762		Pink	Dark Red
VR-14-01-014	40.4	42.2	0.438	0.0423	213.0012	0.0040	0.0050	0.0684	0.0042	3.9441	43.8129		Pink	Dark Red
VR-14-01-015	42.2	44.4	0.425	0.2252	239.0049	0.0048	0.0073	0.0667	0.0047	5.3051	31.2273		DR-V	Pink
VR-14-01-016	44.4	47.4	0.462	0.4340	242.1321	0.0078	0.0056	0.0768	0.0050	107.4957	32.2403		Dark Red	
VR-14-01-017	47.4	51.0	0.436	0.2065	237.2232	0.0040	0.0052	0.0751	0.0049	4.8085	30.1175		Dark Red	Varying
VR-14-01-018	51.0	53.2	0.380	0.3044	223.2181	0.0038	0.0050	0.0586	0.0041	8.7176	25.2037		DR-V	
VR-14-01-019	53.2	56.0	0.575	0.3031	309.8285	0.0041	0.0068	0.0940	0.0067	7.5776	29.2981		Dark Red	Varying
VR-14-01-020	56.0	59.1	0.657	0.5317	313.8497	0.0043	0.0063	0.1060	0.0134	41.5385	27.4434		Dark Red	Varying
VR-14-01-021	59.1	62.3	0.686	0.4057	381.6579	0.0045	0.0063	0.0979	0.0150	41.6920	45.5386		Dark Red	Light Gray
VR-14-01-022	62.3	64.4	0.778	0.2282	481.0837	0.0046	0.0088	0.0999	0.0066	6.1339	75.1191		LG-P	Dark Red
VR-14-01-023	64.4	67.5	0.578	0.2565	465.3160	0.0045	0.0065	0.0786	0.0058	6.5552	62.4118	27.3171	Dark Red	
VR-14-01-024	67.5	69.2	1.264	0.2308	701.2929	0.0055	0.0092	0.1244	0.0074	5.7663	98.5683		Pink	Varying

Appendix F Photo of core





## Appendix G Structural measurements

List of all field samples:

Structural measurements								
Nr.	Loc nr. (ArcGis)	Azimuth	Dip	X	Y	Z	Color/Formation	Comment
2	JP_2	171	27	561219.3	7822981.0	492	Pi/Rd QTZ	
4	JP_4	151	28	561212.5	7823020.8	494	Pi/Rd QTZ	
5	JP_5	154	14	561135.9	7823258.2	500	Pi/Rd QTZ	
6	JP_6	158	20	561084.0	7823357.6	501	Pi/Rd QTZ	
7	JP_7	162	30	560430.1	7822289.7	420	LG QTZ	
8	JP_8	148	23	560412.7	7822328.2	433	Pi/Rd QTZ	
9	JP_9	148	22	560370.4	7822400.1	450	Pi/Rd QTZ	
10	JP_10	151	23	560356.6	7822415.5	453	Pi/Rd QTZ	
11	JP_11	151	23	560536.2	7822506.2	464	Pi/Rd QTZ	
13	JP_13	155	23	560513.2	7822540.1	469	Pi/Rd QTZ	
14	JP_14	165	21	560637.0	7822719.7	482	Pi/Rd QTZ	
15	JP_15	153	38	560444.0	7822114.1	355	LG QTZ	
16	JP_16	125	32	560437.7	7822150.6	371	LG QTZ	
18	JP_18	175	14	560388.5	7823099.6	503	Pi/Rd QTZ	
19	JP_19	281	7	560363.1	7823219.2	501	Pi/Rd QTZ	
20	JP_20	311	20	560311.3	7823304.7	486	Pi/Rd QTZ	
21	JP_21	311	25	560240.6	7823403.1	450	Pi/Rd QTZ	
22	JP_22	321	31	560142.2	7823465.8	433	Pi/Rd QTZ	
23	JP_23	315	26	559925.4	7823663.8	406	Pi/Rd QTZ	
24	JP_24	311	20	560140.7	7823339.9	453	Pi/Rd QTZ	
25	JP_25	315	20	560110.4	7823307.6	457	Pi/Rd QTZ	
26	JP_26	325	17	560065.2	7823208.8	468	Pi/Rd QTZ	
28	JP_28	111	46	560311.6	7821719.3	295	Vagge	
29	JP_29	157	38	560341.1	7821731.0	297	Vagge	
30	JP_30	140	30	560439.8	7821826.5	315	Vagge	
31	JP_31	143	40	560607.5	7821908.0	321	Hangle - Vagge	

32	JP_32	140	27	560724.4	7822170.7	402	Hangle - Vagge	
33	JP_33	155	18	559879.9	7822396.1	431	Pi/Rd QTZ	
34	JP_34	178	15	559639.5	7822589.9	437	Pi/Rd QTZ	
35	JP_35	179	15	559584.0	7822548.7	434	Pi/Rd QTZ	
36	JP_36	177	7	559518.9	7822711.4	441	Pi/Rd QTZ	
37	JP_37	319	4	559548.2	7822774.9	446	Pi/Rd QTZ	
38	JP_38	302	13	559647.5	7823047.1	451	Pi/Rd QTZ	
39	JP_39	291	28	559660.2	7823115.4	447	Pi/Rd QTZ	
40	JP_40	303	25	559797.9	7823645.1	400	Pi/Rd QTZ	
41	JP_41	307	23	560255.1	7824235.9	434	Pi/Rd QTZ	
42	JP_42	325	16	560233.9	7824377.7	323	Pi/Rd QTZ	
43	JP_43	317	26	559931.2	7824426.4	233	Pi/Rd QTZ	
44	JP_44	303	24	559688.9	7824775.4	154	Hangle - Vagge	Contact
46	JP_46	178	17	560230.0	7822431.7	451	Pi/Rd QTZ	PR2 - 12.5m
47	JP_47	166	18	560268.0	7822425.7	452	Pi/Rd QTZ	PR2 -7.5m
48	JP_48	165	18	560332.8	7822425.7	454	Pi/Rd QTZ	PR2 -2.5m
49	JP_49	153	40	558992.7	7820616.8	343	Hangle - Vagge	Contact
50	JP_50	150	34	558973.4	7820880.3	380	LG QTZ	Contact
51	JP_51	155	33	558924.6	7820912.0	397	Pi/Rd QTZ - LG QTZ	Contact
52	JP_52	150	22	558837.5	7820940.9	398	Pi/Rd QTZ	
53	JP_53	148	18	558844.4	7821006.0	385	Pi/Rd QTZ	
54	JP_54	166	20	560343.7	7822410.0	352	Pi/Rd QTZ	PR2 -0m
55	JP_55	140	22	560376.4	7822401.4	351	LG QTZ	PR2 +5m
56	JP_56	152	24	560405.1	7822378.0	346	LG QTZ	PR2 +10m
57	JP_57	142	21	560418.1	7822362.9	342	LG QTZ	PR2 + 12.5m
58	JP_58	146	26	560468.6	7822369.5	340	LG QTZ	PR2 +17.5m
59	JP_59	140	21	560493.8	7822383.7	341	LG QTZ	PR2 +19m
60	JP_60	168	18	560305.8	7822431.7	454	Pi/Rd QTZ	PR2 -5m
61	JP_61	175	20	560243.2	7822428.3	451	Pi/Rd QTZ	PR2 -10m

62	JP_62	155	17	560217.2	7822434.0	450	Pi/Rd QTZ	PR2 -15m
63	JP_63	169	22	560204.2	7822473.7	454	Pi/Rd QTZ	PR2 -22m
64	JP_64	174	14	560198.2	7822512.0	458	Pi/Rd QTZ	PR2 -25m
65	JP_65	177	17	560182.2	7822521.3	458	Pi/Rd QTZ	PR3 - 27.5m
66	JP_66	180	16	560169.3	7822536.6	458	Pi/Rd QTZ	PR2 -30m
67	JP_67	168	16	560356.5	7822403.2	451	LG QTZ	PR2 +2.5m
68	JP_68	166	23	560282.0	7822296.1	433	LG QTZ	
113	JP_113	150	28	561289.6	7822948.0	487	LG QTZ	PR 1 0m
114	JP_114	174	28	561283.9	7822951.0	488	LG QTZ	PR 1 - 2.5m
115	JP_115	144	26	561269.1	7822954.2	489	LG QTZ	PR 1 - 5m
116	JP_116	166	27	561257.9	7822957.9	490	LG QTZ	PR 1 - 7.5m
118	JP_118	148	28	561282.0	7822982.1	491	LG QTZ	PR 1 - 12.5m
119	JP_119	138	24	561276.1	7822993.0	492	Pi/Rd QTZ	PR 1 - 17.5m
120	JP_120	144	32	561272.1	7822997.0	492	Pi/Rd QTZ	PR 1 - 20m
121	JP_121	140	21	560217.0	7822441.9	451	Pi/Rd QTZ	PR2 - 19.5m
122	JP_122	157	21	560393.2	7822398.0	450	LG QTZ	PR2 +7.5m
123	JP_123	148	20	560434.9	7822367.3	442	LG QTZ	PR2 +15m
124	JP_124	154	18	561220.5	7823073.0	497	Pi/Rd QTZ	PR1 -45m
125	JP_125	176	21	561214.9	7823026.4	495	Pi/Rd QTZ	PR1 -35m
126	JP_126	179	26	561227.8	7823019.4	494	Pi/Rd QTZ	PR1 - 32.5m
127	JP_127	166	24	561236.4	7823016.8	494	Pi/Rd QTZ	PR1 -30m
128	JP_128	164	19	561253.9	7823015.8	494	Pi/Rd QTZ	PR1 - 27.5m
129	JP_129	156	28	561262.2	7823013.1	493	Pi/Rd QTZ	PR1 -25m
130	JP_130	150	32	561275.3	7823010.7	493	Pi/Rd QTZ	PR1 - 22.5m

133	JP_133	153	24	561351.0	7823065.9	494	Pi/Rd QTZ	
134	JP_134	142	27	561427.0	7823111.5	494	Pi/Rd QTZ	
135	JP_135	144	23	561478.0	7823194.9	496	Pi/Rd QTZ	
136	JP_136	140	24	561577.2	7823170.4	491	Pi/Rd QTZ	
137	JP_137	159	44	561544.2	7822765.1	437	Hangle - Vagge	Contact
138	JP_138	153	54	561502.0	7822740.9	430	Hangle - Vagge	Contact
139	JP_139	142	35	560901.2	7822311.5	416	Hangle - Vagge	Contact
140	JP_140	146	36	560836.7	7822248.6	410	Hangle - Vagge	Contact
141	JP_141	140	30	560572.1	7822155.0	352	Vagge	
142	JP_142	122	2	559976.2	7821955.3	363	Pi/Rd QTZ	
143	JP_143	168	6	559897.1	7821955.1	359	Pi/Rd QTZ	
144	JP_144	170	10	559814.1	7821879.9	329	Pi/Rd QTZ	
145	JP_145	160	2	559790.3	7822026.8	380	Pi/Rd QTZ	
146	JP_146	146	12	559758.2	7822069.3	390	Pi/Rd QTZ	
147	JP_147	164	15	559868.5	7822110.9	401	Pi/Rd QTZ	
148	JP_148	150	18	560002.1	7822193.9	320	Pi/Rd QTZ	
149	JP_149	150	18	560122.3	7822241.4	426	Pi/Rd QTZ	
150	JP_150	170	19	560141.9	7822582.8	461	Pi/Rd QTZ	
151	JP_151	160	18	560105.9	7822622.5	465	Pi/Rd QTZ	
152	JP_152	162	18	560071.5	7822750.6	476	Pi/Rd QTZ	
153	JP_153	178	16	560055.1	7822820.9	479	Pi/Rd QTZ	
154	JP_154	176	11	560067.3	7822877.0	481	Pi/Rd QTZ	
155	JP_155	162	11	559970.0	7822865.0	480	Pi/Rd QTZ	
156	JP_156	225	6	559966.1	7822905.9	480	Pi/Rd QTZ	
157	JP_157	226	1	559931.3	7822920.3	479	Pi/Rd QTZ	
158	JP_158	281	6	559840.3	7822939.8	471	Pi/Rd QTZ	
159	JP_159	330	10	559903.8	7823011.8	473	Pi/Rd QTZ	
160	JP_160	300	14	559963.5	7823051.5	474	Pi/Rd QTZ	
161	JP_161	294	10	560071.5	7823059.4	480	Pi/Rd QTZ	
162	JP_162	278	6	560136.1	7823078.5	486	Pi/Rd QTZ	
163	JP_163	222	6	560203.3	7823066.8	493	Pi/Rd QTZ	
164	JP_164	216	7	560245.6	7823073.2	498	Pi/Rd QTZ	

165	JP_165	321	20	559871.5	7823152.2	450	Pi/Rd QTZ	
166	JP_166	322	19	559870.9	7823213.0	438	Pi/Rd QTZ	
167	JP_167	316	18	559909.2	7823247.4	438	Pi/Rd QTZ	
168	JP_168	316	18	560140.0	7823349.3	449	Pi/Rd QTZ	
169	JP_169	344	30	560215.0	7823453.7	438	Pi/Rd QTZ	
170	JP_170	324	24	560242.1	7823416.0	447	Pi/Rd QTZ	
171	JP_171	322	29	560297.0	7823453.4	446	Pi/Rd QTZ	
172	JP_172	311	27	560308.6	7823524.8	439	Pi/Rd QTZ	
173	JP_173	298	16	560443.0	7824176.6	389	Pi/Rd QTZ	
174	JP_174	300	14	560461.3	7824273.4	372	Pi/Rd QTZ	
175	JP_175	322	18	560451.7	7824309.9	368	Pi/Rd QTZ	
176	JP_176	323	18	560423.9	7824397.2	366	Pi/Rd QTZ	
177	JP_177	321	20	560423.9	7824433.0	367	Pi/Rd QTZ	
178	JP_178	321	22	560417.9	7824484.9	368	LG QTZ	
179	JP_179	300	18	560406.0	7824500.1	366	LG QTZ	
180	JP_180	300	22	560343.7	7824766.8	404	Hangle-Vagge	Contact
181	JP_181	319	22	560476.1	7824889.9	420	Hangle-Vagge	Contact
182	JP_182	312	23	560563.5	7825021.0	424	Hangle-Vagge	Contact
183	JP_183	317	28	561070.2	7825265.2	494	Hangle-Vagge	Contact
184	JP_184	302	19	560914.5	7824641.5	427	Pi/Rd QTZ	
185	JP_185	310	18	560888.0	7824519.8	428	Pi/Rd QTZ	
186	JP_186	312	22	561150.0	7824077.9	434	Pi/Rd QTZ	
187	JP_187	324	22	561171.1	7824001.2	445	Pi/Rd QTZ	
188	JP_188	328	19	561142.2	7823854.0	462	Pi/Rd QTZ	
189	JP_189	186	8	561116.0	7823516.7	499	Pi/Rd QTZ	
190	JP_190	162	10	561081.9	7823357.9	501	Pi/Rd QTZ	
191	JP_191	172	12	561005.9	7823312.2	502	Pi/Rd QTZ	
192	JP_192	171	12	560916.6	7823301.9	505	Pi/Rd QTZ	
193	JP_193	180	12	560809.9	7823270.0	513	Pi/Rd QTZ	
194	JP_194	170	10	560708.3	7823193.9	508	Pi/Rd QTZ	
195	JP_195	167	17	560858.2	7822837.3	494	Pi/Rd QTZ	
196	JP_196	138	24	560563.7	7822198.3	367	LG QTZ - Vagge	Contact
197	JP_197	145	30	560564.3	7822184.0	361	LG QTZ - Vagge	Contact



199	JP_199	154	31	560557.3	7822156.0	351	LG QTZ - Vagge	Contact
200	JP_200	146	32	560536.7	7822114.8	337	LG QTZ - Vagge	Contact
633	Not imported	300	30	559731.0	7824575.5	112	LG QTZ	PR3-0m
634	Not imported	316	28	559741.8	7824551.4	122	LG QTZ	PR3-2.5m
635	Not imported	308	30	559790.7	7824519.9	148	Pi/Rd QTZ	PR3-5m
636	Not imported	310	32	559811.5	7824495.3	164	Pi/Rd QTZ	PR3-7.5m
637	Not imported	310	32	559862.8	7824466.4	183	Pi/Rd QTZ	PR3-10m
639	Not imported	314	28	559896.5	7824454.6	211	Pi/Rd QTZ	PR3 - 12.5m
640	Not imported	320	31	559909.1	7824445.5	213	Pi/Rd QTZ	PR3 -15m
641	Not imported	314	33	559932.2	7824423.9	227	Pi/Rd QTZ	PR3 - 17.5m
642	Not imported	298	22	560256.1	7824359.6	322	Pi/Rd QTZ	PR3 . 30m
664	Not imported	310	22	560287.2	7824347.4	332	Pi/Rd QTZ	PR3- 32.5m
665	Not imported	290	21	560279.4	7824331.1	324	Pi/Rd QTZ	PR3- 37.5m
666	Not imported	291	20	560285.6	7824332.4	324	Pi/Rd QTZ	PR3-40m
667	Not imported	301	19	560293.4	7824322.9	322	Pi/Rd QTZ	PR3- 42.5m
668	Not imported	300	20	560305.1	7824323.3	323	Pi/Rd QTZ	Pr3-44m
643	JP_213	137	50	559942.5	7820952.2	179	Hangle - Unknown	Contact
644	JP_211	154	52	560031.4	7821030.1	231	Hangle - Unknown	Contact
645	JP_210	146	49	560228.8	7821239.3	262	Hangle - Unknown	Contact
646	JP_206	146	50	560320.9	7821311.6	268	Hangle - Unknown	Contact
647	JP_207	152	50	560522.7	7821469.3	283	Hangle - Unknown	Contact
648	JP_208	141	52	560744.2	7821673.7	295	Hangle - Unknown	Contact
649	JP_209	143	51	560941.6	7821917.5	316	Hangle - Unknown	Contact

638	Not imported	324	33	559690.9	7824599.6	115	Vagge	
-----	--------------	-----	----	----------	-----------	-----	-------	--

## Appendix H Leapfrog data

Structural data used when modelling outcropping boundaries:

Structural data				
Unknown - Hanglecearru				
x	y	z	dip	azimuth
559942.45	7820952.22	179	50	137
560031.42	7821030.1	231	52	154
560228.81	7821239.29	262	49	146
560320.93	7821311.58	268	50	146
560522.66	7821469.26	283	50	152
560744.22	7821673.67	295	52	141
560941.55	7821917.51	316	51	143
Hanglecearru - Vagge				
x	y	z	dip	azimuth
560607.5029	7821907.969	321	40	143
560724.4489	7822170.701	402	27	140
561544.2487	7822765.099	437	44	159
561501.9858	7822740.947	430	54	153
560901.2217	7822311.528	416	35	142
560836.6632	7822248.557	410	36	146

560490.6065	7824784.767	433	22	319
559682.4184	7824774.714	152	24	303
Vagge - Unit A				
x	y	z	dip	azimuth
560549.4691	7822154.162	351	31	148
560390.7634	7824533.076	370	22	321
559716.3214	7824591.054	140	28	316
Unit A - Unit B				
x	y	z	dip	azimuth
560358.4139	7822408.301	453	20	167
560507.4729	7822530.899	469	23	153
561276.4281	7822972.781	491	28	150
560422.2518	7824457.258	369	22	321
Unit B - Unit C				
x	y	z	dip	azimuth
560189.6339	7822426.528	447	18	168
560733.2565	7822806.186	499	19	166
561237.2064	7823019.793	501	23	170
561524.539	7823173.057	501	23	142
560471.6369	7824402.348	374	18	323

